Australian National University

Optical Metasurfaces with Advanced Phase Control Functionalities

RIFAT AHMMED AONI

Department of Electronic Materials Engineering,

Research School of Physics

A thesis submitted for the Degree of

Doctor of Philosophy of

The Australian National University

November 2021

Declaration

This thesis is an account of research undertaken in the Department of Electronic Materials Engineering (EME) and Nonlinear Physics Centre (NLPC) within the Research School of Physics at the Australian National University between May 2017 and October 2021 while I was enrolled for the Doctor of Philosophy degree.

The research has been conducted under the supervision of Prof. Dragomir N. Neshev, Prof. Andrey E. Miroshnichenko, Prof. Mohsen Rahmani, and Dr. Lei Xu. However, unless specifically stated otherwise, the material presented within this thesis is my own original work.

None of the work presented here has ever been submitted for any degree at this or any other institution of learning.

Rifat Ahmmed Aoni

November 2021

List of Publications

Book Chapter:

1. **Rifat A. Aoni,** M. R. Hasan, R. Ahmed, and A. E. Miroshnichenko, "Microstructured Optical Fiber-Based Plasmonic Sensors", *Computational Photonic Sensors*, Springer, pp. 203-232, 2019.

Peer-Reviewed Journal Articles:

Papers with results included in this thesis:

1. **Rifat A. Aoni,** Mohsen Rahmani, Lei Xu, Khosro Zangeneh Kamali, Andrei Komar, Jingshi Yan, Dragomir Neshev, and Andrey E. Miroshnichenko, "High-Efficiency Visible Light Manipulation Using Dielectric Metasurfaces", *Scientific Reports*, vol. 9, no. 1, 6510, 2019.
2. Liu, Mingkai, Quanlong Yang, **Rifat A. Aoni,** Vidur Raj, Andrei Komar, Jiaguang Han, Mohsen Rahmani et al., "Deeply Subwavelength Metasurface Resonators for Terahertz Wavefront Manipulation", *Advanced Optical Materials*, 1900736, 2019.
3. **Rifat A. Aoni,** Shridhar Manjunath, Buddini Karawdeniya, Khosro Z. Kamali, Lei Xu, Adam M. Damry, Colin J. Jackson, Antonio Tricoli, Andrey E. Miroshnichenko, Mohsen Rahmani, and Dragomir N. Neshev, "Resonant Dielectric Metagratings for Response Intensified Optical Sensing", *Advanced Functional Materials*, p. 2103143, 2021.
4. **Rifat A. Aoni,** M. Rahmani, L. Xu, and A. E. Miroshnichenko, "Hybrid Metasurface Based Tunable Near-Perfect Absorber and Plasmonic Sensor", *Materials*, vol. 11, issue: 7, 2018.
5. Komar, A, **Rifat A. Aoni,** Xu, L., Rahmani, M., Miroshnichenko, A. E., & Neshev, D. N. "Edge Detection with Mie-resonant Dielectric Metasurfaces", *ACS Photonics*, 8(3), 864-871, 2021.

Papers with results not included in this thesis:

6. Manjunath, S., Liu, M., Raj, V., **Rifat A. Aoni,** Powell, D. A., Shadrivov, I. V., & Rahmani, M., "Dual‐Region Resonant Meander Metamaterial, *Advanced Optical Materials*, 1901658, 2020.
7. **Rifat A. Aoni,** Firoz Haider, Rajib Ahmed, G. A. Mahdiraji, F. R. M. Adikan, Andrey E. Miroshnichenko, "Highly Sensitive Selectively Coated Photonic Crystal Fiber Based Plasmonic Sensor", *Optics Letters*, vol. 43, no: 4, 2018.

8. Morshed, Monir, Ziyuan Li, Benjamin C. Olbricht, Lan Fu, Ahasanul Haque, Li Li, **Rifat A. Aoni,** Mohsen Rahmani, Andrey E. Miroshnichenko, and Haroldo T. Hattori, "High Fluence Chromium and Tungsten Bowtie Nano-Antennas", *Scientific Reports*, 9, no. 1, 1-11, 2019.
9. Haider, F., **Rifat A. Aoni,** Ahmed, R., & Miroshnichenko, A. E., "Highly Amplitude-Sensitive Photonic Crystal Fiber-Based Plasmonic Sensor", *JOSA B*, 35(11), 2816-2821, 2018. **(Equal 1st author)**
10. Haider, F., **Rifat A. Aoni,** Ahmed, R., Islam, M. S., & Miroshnichenko, A. E., "Propagation Controlled Photonic Crystal Fiber-Based Plasmonic Sensor via Scaled-Down Approach", *IEEE Sensors Journal*, 19(3), 962-969, 2018.

Conference Abstracts/ Proceedings/ Posters:

1. **Rifat A. Aoni,** S. Manjunath, Mohsen Rahmani, Lei Xu, Andrey Miroshnichenko, Dragomir Neshev, "Diffractive Metagrating Sensor: An Improved Technique for Response Intensification", CLEO, USA, 2021. (Contributed Talk)
2. **Rifat A. Aoni,** Manjunath, S., Karawdeniya, B. I., Kamali, K. Z., Xu, L., Damry, A., Tricoli, A., Miroshnichenko, A., Rahmani, M. and Neshev, D., "Highly Sensitive Resonant Dielectric Metagrating Sensors", Flat Optics: Components to Systems, pp. FM3C-5, USA, 2021. (Contributed Talk)
3. **Rifat A. Aoni,** S. Manjunath, Yu Yu, Mohsen Rahmani, Lei Xu, Andrey Miroshnichenko, Dragomir Neshev, "Dielectric Huygens Metagrating-Based Refractive Index Sensor", CLEO PR, Australia, 2020. (Contributed Talk)
4. Komar, A., **Rifat A. Aoni,** Xu, L., Rahmani, M., Miroshnichenko, A. E., & Neshev, D. N. (2019, December). "Dielectric Metasurface Based Advanced Image Processing", SPIE Micro + Nano Materials, Devices, and Applications 2019 (Vol. 11201, p. 112010I). (Contributed Talk)
5. **Rifat A. Aoni,** Mohsen Rahmani, Lei Xu, Rajib Ahmed, Dragomir Neshev, and Andrey E. Miroshnichenko, "Plasmonic Metasensor for Wide Range of Refractive Index Sensing", São Paulo School of Advanced Science on Modern Topics in Biophotonics, São Carlos/ SP, Brazil, March 2019. (Contributed Poster)
6. Komar, Andrei, Lei Xu, **Rifat A. Aoni,** Mohsen Rahmani, Andrey E. Miroshnichenko, and Dragomir N. Neshev, "Experimental Demonstration of Edge Detection by Dielectric Metasurfaces", CLEO/ Europe, p. eh_4_6. Optical Society of America, 2019. (Talk)
7. **Rifat A. Aoni,** Mohsen Rahmani, Lei Xu, Khosro Z. Kamali, Andrei Komar, Jingshi Yan, Dragomir N. Neshev, and Andrey E. Miroshnichenko, "High-Efficiency Beam Deflection of Visible Light Based on Dielectric Metasurfaces", Frontiers in Optics (FiO), USA, 2018. (Contributed Poster)

8. **Rifat A. Aoni,** Mohsen Rahmani, Lei Xu, Rajib Ahmed, Dragomir N. Neshev, and Andrey Miroshnichenko, "Highly Sensitive Plasmonic Metasensor with Wide Detection Range", Frontiers in Optics (FiO), USA, 2018. (Contributed Poster)
9. Haque, A., Morshed, M., **Rifat A. Aoni,** Li, Z., Li, L., Miroshnichenko, A., & Hattori, H. T., "Electrically Tunable MnO_2 Based Metasurface", IEEE Photonics Conference (IPC) (pp. 1-2), USA, 2018. (Talk)
10. **Rifat A. Aoni,** Mohsen Rahmani, Lei Xu, Khosro Z. Kamali, Andrei Komar, Jingshi Yan, Dragomir N. Neshev, and Andrey E. Miroshnichenko, "Efficient Beam Deflection Based on Off-Resonance Dielectric Metasurface", AOS/ ACOFT Conference, Australia, 2018. (Talk)

Acknowledgements

I would like to express my deepest gratitude to my supervisors Prof. Dragomir Neshev, Prof. Andrey Miroshnichenko, Prof. Mohsen Rahmani, and Dr. Lei Xu, for giving me the opportunity to carry out my PhD research works under their supervision. I am sincerely grateful to Andrey, who gave me the opportunity to join him at the Research School of Physics, Australian National University, ACT. Andrey is a very kind, and great supervisor with a supportive manner. I have gathered metasurface simulation skills from him. I used to go to him even for very basic simulation problems, and he always guided me patiently to solve those issues. I would like to thank Mohsen for giving me hands on nanofabrication training. He is very friendly, and always motivated me to work hard. I would like to thank Lei, for his valuable support in terms of simulations. I have gathered RCWA simulation skills from him. Finally, I would sincerely like to thank Dragomir, for his expert guidance towards the accomplishment of the projects. Dragomir always helps to generate and shape the project ideas. He is a great experimentalist. I always took his guidance to establish the experimental setups, to carry out my research projects.

I would like to thank all my Electronic and Materials Engineering (EME) and Nonlinear Physics Centre (NLPC) colleagues (Khosro, Jingshi, Shridhar, Rocio, Vidur, MingKai, Quanlong, Andrei, Matthew), who make my PhD journey enjoyable. Thanks to Kathy, who makes life lot easier in terms of official matters. I would also like to thank all my collaborators for their helps and giving me opportunity to work with them to accomplish the projects. I would also like to thank Prof. Isabelle Staude, University of Jena for allowing me to visit her lab during my PhD study.

I would like to thank the ANFF team for their countless efforts to keep the machine active as well as providing various trainings. I would also like to thank Khosro and Prof. Duk (Laser Physics Centre) for their valuable suggestions to fabricate the samples.

At the end, I would like to thank my parents. Without their continuous support, I won't be able to come to this stage where I am today. I am also grateful to my elder brother Dr. Rajib Ahmed, who always inspired me to work hard, and giving me proper guidance. I would also like to thank my loving wife for her continuous support.

Finally, I would like to dedicate my PhD thesis to my father, Md. Abul Kashem Bhuiyan, who passed away during the middle of my PhD journey.

Abstract

The development of a metasurface platform with advanced micro- and nano-fabrication techniques has attracted a lot of attention. It exhibits a broad range of applications in the lens, hologram, image processing, vortex beam generation, information encoding, sensing, etc. Metasurfaces are ultrathin planar nanostructures made of subwavelength metallic or dielectric elements that can efficiently control the light characteristics such as polarisation, dispersion, amplitude, and phase. The high-index dielectric metasurfaces exhibit low loss and produce various types of resonant effects such as Mie-type resonances, Huygens' resonances, and so on. The Huygens' resonant regime of the dielectric metasurfaces exhibits the near-unity transmission window with a 2π-phase coverage. The efficient 2π-phase control capability with high transmittance feature makes the metasurfaces versatile tools for wavefront manipulation. The challenge is to realize the practical application of the metadevices such as beam deflection, optical image processing, sensing, hologram, lens, and so on. The performance of such metadevices can be made highly efficient by incorporating carefully engineered phase discretisation. Due to such engineered subwavelength wave discretisation, new functionalities that are not possible to date can be achieved by governing the phase response.

In this thesis, I will first demonstrate the efficient control of deflection angle with high diffraction efficiency in the visible wavelength. I will also discuss deeply subwavelength metasurface resonators for terahertz wavefront manipulation. Then, I will focus on a novel dielectric resonant metagrating-based highly sensitive optical biosensing technique. Finally, I will demonstrate Mie-resonant dielectric metasurfaces can be used as a passive filter to perform image processing in the form of edge detection of a target object.

Contents

Chapter 1

Introduction

1.1 Metasurfaces, a Historical Prospective

Optical metasurfaces are two-dimensional periodic ultra-thin subwavelength planar structures of metallic or dielectric elements [1-4]. The subwavelength meta-atoms rely on optical scattering instead of light propagation to modify the light characteristics such as polarisation, amplitude, phase, dispersion, etc. [3, 5]. The structures of the meta-atoms are in a subwavelength scale. As a result, the size of the meta-devices is significantly miniaturised compared to the conventional optical devices. By engineering the meta-atom design (i.e., shape, size, orientation), the features of the light interacting with the metasurfaces can be significantly manipulated [4-6]. Therefore, various conventional optical devices such as gratings, polarisers, holograms, lens, mirrors, etc. can be implemented with ultrathin flat metasurfaces [7-11]. Furthermore, metasurface can also provide unique properties that can be replaced the bulk conventional optical system, as an example edge detection filter [12, 13]. Generally, the meta-atoms are subwavelength thick and planar form factor which can be fabricated following the nano-fabrication technique. Due to its significant wavefront manipulation in ultrathin subwavelength resolution and easy fabrication technique, metasurface has attracted significant attention in last two decades for broad range of applications in different frequency regimes such as lens, hologram, wavefront control, filter, waveplates, vortex beam generation, image processing, sensing, and so on [5, 7, 8, 14, 15].

The term “metasurface” became a buzzword in the early 2000s for different applications that use diffractive optical elements. The diffraction phenomena were observed by Francis Hopkinson in 1785 [16]. Francis Hopkinson observed the dark spots at a streetlamp while looking through a stretched thin silk handkerchief in his hand. This was the filtering phenomena of a white light source at a particular wavelength band which was later demonstrated by Rittenhouse [16]. This was the basic idea of diffraction and later formed the foundation of the field of metasurfaces. The conception of optical metasurfaces has also been studied for decades in the microwave community [17]. In 1993, using different sizes element (or meta-atom) exhibits the spatially varying phase profile response [18]. In the early 2000s, Hasman’s group first demonstrated the concept

of geometric phase or Pancharatnam-Berry phase for wavefront manipulation of circularly polarised incoming light [19, 20]. Later, in early 2010, metasurface has attracted much attention in the photonics community due to its unique light controllability, planar surface, and ultrathin dimensions [21].

1.2 Recent Developments

Due to advanced nano- and micro-fabrication technologies, the fabrication of precise optical devices becomes more accessible, which leads to wider practical applications. The subwavelength thickness and altering light characteristics based on structural geometry make the metasurface a promising alternative to conventional optical devices [9]. Among the light characteristics (polarisation, amplitude, phase, dispersion, and so on), polarisation is one of the key properties. Controlling polarisation of incident light using conventional optical devices requires birefringent crystals, which are bulky and limited to broadband operation. However, metasurface can overcome these issues.

Recently, several metasurface-based waveplates (half-wave plates and quarter waveplates) have been reported covering broad operation bandwidth and specific frequency range [22, 23]. Furthermore, the polarisation state can be determined following Stokes parameters of light beams, also known as polarimetry device [24, 25]. Another important optical component that the metasurface-based platform has recently taken over is lens technology. The conventional lenses are bulky and control the optical wavefronts by accumulating phase varying the refractive index of the medium or following the surface topography, therefore, significant chromatic aberration occurs [26, 27]. These problems can be significantly overcome utilizing ultra-thin metasurfaces. Due to efficient amplitude and phase controllability, flat metalens can correct the chromatic/ monochromatic aberrations and reduce the spherical aberration [10]. In 2011, Federico Capasso proposed an idea of locally changing the phase of electromagnetic waves [21]. They utilised the V-shape ultrathin nano-resonators to control the wavefronts and realise the generalised laws of refraction and reflection. A simple achromatic broadband metalens is shown in Fig. 1.1(a), exhibiting the full-colour imaging in the visible range [28]. To date, considerable numbers of metalenses have been reported to achieve high numerical aperture, monochromatic lens, achromatic broadband lens, multi-focal lens, polarisation insensitive metalens, etc. [10, 29].

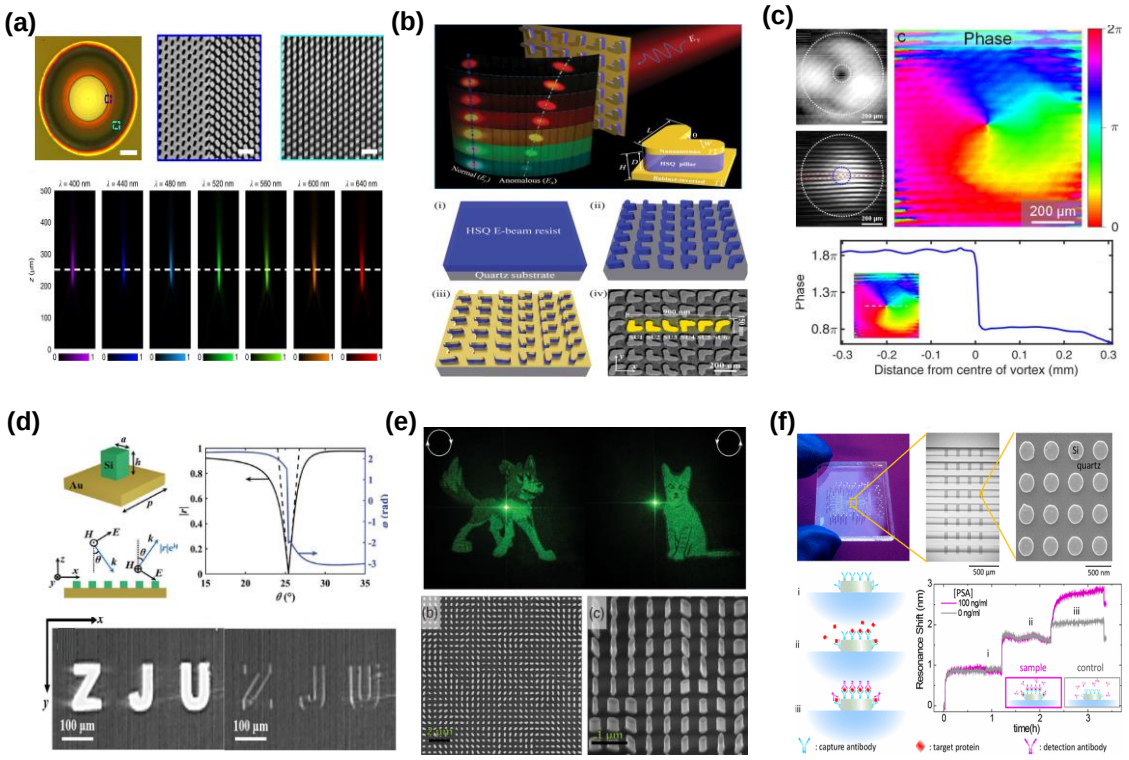

Figure 1.1 Metadevices for different functionality. (a) A broadband achromatic metalens [28]. (b) Plasmonic bilayer metasurface based visible light manipulation [30]. (c) Intensity profile of the vortex beam generation and reconstructed phase of the object beam [31]. (d) Analog optical differentiator [32]. (e) Polarisation independent chiral hologram [33], and (f) All-dielectric metasurface based optical biosensor [34].

Efficient beam deflection using metallic or dielectric metasurfaces is another essential phenomenon [30]. Due to the sub-wavelength feature, incoming light can be diffracted entirely in a certain diffraction order or split equally in different diffraction orders [35, 36]. A hybrid bilayer plasmonic metasurface-based deflector is shown in Fig. 1.1(b), exhibiting the maximum 36% conversion efficiency. Metasurface-based optical vortex beam generation is another important accomplishment that can be potentially used for optical communications, optical tweezers, high-resolution microscopy, and so on [31, 37]. All-optical dielectric metasurface-based conventional beam to optical vortex beam generation is shown in Fig. 1.1(c). More recently, utilizing the ultra-thin metasurfaces, 2nd order derivative has been realized resulting in an optical edge detection function of a given object [12, 13, 32, 38]. This metasurface approach has the potential to replace the bulky complex 4-f system and work as a perfect optical differentiator. A hybrid metasurface-based analog optical differentiator is shown in Fig. 1.1(d), which performed

the edge detection of a given image at 25 degrees oblique incident. Another very attractive application is metasurface holography. To date, numerous metasurface-based hologram works have been reported to enhance the device efficiency, altering images based on polarisation, optical data storage and so on [11, 39, 40]. Figure 1.1(e) shows an all-dielectric metasurface-based optical hologram, where the left and right circular polarised lights produce two different images. Very recently, metasurface-based sensing platforms also showed great interest and became viable alternatives to other optical sensing techniques due to device miniaturization, label-free detection, real-time detection, high throughput and massive multiplexing facilities [41, 42]. The all-dielectric metasurface-based optical biosensor integrated with a microfluidic system has been demonstrated for the first time by Ozlem *et al.* (see Fig. 1.1(f)) [34].

In summary, the metasurface platform is reaching a new paradigm by opening new application opportunities due to advanced amplitude, phase, polarisation, and dispersion control capabilities. Among those properties, the phase accumulation feature provides the extra freedom to significantly control the electromagnetic wave resulting in substantial opportunity to explore the new applications window.

1.3 Plasmonics and Dielectric Metasurfaces

In the optical frequency, all the conventional material exhibits the relative permeability close to 1. Therefore, the available conventional optical devices have only influence on the electric components of the electromagnetic field. To achieve utterly new functionality in photonics, it is necessary to impact also on the magnetic constituent of light. The goal is, therefore, to obtain a magnetic response from a material. The plasmonic metasurfaces can exhibit both electric and magnetic responses [43]. The metals have free electrons which facilitates achieving surface plasmon resonance behaviour. Utilizing the resonance behaviour, which originated from the surface plasmon resonance, can manipulate the incoming wave, and generate novel applications that are not possible with the conventional materials. To date, many interesting optical effects have been demonstrated with the plasmonic metasurfaces such as negative-index [44, 45], zero-index [45], hyperbolic media [46, 47], chiral [48], and so on. The skin depth of the material needs to be smaller to exhibit the plasmonic effects. Therefore, a significant amount of energy is lost, and the efficiency of the plasmonic metadevices is largely restricted [49, 50]. For the visible and near-infrared wavelengths, the plasmonic materials exhibit more loss.

However, plasmonic structures are more suitable in longer wavelengths such as microwave and terahertz (THz) regimes, where the losses are negligible (see Sec. 2.3).

1.3.1 Resonances in Plasmonic Nanostructures

Inside a conductor (metal), there are a lot of free electrons, and an assembly of the electrons can be considered as plasma particles. At the same time, there are equal numbers of positively charged ions from the lattice, so the total charge density in the conductor is zero. Due to the external field, electrons will move towards the positive region, and the positive ion will move opposite to the electrons, shown in Fig. 1.2. This moving mechanism creates a longitudinal oscillation in the conductor which is known as plasma oscillation or surface plasmons [51, 52]. In general, the metal and dielectric interface is used to support the surface plasmon oscillation. At a certain resonance condition, surface plasmon wave is generated at a certain resonance condition, which propagates along the surface (Fig. 1.3). This surface plasmon is only TM polarisation electromagnetic field because there is no solution for TE polarisation case of Maxwell's equation. The TM wave is decayed exponentially in the metal. This Surface Plasmon Wave (SPW) is characterised by the propagation constant as [51, 53]:

$$\beta = \frac{\omega}{c}\sqrt{\frac{\varepsilon_M \varepsilon_D}{\varepsilon_M + \varepsilon_D}} \qquad 1.1$$

Here ω is the angular frequency, c is the speed of light in vacuum, and ε_m, ε_D are the dielectric permittivity's of metal and dielectric medium, respectively.

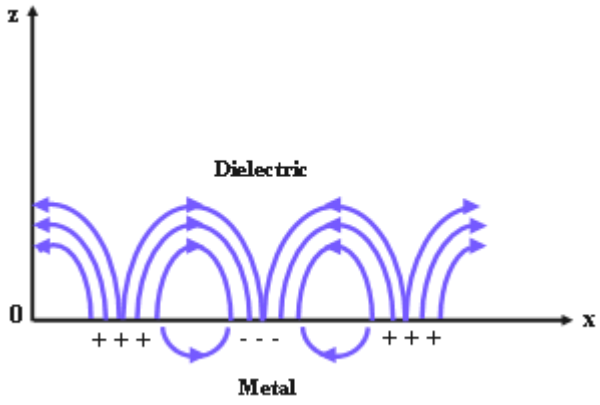

Figure 1.2 Surface plasmon oscillation in metal.

From Eq. 1.1, it is noticeable that SPW is strongly dependent on the metal and dielectric medium. Therefore, to create the surface plasmon oscillation, it is needed to excite the electrons in the conductor. So, imposing the light (EM field) is necessary on the surface. The electrical permittivity for the conductor (metal) is negative, and the electrical permittivity for the dielectric is positive. In the dielectric medium, the propagation constant (maximum) can be written as [53]:

$$\beta = \frac{\omega}{c}\sqrt{\varepsilon_S} \qquad 1.2$$

The above equations show that the propagation constant for surface plasmon waves is higher than the propagation constant of light in the dielectric medium. Therefore, surface plasmon can't be excited with the normal light; it requires the light with extra momentum with the same polarisation state as the surface plasmon wave. Also, the propagation constant should be matched with the surface plasmon wave.

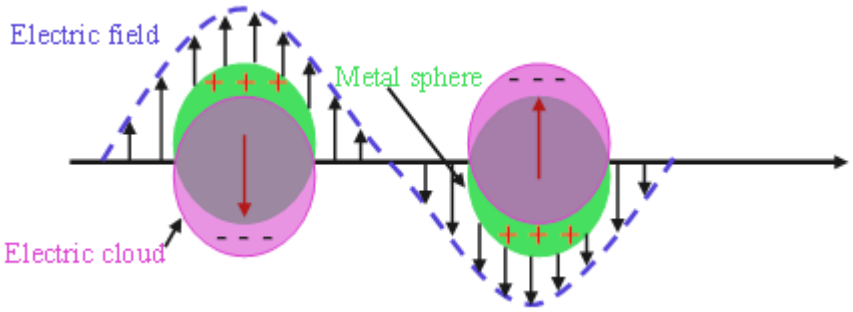

Figure 1.3 Localised surface plasmon resonance (SPR) when field (light) interacts with the plasmons.

1.3.2 Resonances in Dielectric Nanostructures

Dielectric materials are a viable alternative to plasmonic materials. Since they exhibit less loss in optical frequency resulting in significant improvement of the device performance. According to Mie theory, a spherical dielectric particle also can exhibit the magnetic dipolar resonance by following some specific criteria's such as higher dispersive medium, $n \geq 2$, and the spherical particle with radius, $r \approx \lambda / 2n$, where r is the nanoparticle radius, n is the refractive index of the particle and λ is operating wavelength. Furthermore, while satisfying the following conditions, $r \approx \lambda / n$, a second magnetic dipole response with a

much smaller transmission/ reflection amplitude could occur. According to Fig. 1.4(a), it is clearly visible that the dielectric particle with a refractive index larger than 2 can efficiently produce fundamental electric and magnetic dipolar resonances and higher-order dipolar resonances.

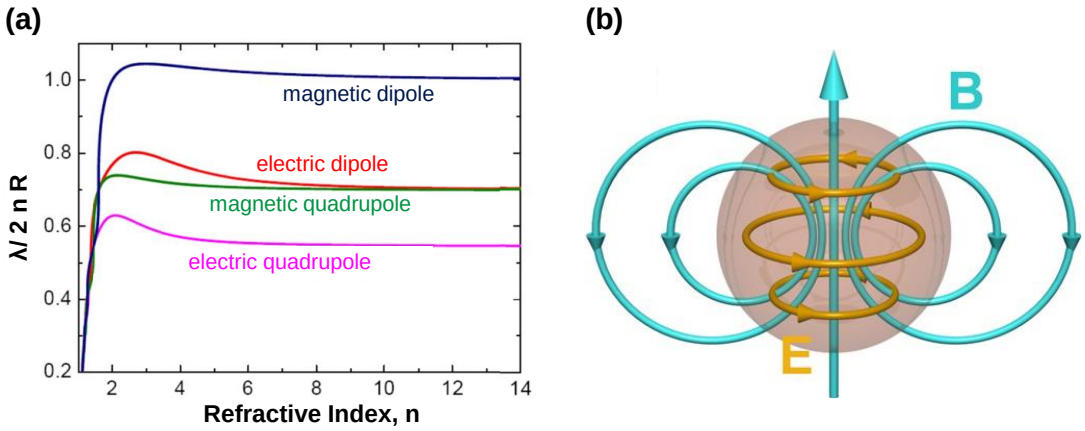

Figure 1.4 (a) The size of the dielectric particles as a function of refractive index to achieve the electric and magnetic resonance together, and (b) high-index dielectric particle that supports displacement current to generate magnetic dipole resonance [54].

This phenomenon is also experimentally verified, which confirms that the first resonance is the magnetic dipolar (MD) resonance, second resonance is electric dipolar (ED) resonance, third resonance is magnetic quadrupolar (MQ) resonance and fourth resonance is the electric quadrupolar (EQ) resonance [54]. The large size of a dielectric particle and with the high refractive index support the displacement current inside the particles. The strong circulation of displacement currents generates due to the polarisation of the incident electric field being antiparallel at opposite sphere boundaries, as shown in Fig. 1.4(b). Therefore, oscillating magnetic fields are created to lead to magnetic resonance, which is a remarkable achievement in nanophononics. This unique MD resonance feature of high-index dielectric material overcomes the efficiency issue of the plasmonic materials, and gradually replaces most optical applications.

For a homogeneous spherical particle, Gustav Mie provides a solution to the Maxwells equations for a homogeneous spherical particle for the scattered electric field, E_s and magnetic field, H_s [55]. The scattered electric and magnetic fields are the linear

combinations of the two vector fields M and N, where a_n and b_n are two scattering coefficients. The scattered E_s and H_s can be written as:

$$\begin{aligned} E_s &= \sum_{n=1}^{\infty} E_n \left(i a_n N_{e1n}^{(3)} - b_n M_{o1n}^{(3)} \right), \\ H_s &= \frac{k}{\omega \mu} \sum_{n=1}^{\infty} E_n \left(i b_n N_{o1n}^{(3)} + a_n M_{e1n}^{(3)} \right), \end{aligned} \tag{1.3}$$

Here angular frequency is ω, the background medium, and scattered permeability is μ, and wavenumber is k. M and N can be expressed as:

$$\begin{aligned} M &= \nabla \times (c\psi), \\ N &= \frac{\nabla \times M}{k}, \end{aligned} \tag{1.4}$$

Where the arbitrary constant vector is c, and ψ is a solution to a scaler wave equation.

$$\frac{1}{r^2}\frac{\partial}{\partial r}\left(r^2 \frac{\partial \psi}{\partial r} \right) + \frac{1}{r^2 \sin\theta}\frac{\partial}{\partial \theta}\left(\sin\theta \frac{\partial \psi}{\partial \theta} \right) + \frac{1}{r^2 \sin\theta}\frac{\partial^2 \psi}{\partial \phi^2} + k^2 \psi = 0, \tag{1.5}$$

The scalar function ψ can be expressed as:

$$\psi(r, \theta, \phi) = R(r)\Theta(\theta)\Phi(\phi),$$

leading to solutions of

$$\begin{aligned} \psi_{emn} &= \cos m\phi P_n^m (\cos\theta) z_n (kr), \\ \psi_{omn} &= \sin m\phi P_n^m (\cos\theta) z_n (kr), \end{aligned} \tag{1.6}$$

where e and o refer to even and odd, Legendre function is $P_n^m(cos\theta)$ for the degree of n and order m. Zn is any of four spherical Bessel functions, j_n, y_n, $h_n^{(1)}$ and $h_2^{(1)}$. $h_n^{(1)}(kr)$ is the spherical Hankel function.

The normal electromagnetic modes of a spherical particle are M_n and N_n. The scattered fields are the superposition of normal modes which are governed by the transverse electric (TE) and transverse magnetic (TM) modes with no radial electric and magnetic components, respectively, based on the values of a_n and b_n. The first four modes of each type are shown in Fig. 1.5. The lowest order mode is the dipolar mode which can be achieved while n = 1. In Fig. 1.5, it is clearly visible that n =1 leads to a dipole-like

radiation pattern for N_{e11} and the circulating electric field, which gives rise to a magnetic dipole radiation pattern for M_{o11}. Similarly, a higher *n* value represents the higher-order modes.

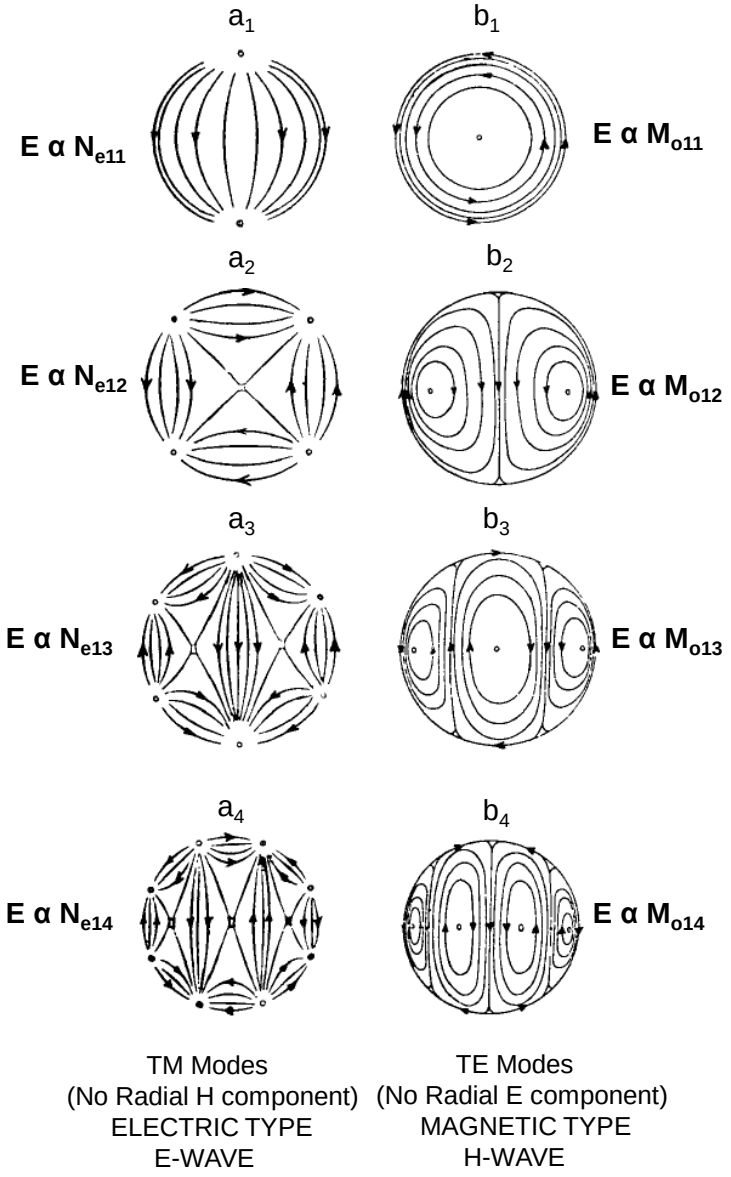

Figure 1.5 The first four TE and TM modes in Mie theory [55].

The scattering and extinction cross-section of a particle can be expressed as:

$$C_{sca} = \frac{2\pi}{k^2} \sum_{n=1}^{\infty} (2n+1)\left(|a_n|^2 + |b_n|^2\right), \tag{1.7}$$

$$C_{ext} = \frac{2\pi}{k^2} \sum_{n=1}^{\infty} (2n+1)\,\mathrm{Re}\{a_n + b_n\}, \tag{1.8}$$

where the two scattering coefficients, a_n and b_n are functions of the size parameter $x = 2\pi a/\lambda$, and a is the characteristic length or radius of the scatterer.

I have also further investigated the Cartesian components. I have performed the multipolar analysis of the scattering cross-section until the magnetic quadrupole mode. The multipoles can be retrieved from the total field $E(r)$ inside the nanoparticle according to the following equations [56]:

$$p = \varepsilon_0(\varepsilon_d - \varepsilon_r)\int E(r)dv \tag{1.9}$$

$$m = \frac{i\omega\varepsilon_0(\varepsilon_d - \varepsilon_r)}{2v_d}\int [r \times E(r)]dV \tag{1.10}$$

$$Q_{\alpha\beta} = \frac{\varepsilon_0(\varepsilon_d - \varepsilon_r)}{2}\int \{r_\alpha E_\beta + r_\beta E_\alpha - \frac{2}{3}[r.E(r)]\delta_{\alpha\beta}\}dv \tag{1.11}$$

$$M_{\alpha\beta} = \frac{i\omega\varepsilon_0(\varepsilon_d - \varepsilon_r)}{3v_d}\int \{[r \times E(r)]_\alpha r_\beta + [r \times E(r)]_\beta r_\alpha\}dv \tag{1.12}$$

where electric and magnetic dipoles are defined by p and m, respectively. Also, $Q_{\alpha\beta}$ and $M_{\alpha\beta}$ refer to the electric and magnetic quadrupole tensors, respectively. ε_r is the relative permittivity of the nanoantenna, v_d is the speed of light in the background medium, α, β represent the Cartesian coordinates.

Finally, the total scattering cross-section can be defined as:

$$\begin{aligned}\sigma_{sca} &= \sigma_{sca}^{p} + \sigma_{sca}^{m} + \sigma_{sca}^{Q} + \sigma_{sca}^{M} + \cdots \\ &= \frac{\frac{v_d{}^2 k_d{}^4 z_d}{12\pi}|p|^2}{I_0} + \frac{\frac{v_d{}^2 k_d{}^4 z_d}{12\pi}|m|^2}{I_0} + \frac{\frac{v_d{}^2 k_d{}^6 z_d}{40\pi}\Sigma|Q_{\alpha\beta}|^2}{I_0} + \frac{\frac{v_d{}^2 k_d{}^6 z_d}{160\pi}\Sigma|M_{\alpha\beta}|^2}{I_0}\end{aligned} \tag{1.13}$$

Where I_0 is the incident power density. The four decomposed terms correspond to contributions from p, m (which can be further decomposed into m_1 and m_2), Q and M, respectively.

1.4 Huygens' Metasurfaces

The first demonstration of Huygens' metasurfaces or metamaterial Huygens' metasurfaces for tailoring the wavefronts with a metallic reflectionless sheet occurred at the microwave frequencies [57]. In the later stage, the Huygens' principle was developed for mid-IR and optical frequencies [58, 59]. However, recently, this Huygens' phenomena

have been established in an all-dielectric platform at the optical frequency regime, which leads to efficient functional metadevices [60, 61].

1.4.1 Huygens' Principle

In 1690, Christiaan Huygens proposed that *"every point on a wavefront acts a secondary source of outgoing waves which expand in forward direction, and that the sum of such secondary waves would lead to a forward only propagating wave"*, [62] which is currently known as Huygens' principle. Later, Huygens' principle was widely explored in the interference phenomena. The schematic of Huygens' principle is shown in Fig. 1.6. The incoming waves propagate towards the forward direction. and when found an opening, the wavelets (yellow spherical) at the interface of the incident plane wave and opening create the wavefronts. The yellow spherical wavelets work as a secondary wave source which is also known as Huygens' source, and create the wavefronts. Finally, the constructive interference of the wavefronts (blue lines), it creates an entirely new wavefronts (orange lines) that propagate towards the forward direction.

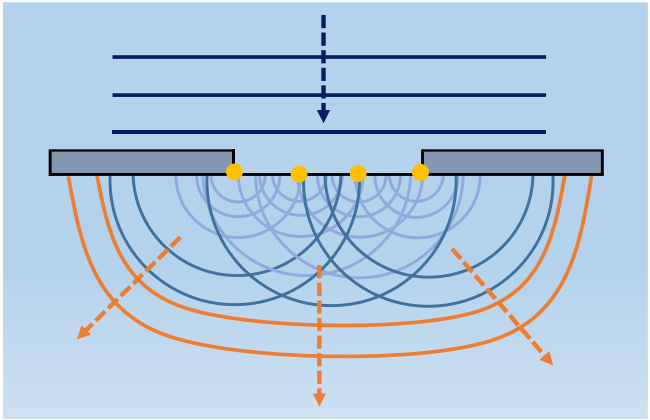

Figure 1.6 Conceptual diagram of wave diffraction phenomena following the Huygens' principle.

The ideal Huygens' source where the incoming wave propagates towards the forward direction is demonstrated by Love in 1901 [63]. The fictitious radiating source can help to generate the propagating waves in the forward direction, which possess the far-field radiation pattern of a pair of crossed electric and magnetic dipoles.

1.4.2 Kerker's Condition

In 1983, Kerker *et al.* [64] proposed that if the electric and magnetic polarizabilities are exactly same in a dielectric particle such as $\varepsilon = \mu$ then that particle can completely suppress the backscattering. This is occurred due to the destructive interference of the scattered field in the backward propagating direction of the incident field. This condition of zero back scattering is also known as Kerker's condition or first Kerker condition (zero reflectance). During the initial development of Kerker's condition, it was widely used at the microwave frequency due to the lack of magnetic element ($\mu_r \neq 1$) at the optical frequencies. Due to the development of metasurfaces that can simultaneously possess the electric and magnetic dipoles at the optical frequency, this Kerker's phenomena is widely using to suppress the backward scattering [65, 66]. The constructive interference of ED and MD dipoles can completely suppress the backward scattering, which is also known as first Kerker condition (see Fig. 1.7). Also, constructive interference of ED and EQ can suppress the backward scattering. Due to significantly suppressing the backward scattering, it allows transmitting most of the light in the forward direction, leading to high efficiency transmissive metadevices.

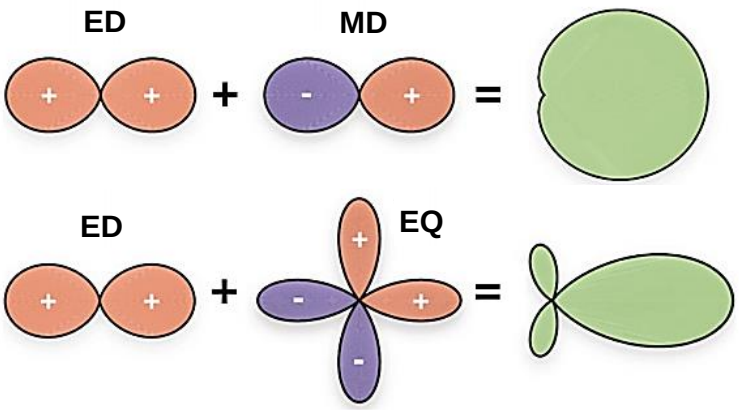

Figure 1.7 The constructive interference of multipoles to suppress the backward interference [67].

1.4.3 Tailored All-dielectric Huygens' Metasurfaces

In 2013, Staude *et al.* demonstrated the tailoring of the directional scattering using high-index all-dielectric nanoparticles [68]. The high-index dielectric particle possesses

electric and magnetic dipole resonances. By tuning the diameter of the particle, it is possible to spectrally tune the position of the electric and magnetic dipole resonances. Figure 1.8 shows the experimentally measured transmission and reflection spectra while varying the silicon disk diameters. It is clearly noticeable that at a certain disk diameter, the spectral overlap of electric and magnetic resonances leads to maximizing the transmission and minimizing the reflection. After this remarkable observation, in 2015, Decker *el al.* proposed the first all-dielectric Huygens' metasurfaces based on resonant nanoparticles [60]. It was analytically observed that the field amplitudes of electric and magnetic dipole resonances are precisely the same at a specific diameter of the dielectric particle. At that condition, it exhibits the complete near-unity transmission window (Fig. 1.9(a)). At the same time, the phase also accumulates at that condition and exhibits 0 to 2π phase response (Fig. 1.9(b)). Finally, spectral overlap of the electric and magnetic dipole resonances are observed. The numerically calculated transmission and phase response with varying the disk radius is shown in Figs. 1.9(c, d).

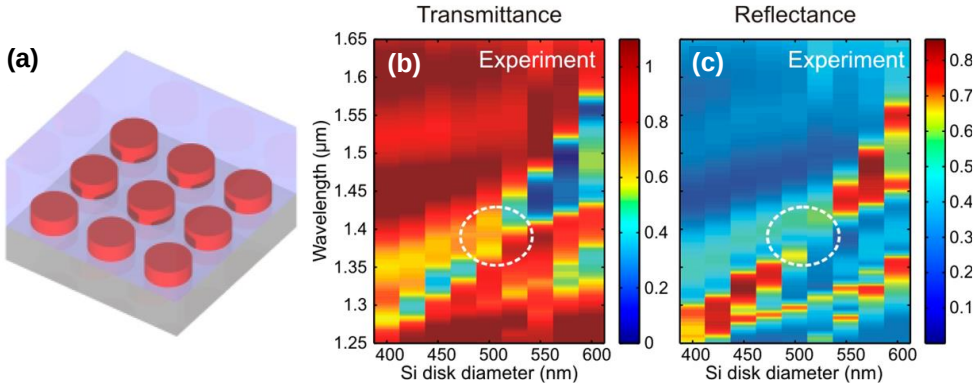

Figure 1.8 (a) Schematic of the silicon nanodisks where the height of the nanodisks was constant at 220 nm, and it was embedded into a low-index medium (n = 1.50). The lattice constant a was varied along with diameter d where, $a = d + 200$ nm. Experimentally measured optical (b) transmittance, and (c) reflectance [68].

At the nanodisk radius of 242 nm, the electric and magnetic dipole resonances have a perfect spectral overlap at 1340 nm wavelength. Therefore, a transmission (99%) window is generated and observed. As expected, it also preserved the 2π phase coverage (Fig. 1.9(d)). Due to the near-unity transmission feature with 0 to 2π phase profile, it showed great interest in the field of wavefront control and exhibits lots of potential applications such as lens, hologram, imaging, vortex beam generation, and etc. [10, 31, 40].

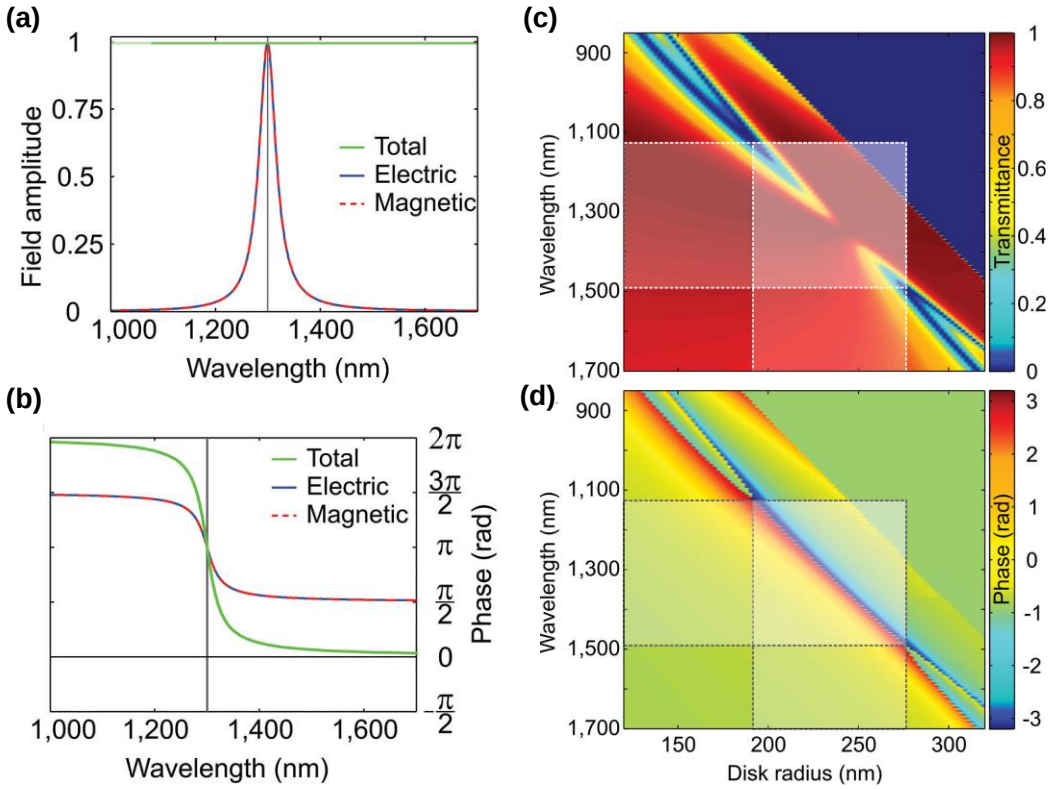

Figure 1.9 Analytical results of spectrally overlapping the electric and magnetic resonances: (a) Field amplitudes and (b) phase spectrum. Numerically calculated (c) transmission intensity and (d) phase response where the nanodisk (a-Si) height, h = 220 nm, lattice constant, $a = 1.38 \times 2 \times r_d$ with an embedding medium of n = 1.66 [60].

1.5 Metasurfaces – Phase Discretisation

The individual meta-atoms possess amplitude and phase responses. By changing the size and rotating the nanostructure's orientation, we can easily change the phase response. To efficiently control the wave propagation, it is necessary to cover the phase response from 0 to 2π. A simple example of a meta-deflector is shown in Fig. 1.10(a). By changing the radius of the circular nanodisk from 83 to 190 nm, a phase profile from 0 to 2π is achieved and the individual nanodisk exhibits the maximum transmission efficiency. Here the phase response is discretised into eight steps with π/4 increments to cover 2π phase response. Now by choosing the given eight nanodisks it is possible to design any phase dependent applications such as metalens, hologram, vortex beam generation, meta-deflector, and so on. It is worthy to note that, to cover the 2π phase response, it is not limited to eight discretised steps. By increasing or decreasing the phase discretised

elements (PDEs) to cover 2π phase response, it is possible to significantly control the deflection angle, which can be calculated following the Snell's law [69].

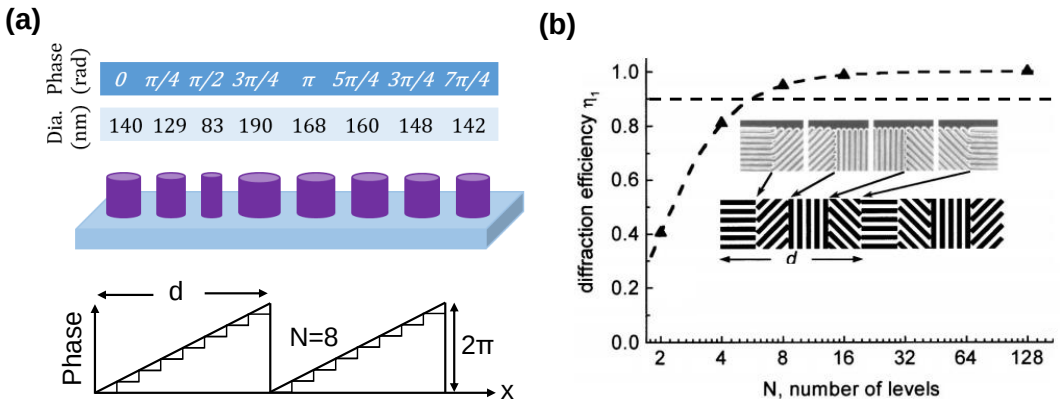

Figure 1.10 (a) Eight nanodisks based supercell where the individual nanodisks are responsible for phase shift from 0 to 2π with π/4 phase increments, and (b) 1st order diffraction efficiency as a function of discretised phase units [70].

Due to an increase of PDEs, the phase change between nearby meta-atoms will be small, therefore the coupling between the nearby meta-atoms exhibits quite uniform coupling, leading to enhancing the device performance. Hasman *et al.* investigated the discretise Pancharatnam–Berry (PB) phase optical elements and showed that the device performance could be significantly enhanced by increasing to a certain number of PDEs [70]. The efficiency of the diffractive optics can be calculated following the below equation [71, 72]:

$$\text{Diffraction efficiency of } 1^{st} \text{ diffraction order, } \eta_1 = \left[\left(\frac{N}{\pi}\right)\sin\left(\frac{\pi}{N}\right)\right]^2 \qquad (1.17)$$

where N is the number of discretised phase elements. According to the Eq. 1.17, for 2, 4, 6, 8, and 16 PDEs can provide the diffraction efficiency of 40.5%, 81.1%, 95% and 98.7%, respectively. From Fig. 1.10(b), it is clearly visible that the diffraction efficiency has a significant effect with lower than 8 PDEs. By utilizing the PDEs 8 or more than 8, achieving the 1st diffraction efficiency of more than 95% is possible. However, it is worthy to note that the device fabrication become more complex by increasing the number of PDEs.

To exhibit this type of phase discretisation to cover 0 to 2π phase response, the phase modulation can be based on a resonant effect, non-resonant effect or a combination of both effects [21, 73]. Different types of phase control mechanisms are shown in Fig. 1.11. Generally, the Mie-type resonances are considered in the localised resonance (Fig. 1.11(a)). By spectrally overlapping the electric and magnetic resonances, 2π phase response can be achieved [21, 60, 74]. On the other hand, photonic crystal and high-contrast grating structures based 2π phase accumulation techniques are considered in the extended resonance category (Fig. 1.11(b)) [75-77]. The above-mentioned both types modulate the phase employing resonant features. The effective index method is another way to control the phase where the fill factor of the nanostructures plays a vital role [15, 39]. The light passes through the different sizes of meta-atoms differently. Therefore, the effective index of the individual meta-atoms is different. The phase response of the individual meta-atoms can be obtained by [29]; $\phi = \frac{\omega}{c} n_{eff} h$, where n_{eff} is the effective index of the meta-atom, and h is the height of the disk. Finally, PB phase is the widely used technique to modulate the phase. However, this case requires the circularly polarised incident beam [33, 78]. These effective index and PB phase techniques fall under the non-resonant category.

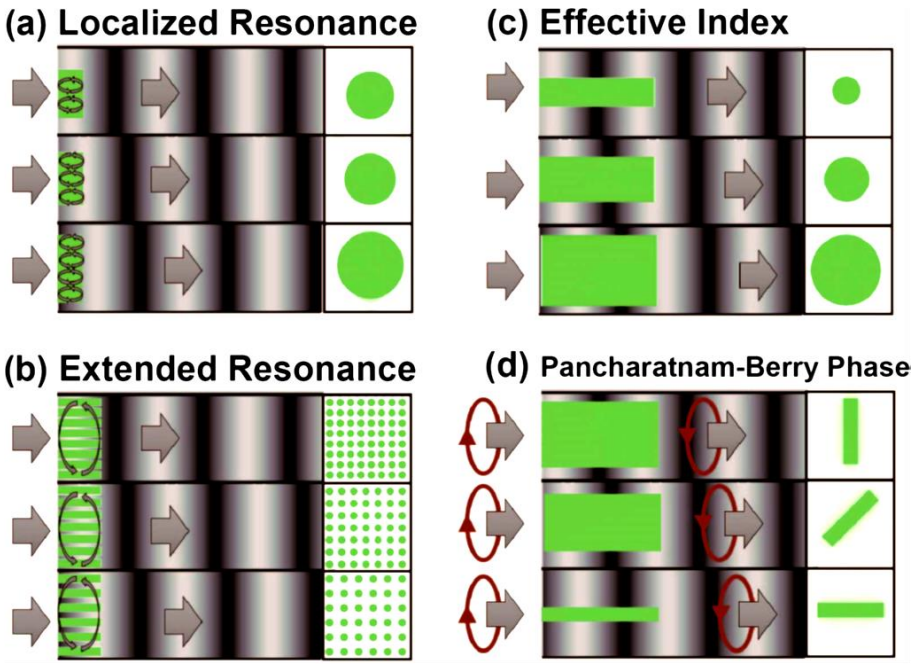

Figure 1.11 Arbitrary Phase control using resonant and non-resonant nanostructures. (a) Localised resonance, (b) Extended resonance, (c) Effective index method, and (e) Pancharatnam–Berry phase technique [73].

In these cases, the aspect ratio of the nanostructures is quite high compared to the resonant nanostructure-based techniques. Therefore, the resonant structure can be much thinner, which is easy to fabricate as well as highly reproducible. However, it is worthy to note that the resonant structures are more sensitive to fabrication tolerance.

1.6 Motivation and Thesis Outline

To date, many different plasmonic and all-dielectric metasurfaces have been proposed and demonstrated by the scientific community. By varying the geometries, working regimes, and sophisticated designs, researchers are applying metasurfaces in different applications. As briefly mentioned in section 1.5, using phase discretisation makes it is possible to control wavefronts and efficiently improve device efficiency. Due to efficient wavefront control, we can manipulate the incoming wave and develop new applications. Although basic operations have been derived using ultrathin metasurfaces, more advanced subwavelength wave discretisation is required to develop advanced functionalities. In this thesis, I will focus on developing efficient metadevices for three different applications: high-efficiency wavefront manipulation in the visible and THz regimes, highly sensitive diffractive biosensing, and image processing in the form of edge detection.

After the Introduction, there are three main chapters for three different applications. All the chapters are involved with numerical and experimental results.

Chapter 2 of this thesis is divided into two main sections. In the first main section, I will demonstrate high-efficiency beam manipulation at the visible wavelength. I will explore multipolar decomposition analysis as a function of nanodisk radius. I will present two different supercells and their effects on enhancing efficiency. Finally, I will demonstrate a novel technique to introduce the higher diffraction orders by introducing 3π phase profile. I have performed wave propagation, transmission (in different diffraction orders), and far-field analysis to investigate the supercell performance. All the supercell analysis is involved with numerical and experimental results. Later, in the second main section, I will focus on ultra-compact metadevice based on deeply subwavelength metaunits for THz wavefront manipulation. I will first present the design concept and an advanced fabrication technique. Next, I will demonstrate the numerical and experimental results to justify the efficient wavefront manipulation.

Chapter 3 will demonstrate a novel optical sensing technique. Firstly, I will establish the novel diffractive sensing concept. Later, I will demonstrate the numerical and experimental refractive index (RI) sensing results for large deflection angles. In the second part of this chapter, I will present the small deflection angle-based diffractive sensor, which exhibits a highly sensitive response compared to the existing dielectric grating-based sensors. Finally, I will demonstrate the sequence of functionalization process and experimentally measured biomarker mouse-IgG results.

Chapter 4 will demonstrate an image processing technique in the form of edge detection. All-dielectric metasurface has been used with Mie-type resonance feature to achieve high-efficiency edge detection. I will first demonstrate the concept of edge detection using ultrathin silicon metasurfaces. Later, I will discuss actual the numerical and experimental results of edge detections. Finally, I will explore the experimental results of polarisation dependency in edge detection.

Chapter 5 is the conclusion of this thesis. This chapter will summarise all the key information presented in the thesis based on the applications. Also, I will provide a brief outlook on future works.

Chapter 2

Metasurface Based Advanced Wavefront Manipulation

The material in this chapter was in part presented in [69, 79].

In this chapter, I will show efficient beam manipulation in visible and terahertz regions. In sec. 2.2, I will first demonstrate the design concept of meta-deflectors for operating at the visible wavelength. Later, I will briefly discuss the numerical and experimental results of beam deflection for different deflection angles. I will also briefly discuss the step-by-step nanostructure fabrication steps. Finally, I will demonstrate an advanced beam-deflector, which allows multiplexing the beam. Besides the efficient beam manipulation at the visible wavelength, I will also demonstrate the efficient beam manipulation at the THz frequency using extreme sub-wavelength resonators. Firstly, I will discuss the design concept of sub-wavelength metaunit. Subsequently, I will demonstrate the advanced electron beam lithography technique, which allows us to fabricate the 5×5 mm^2 patterned area within a minimal time (~2 hrs). Finally, I will demonstrate the numerical and experimental beam deflection results at the THz frequency.

2.1 Introduction

Wavefront manipulation refers to the ability to modify and shape light, which is very important in our daily life as well as in scientific research. Available conventional optical components are still bulky, costly, and difficult to manufacture with high accuracy, which limits their applications, especially in portable and wearable devices [29, 80]. Metasurfaces have shown outstanding abilities to overcome these issues through their unique light manipulation capabilities. Metasurfaces are ultrathin single-layer planar nanostructures made of subwavelength metallic or dielectric elements, which can be designed to efficiently control the light characteristics such as polarisation, dispersion, amplitude, and phase [5, 81]. In particular, the efficient 2π-phase control capability with high transmittance/ reflection feature makes the metasurfaces versatile tools for many applications including flat lenses, holograms, vortex generators, beam deflection, polarimeters, imaging, etc. [39, 82-84]. Among these applications, efficient beam steering at visible and terahertz regimes is highly desirable for a range of applications including

LiDAR (light detection and ranging), dynamic tuning, imaging, display applications, and so on [11, 39, 84, 85].

2.2 Efficient Wavefront Manipulation in Visible Wavelengths

The wavefront manipulation is key to lots of novel optical applications. To achieve efficient wavelength manipulation, it is important to have 0 to 2π phase control. The conventional blazed grating doesn't have controllability in phase and polarisations therefore, it is limited to a broad range of applications. By utilizing the discretise phase level, we can efficiently increase the device efficiency [70]. Therefore, intermediate phase levels (within 0 to 2π) play an important role to the coupling between the meta-atoms and lead to improving the device performance. The 2π-phase response of the dielectric metasurfaces can be achieved via Mie-resonance, Pancharatnam-Berry phase elements, and in-plane anisotropy of the scatterer [86-89].

In this work, we concentrate on Mie-resonance Huygens' metasurfaces that take place by overlapping electric dipole (ED) and magnetic dipole (MD) resonances in dielectric metasurfaces. Such metasurfaces can overcome the absorption loss of the materials leading to a full 2π-phase response with near-unity transmission [60, 68, 90]. Recently, Adam *et al.* reported the high-efficiency all-dielectric Huygens' metasurfaces, which show the experimental refraction efficiency of 63.6% (infrared) and 78% (optical frequency) [91]. Zhou *et al.* reported the implementation of crystalline-silicon based dielectric metasurface with the experimental beam deflection of 19.27° and transmission efficiency of 67% at 532 nm wavelength [92]. Shalaev *et al.* also reported a rectangular nanopost based beam steering approach, which has a transmission efficiency of 36% at telecommunication wavelength [93]. In another paper, an all-dielectric C-shaped gradient metasurface was employed to achieve a deflection angle of 15^{o} at the normal incident beam[94]. Furthermore, another interesting approach for electromagnetic wave manipulation was shown through elliptical disk based gradient metasurface leading to a wave deflection of 7^{o} [95]. Chalcogenide alloy PbTeLi based high-efficiency transmittance metasurfaces was also reported with the experimental transmission efficiency of 75% and a deflection angle of 15.1^{o} at mid-infrared wavelengths [96]. Utilising liquid-crystals, thermally-tuneable dielectric metasurfaces was also reported, showing the dynamic beam switching from zero to 12° with 50% transmission efficiency [97]. Recently, Sell *et al.* showed nonintuitive geometry that can significantly improve

the deflection angle and achieve the wide deflection angle of 75° with the total deflection efficiency of 75% (TM polarisation mode) at the operating wavelength 1050 nm [98]. Nevertheless, this sophisticated geometry requires precise optimisation and its fabrication is challenging. Several theoretical approaches were also reported where transmission and reflection modes were used to achieve the deflection behaviour [99-101]. However, the bottleneck of all the above-mentioned techniques shows the low transmission of the individual unit cell in the visible range. Therefore, the overall transmission and deflection efficiency of the metadeflector in the visible range was diminished significantly [92, 93]. As a result, there is a serious quest to improve the transmission and deflection efficiency of optical devices in the visible range. Silicon has been employed as a material of choice in the near and mid-infrared regions, due to its negligible loss in these regions. However, it exhibits remarkable absorption/ loss in the visible range.

In this work, we propose an engineered dielectric metadevice operating at visible wavelengths. We have designed and fabricated a silicon metasurface that exhibits not only an efficient beam deflection capability, but also a high transmission property utilising the phase control. Our metasurface consists of circular nanodisk-based supercells fabricated from amorphous silicon. By changing the diameter of the disks, we manipulate the phase delay of the electromagnetic waves. Utilising properties of near-unity transmittance and discrete phase of dielectric nanodisks, we have demonstrated that the transmitted beam angle can be varied significantly by controlling the supercell length. Furthermore, we have introduced a way to combine the waves coming from two different supercells that leads to the excitation of high diffraction orders.

2.2.1 Design Concept

We have designed three different gradient metasurfaces, consisting of fifteen (2π-phase response), eight (2π-phase response), and fifteen (3π-phase response) amorphous silicon (a-Si) nanodisks that can efficiently manipulate the propagating wave angles. The schematic of the proposed fifteen disks supercells is shown in Fig. 2.1. The disks are arranged periodically in order of phases from 0 to 2π with π/7 increments, which helps to bend the propagating wave following the phase delay phenomena. The height (h) of the disks is 352 nm, and the disks are arranged in a subwavelength periodic structure with a lattice constant (p) of 300 nm. The diameter of the disks varies between 80 and 192 nm. We have considered a-Si material, and its optical properties have been measured using an

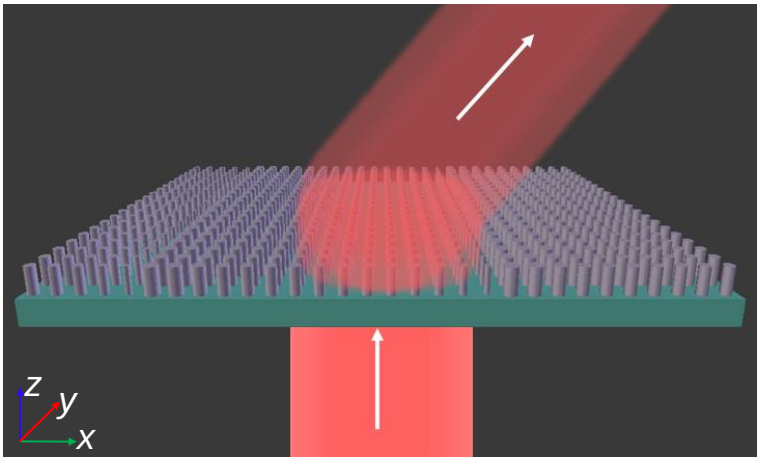

Figure 2.1 Schematic of the proposed beam deflector, with supercell containing fifteen nanodisks where each responsible for phase shift from 0 to 2π with π/7 increments [69].

ellipsometer. The obtained data are used in our numerical investigations. By controlling the different gases level, I have deposited high-purity uniform a-Si layer using plasma-enhanced chemical vapor deposition (PECVD) which provides less absorption at the visible wavelengths. I have provided the measured a-Si refractive index data in appendix A. We numerically investigated the transmission and phase response of the individual nanodisk using rigorous coupled-wave analysis (RCWA) method. RCWA is a fast response modelling method, that helps to optimise the nanodisk parameters effectively. RCWA has been widely used for investigating the transmission properties of periodic structures due to its fast convergence and accurate calculations. RCWA is a freely available open-source software package that works in the frequency domain [102, 103]. With varying disk diameters, the transmission and phase responses are shown in Fig. 2.2.

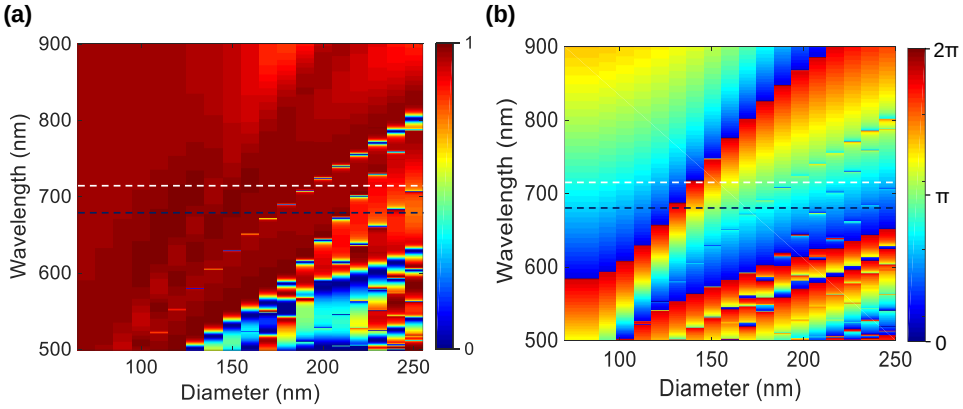

Figure 2.2 Numerically calculated (a) transmission, and (b) phase response with varying the disk diameters. The dashed lines show the operating wavelengths.

We varied the disk diameters from 50 to 250 nm and kept the other parameters constant. By varying the disk diameters, the optimised nanodisk can exhibit near-unity transmission region (Fig. 2.2(a)) and 0 to 2π phase response (Fig. 2.2(b)). It is noticeable from the 2D transmission profile that the near-unity transmission response is achieved at the off-resonant region. To study the resonance condition in detail, multipolar decomposition of the nanodisks has been done with different disk radii shown in Fig. 2.3(a). We have followed the equations 1.9 - 1.12 for the cartesian multipolar decomposition analysis. As can be seen, the strong resonance occurs around the disk diameter of 200 nm, where the MD and EQ are excited. However, when the disk diameters are in the range of 80 to 192 nm, the excitation of ED and MD is moderate and forms a slightly off-resonant region. This is indeed a significant advantage, leading to high transmission and low absorption, simultaneously. Alongside this, we have investigated the effective medium properties of a disk (130 nm diameter) shown in Fig. 2.3(b). We used the Smith retrieval technique to investigate the effective medium properties of the individual nanodisks [104].

The simulated S-parameters results were renormalised in terms of free space impedance, Z_0 = 376.73 Ω. Using the simulated s-parameters, the effective refractive index (n_{eff}) and impedance (Z_{eff}) of the disk can be obtained using the following equations [105]:

$$n_{eff} = \pm\left(\frac{1}{kh}\cos^{-1}\left[\frac{1}{2S_{21}}(1-S_{11}{}^2-S_{21}{}^2)\right]+\frac{2\pi m}{kh}\right) \tag{2.1}$$

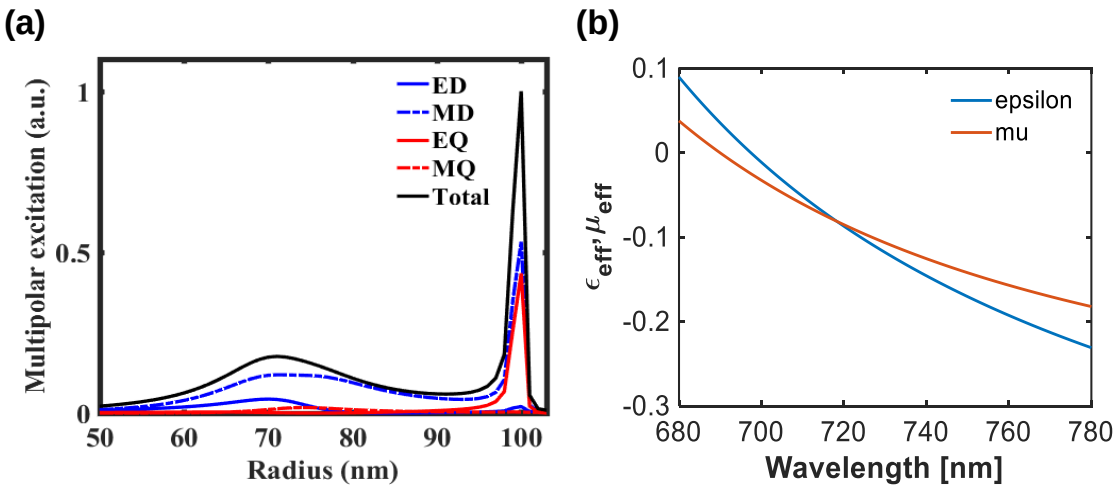

Figure 2.3 (a) Calculated multipolar decomposition under plane wave excitation with different disk radii, and (b) effective medium parameters [69].

$$Z_{eff} = \pm\left(\frac{(1+S_{11})^2 - S_{21}{}^2}{(1-S_{11})^2 - S_{21}{}^2}\right)^{1/2} \tag{2.2}$$

where $k=2\pi/\lambda$ is the wavenumber, h is the height of the nanodisk, and m is an integer. Using the n_{eff} and z_{eff}, the effective permittivity (ε_{eff}) and permeability (μ_{eff}) can be obtained easily with the following relations;

$$\varepsilon_{eff} = \frac{n_{eff}}{Z_{eff}}, \quad \mu_{eff} = n_{eff} Z_{eff} \tag{2.3}$$

It is noticeable that when the disk diameters are around 80 to 192 nm, owing to the excitation and overlap between ED and MD, an artificial magnetic response occurs by impedance matching the permittivity and permeability of the disk. As the ED and MD are relatively weak in this diameter region, the 2π-phase response can be achieved with high transmission. Using the effective medium approach, the phase response of the transmitted light, after passing through the nanodisk, can be obtained as [29]: $\phi = \frac{\omega}{c} n_{eff} h$, where n_{eff} is the effective refractive index of the disk and h represent the height of the disk. The light propagates through the disks with different sizes in a non-identical manner, as a result, various effective refractive index is generated. From Fig. 2.3(b), the calculated effective refractive index of 130 nm disk (diameter) is ~0.1 which is equivalent phase response of π/10 at the operating wavelength of 715 nm. Also, the calculated effective refractive index of 80 nm disk (diameter) is ~0.5, which leads to equivalent phase response of ~π/2. These estimated phase delays are consistent with 2D phase profile calculated in Figure 2.2(b). Therefore, by using different n_{eff}, phase response from 0 to 2π can be achieved.

2.2.2 Wavefront Manipulation with Large Deflection Angle

The schematic of the shorter supercell is shown in Fig. 2.4(a) where the nanodisks diameter varies from 90 to 172 nm. Individual nanodisks show slightly off-resonance phenomena followed by effective medium properties and show the corresponding phase responses at 680 nm wavelength. At the operating wavelength there is a minimal contribution of ED and MD to achieve the near-unity transmission and 2π-phase response. It is noticeable that individual nanodisks show near-unity transmission and each of them is responsible for phase shift from 0 to 2π with π/4 increments. The simulated transmission spectra are shown in Fig. 2.4(b) for different diffraction orders. It shows

that 0th order transmits only 5% of incoming light and around 58% of light transmits through the other diffraction orders at the operating wavelength of 680 nm. The proposed eight-disk supercell theoretically provides the deflection angle of 16.50°.

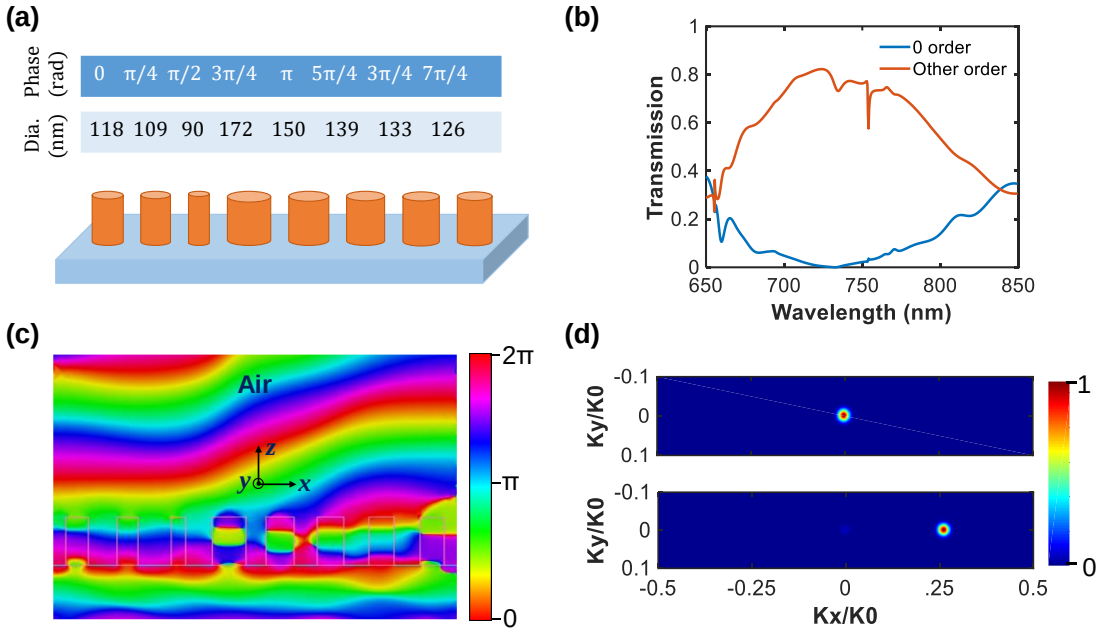

Figure 2.4 (a) Schematic of the smaller supercell which consists of eight nanodisks, where each of them is responsible for phase shift from 0 to 2π with π/4 increments. (b) Simulated transmission spectra for different diffraction orders. (c) Simulated phase profile obtained by the metasurface resulting in a diffraction angle of 15.66° at 680 nm wavelength, and (d) simulated far-field profiles of the incident light intensity (top) and transmitted intensity (bottom) [69].

By arranging the nanodisks in phase increment 0 to 2π, the propagating wave through the shorter supercell shows the larger wave bending (Fig. 2.4(c)). The wave propagation through the gradient metasurface is shown in Fig. 2.4(c). It is known that the diffraction angle of the gradient metasurfaces can be obtained by following Snell's law [92]:

$$n_t \sin\theta_t - n_i \sin\theta_i = \frac{\lambda}{2\pi}\frac{d\phi}{dx} \tag{2.4}$$

where θ_i and θ_t are the incident and diffraction light angles, respectively. The refractive indices of the surrounding media of the incident and transmitted sides are defined by n_i and n_t, respectively. The operating wavelength is defined by λ, and $d\varphi/dx$ indicates the

phase gradient. The individual phase of the unit cell is defined by $d\varphi$ and the period of the unit cell is defined by dx. According to equation 2.4, by reducing the unit cell size and increasing the phase of the individual unit cell, the deflection angle can be increased significantly. Considering our 8 nanodisk supercell which provides $d\varphi$ equals to $\pi/4$ and the dx equals to 300 nm, and according to equation 2.4, our theoretically proposed eight nanodisks supercell provides the deflection angle of 16.50°. As can be seen in the far-field intensity of the shorter supercell, shown in Fig. 2.4(d), incident light (top) is fully transmitted through the +1 order of diffraction (bottom) where the calculated deflection angle is 15.66° ($\theta = \sin^{-1}(k_x / k_0)$). Increasing the phase gradient rises the deflection angle, however, it reduces the transmission and deflection efficiency [70]. The calculated transmission, diffraction and deflection efficiencies are 87%, 83% and 72%, respectively, which are the highest values as compared to the reported silicon metadevices in the visible range [93, 106].

To verify the concept experimentally, we have fabricated and tested the metasurface. The metasurface fabrication requires several sequential steps. The block diagram of the sequential fabrication steps is shown in Fig. 2.5. The details of the standard metasurface fabrication process that I have followed to fabricate in this work, as well as for other works in this thesis has been given below.

1. Cleaning the substrate (glass) with acetone followed by isopropanol and de-ionised water for several minutes.
2. Cleaning the top surface of the glass substrate with the oxygen plasma.
3. Deposited the a-Si on top of the glass substrate using the PECVD process. The a-Si thickness was maintained by running a dummy a-Si deposition for a short time, and then measured deposited sample thickness with the ellipsometer. The optical properties of the a-Si were also measured with the ellipsometer, which I used for numerical simulation purposes.
4. Spin-coated the positive electron-beam zep-photoresist on top of the a-Si followed by the pre-exposure bake.
5. Spin-coated the spacer to avoid the discharging issue due to dielectric a-Si material.
6. Electron beam exposure to pattern the desired structure.

7. Performed the developing with the zep-developer followed by rinsing with isopropanol and de-ionised water to remove the exposed area.
8. Deposited the Chromium (Cr) using the electron beam thermal evaporator for the masking purpose.

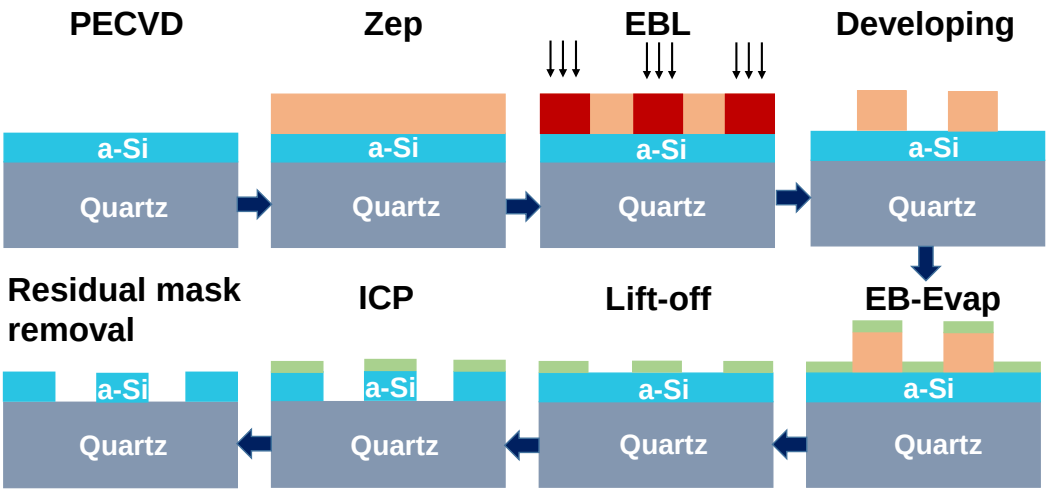

Figure 2.5 Step-by-step fabrication procedures for silicon metasurface [69].

9. Performed the lift-off using zep-remover followed by acetone, isopropanol, and de-ionised water, which helps to completely remove the zep from top of the a-Si surface.
10. Performed the silicon etching using the inductively coupled plasma - reactive ion etching (ICP-RIE).
11. Finally, removed the residual of Cr using the Cr-etchant followed by rinsing with isopropanol and de-ionised water.

Please note, the fabrication parameters such as time duration, temperature, and gasses flow rates for different steps vary based on the resist, developer, and some unknown factors as well.

A Scanning Electron Microscopy (SEM) image of the fabricated periodic supercell structure, consisting of eight nanodisks is shown in Fig. 2.6(a). The total area of gradient metasurface is 90×90 μm^2. The below zoomed area indicates the eight nanodisk-based supercell. The experimentally measured transmittance is depicted in Fig. 2.6(b), where the 0^{th} order shows the transmittance of only 12.5% and the other orders of 44.5% at

operating wavelength 680 nm. The experimentally measured transmission efficiency of the proposed shorter supercell is 57%. However, transmission efficiency can be improved by reducing fabrication imperfections. These differences could occur due to several factors such as uneven circular shape of the disks, surface roughness of the disks, uneven side walls and so on. Due to smaller size of the fabricated supercell then the expected one, the operating wavelength moves to the shorter wavelength. The transmission measurement was carried out by using a home-built transmission setup, shown in Fig. 2.6(c).

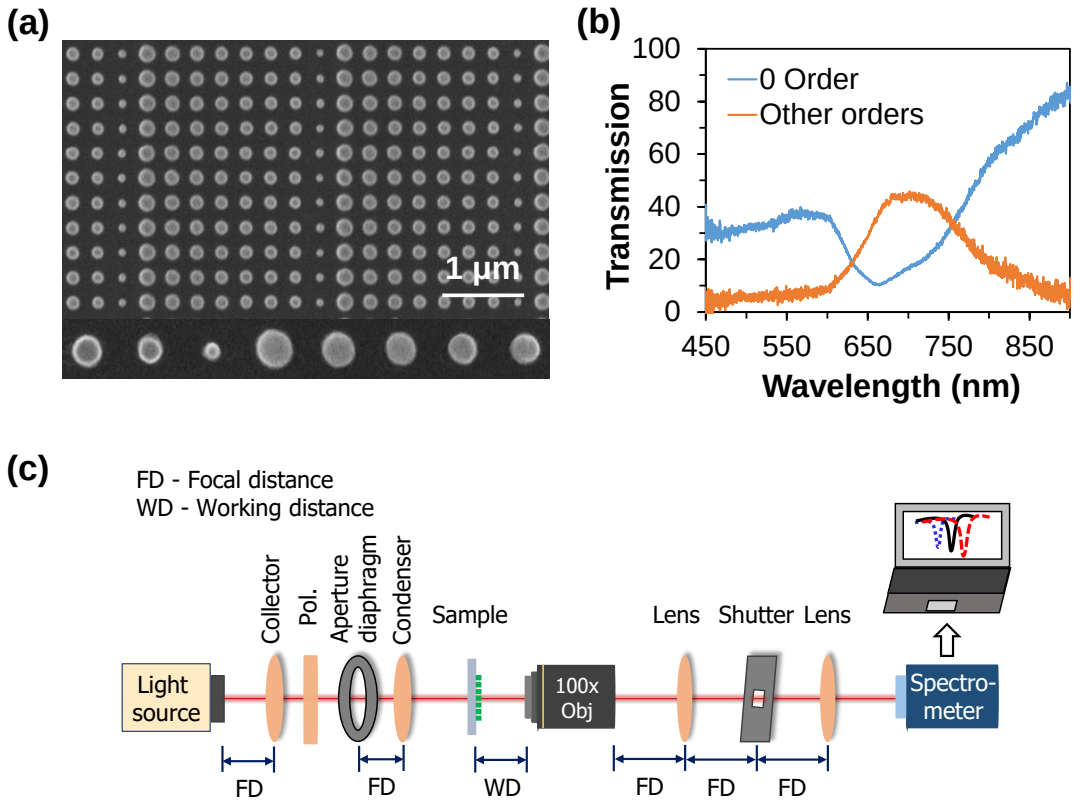

Figure 2.6 (a) SEM image of the fabricated metasurface, which consists of eight nanodisks and corresponds to the phase shift 0 to 2π with π/4 increments. (b) Experimental measurement of transmission spectra for zero and other diffraction orders, and (c) the schematic of the experimental transmission setup [69].

A halogen lamp has been used as a white light source. An aperture diaphragm has been used which transmits only the wave vectors that are parallel to the light path. A polariser has been used to control the polarisation states of the incoming light. The measured metadevices have been fabricated in an array of supercells and the total fabricated

gradient metasurfaces size was 90×90 μm^2. The samples have been illuminated from the back side, and 5x and 100x objectives have been used to capture the zero and other orders light. As our metadevice is a blazed grating, so it is important to use 100x objective to capture all the incoming light passing through the device. Otherwise, the light will bend at a large angle and all the incoming light will not be captured with smaller objectives. Finally, OceanOptics® (USB4000-VIS-NIR) visible spectrometer has been used to observe the transmission spectrum.

The beam deflection measurement was carried out by the experimental set-up shown in Fig. 2.7(a).

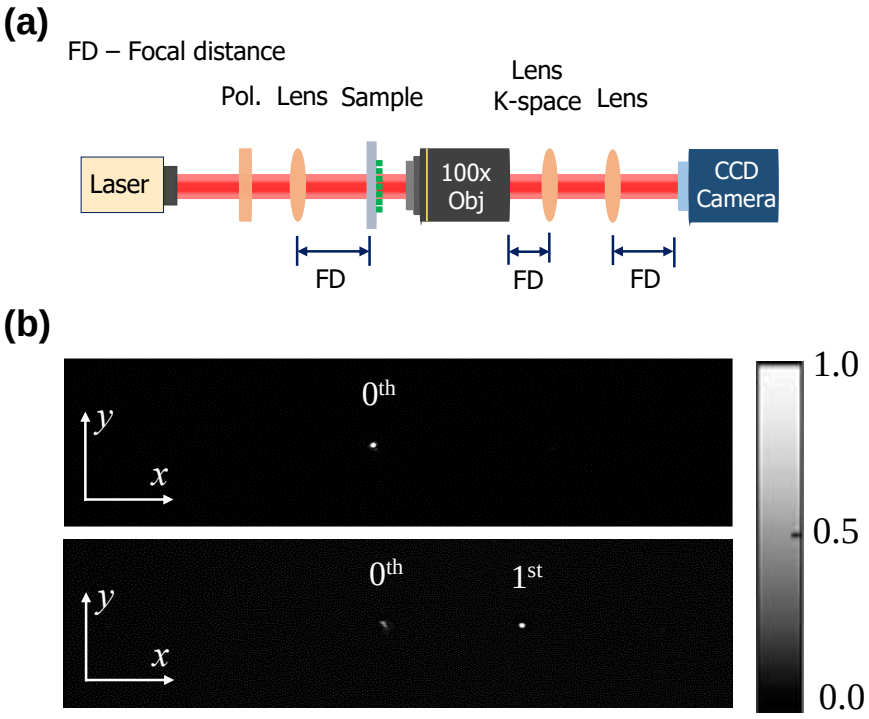

Figure 2.7 (a) The schematic of the measurement set-up to investigate the beam steering by far-field analysis, and (b) experimental far-field profile of the incident (top) and transmitted intensity (bottom) captured by a CCD camera [69].

A tuneable femtosecond laser (pulse duration of 200 fs with the repetition rate of 80 MHz) has been used as a light source. The spectral full-width-half-maximum of the laser line is 4.4 nm. We have used the 100x objectives to collect the transmitted light through the sample. The k-space measurement environment has been established by placing a lens at the focal distance behind the objective, and another lens is placed to image the back focal

plane in real space. This real and k-space measurement has been carried out by altering (keeping and removing) the lens. In the end, a CCD camera was placed at a focal distance from the real-space measuring lens to capture the far-field images. The experimentally measured far-field intensity profile is shown in Fig. 2.7(b). The experimental measurements are in good agreement with the numerical simulations where the incident light intensity (top) is fully transmitted through the +1 order of diffraction (bottom), and the measured deflection angle is 15.50^{o}. Moreover, the experimentally measured deflection efficiency is 43%.

For the LDA metagrating, it exhibits low transmission and diffraction efficiency. However, the transmission and diffraction efficiency can be improved by reducing the deflection angle. It is worth mentioning that deflection angle can be controlled in various ways such as changing the environment medium refractive index, angular light incident, increasing the supercell length, and increasing the phase coverage of the supercell [92]. However, changing the embedding medium and the incident angle have a negligible effect on changing deflection angle whereas increasing supercell length or decrement of phase discretisation within the same supercell length can decrease the deflection angle. Increasing supercell length, which is equivalent to increasing the number of nanodisks, leads to a smaller phase gradient of the individual unit cell that can cover 0 to 2π phase response. As a result, in line with the Snell's law [92], propagating wave will deflect with a small diffraction angle (see Eq. 2.4). Here, we further demonstrated this effect with a supercell consisting of fifteen a-Si nanodisks and demonstrated the high-efficiency meta-deflector.

2.2.3 Wavefront Manipulation with Small Deflection Angle

The schematic of a large supercell is shown in Fig. 2.8(a). The supercell consists of 15 a-Si nanodisks where the nanodisk diameters vary between 80 nm to 192 nm. The transmission spectrum corresponding to the individual nanodisk is shown in Fig. 2.8(b). From Fig. 2.8(b), it is clearly noticeable that the chosen nanodisk shows a strong resonance before the operating wavelength of 715 nm. The closest strong resonance occurs at 707 nm wavelength for the maximum larger disk diameter of 192 nm. Furthermore, individual nanodisk shows almost near-unity transmission response which is one of the key criteria for the transmissive metadevices. Previously reported deflection metadevices shows minimum transmission efficiency because of their chosen individual

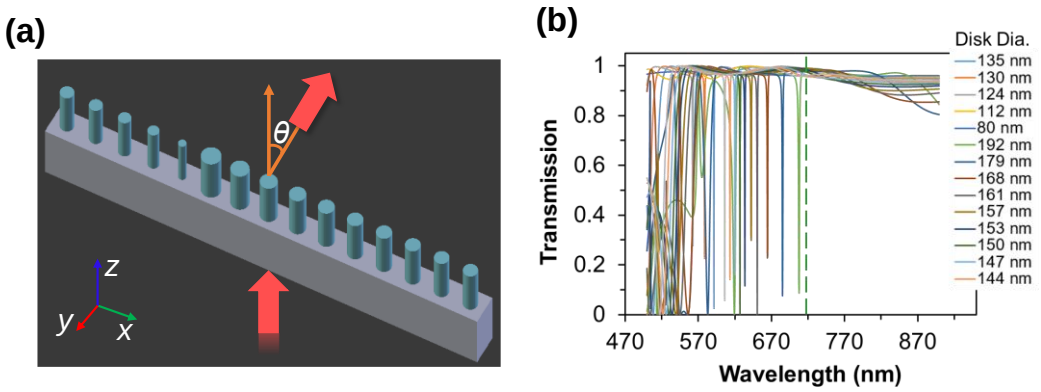

Figure 2.8 (a) Schematic of fifteen nanodisks based large supercell-based deflector, and (b) full-transmission spectra for individual nanodisks [69].

nanodisk shows less transmission. Therefore, the overall transmission efficiency of the gradient metasurfaces also reduced significantly [92, 93]. However, the transmission efficiency of a meta-deflector could be improved by efficiently choosing the highly transmissive nanodisk. Individual nanodisks transmission and phase response at an operating wavelength of 715 nm are depicted in Fig. 2.9(a). It demonstrates that individual nanodisk exhibits almost near-unity transmission, which leads to the high transmission as a supercell. By arranging the 15 nanodisks in a phase increment from 0 to 2π, the full transmission spectra of the proposed gradient metasurface are shown in Fig. 3b. According to Fig. 2.9(b), the 0^{th} order transmission of the proposed gradient metasurface is 0%, while the other orders lead to the transmittance of ~ 95% at the operating wavelength of 715 nm, whereby the calculated transmission efficiency is 95%. As can be seen, instead of passing incident light in normal 0^{th} order, here incident light is transmitting with other orders, which is a clear indication of incident light bending. The wave propagation through the gradient metasurface is shown in Fig. 2.9(c). The 15 nanodisks based supercell where $d\varphi$ equals to $\pi/7$ and dx equals to 300 nm leads to the calculated deflection angle of 9.80^{o} (according to equation 2.4). We have also investigated the far-field profile of the proposed gradient metasurface shown in Fig. 2.9(d). The far-field profile of the incident light intensity is shown at the top and the deflected beam intensity for +1 diffraction order after passing through the proposed gradient metasurface is shown at the bottom. The calculated diffraction efficiency is 100%, and the deflection efficiency is 95%, whereby both values demonstrate a clear improvement in deflection efficiency, as compared to the recently reported works [93, 107]. Also, the calculated deflection angle is 8.50^{o}.

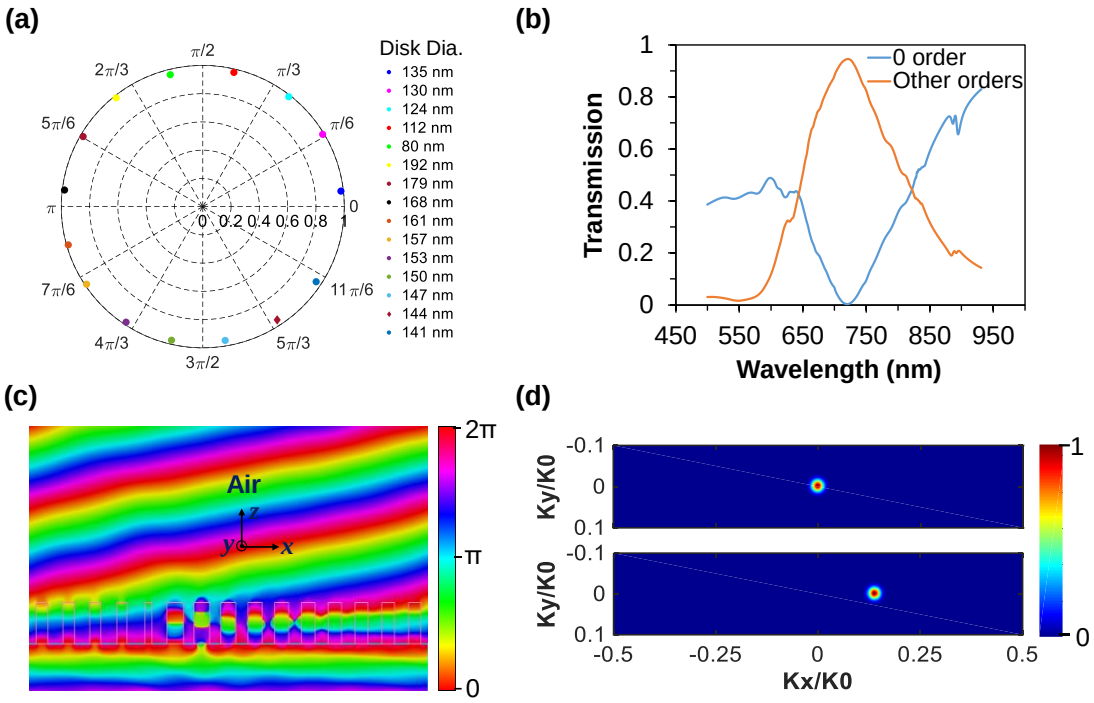

Figure 2.9 (a) Transmittance and phase in polar format at the operating wavelength of 715 nm. (b) Simulated transmittance spectra for different diffraction orders. (c) The simulated phase of a plane wave propagating through the metasurfaces corresponding to a diffraction angle of 8.50°. (d) Simulated Far-field profiles of the incident light intensity (top) and transmitted light intensity (bottom) [69].

The SEM of the fabricated large supercell is shown in Fig. 2.10(a). The total area of each gradient metasurface is 90×90 μm^2. The experimentally measured 0^{th} order transmittance of the proposed gradient metasurface is only 5% while the other orders transmittance is 78% at 715 nm (Fig. 2.10(b)). The measured transmission efficiency (ratio of the transmitted light to the incident light) is 83%, which is the highest reported value as compared to the recently reported metadevices [92, 106, 108]. It indicates the incident light wave is deflecting after passing through the gradient metasurfaces. The far-field profile of the incident light intensity is shown on top and the deflected beam intensity for +1 diffraction order after passing through the proposed metasurface is shown on the bottom (Fig. 2.10(c)). It can be seen that most of the light is transmitted to the +1 diffraction order, while the other orders are minimal. The measured beam-deflection angle is 8.40°, which shows an excellent agreement with our simulated deflection angle, shown in Fig. 2.9(d). Also, the measured deflection efficiency is 71%.

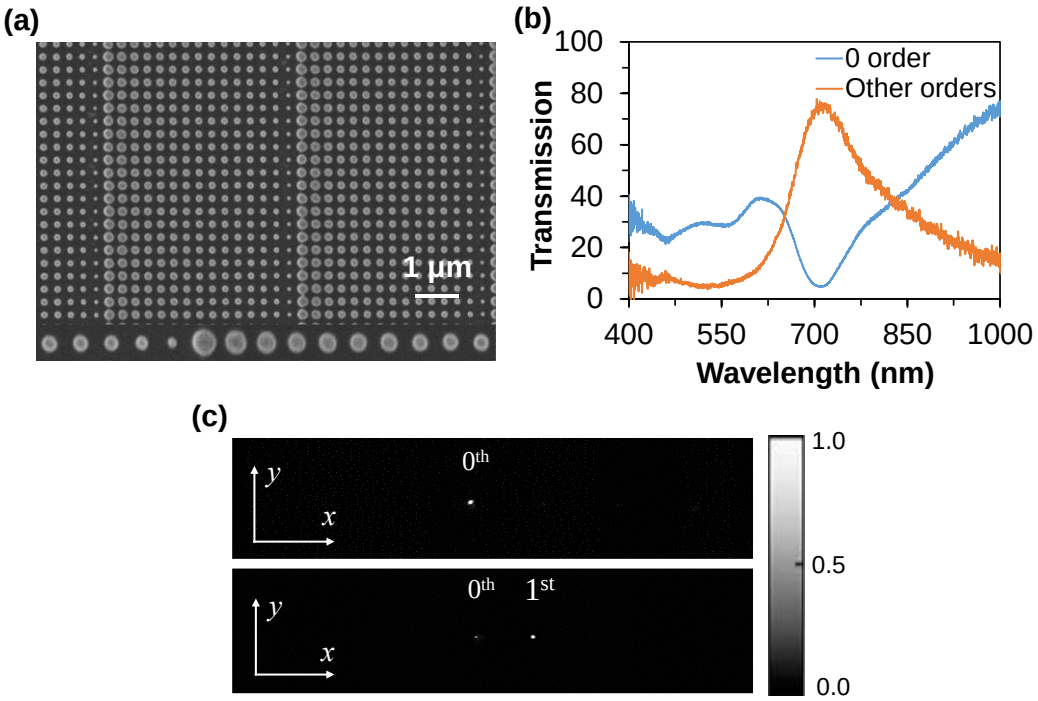

Figure 2.10 (a) SEM image of fabricated 15-disk supercell based metasurfaces with 90×90 μm^2 total size. (b) Experimental measurement of transmission spectra for zero and other orders. (c) The experimental investigation of the far-field profiles of the incident light intensity (top) and transmitted light intensity (bottom) captured by a CCD [69].

Comparing the large and small deflection angle based meta-deflector, it is clearly noticeable that small deflection angle based meta-deflector exhibits high transmission, diffraction, and deflection efficiency. This is because of large number of phase discretisation level is used in the small deflection angle-based supercell, therefore the coupling between the neighbouring meta-atoms is more uniform. This further leads to improve device performance.

2.2.4 Advanced Wavefront Control with 3π-Phase Gradient Meta-deflector

Finally, we show that the deflection angle/ orders of the metadevices can be controlled significantly keeping the supercell length unchanged but, increasing the phase response of the supercell. The SEM of the fabricated sample with the increasing phase response (0 to 3π) within the fifteen nanodisks supercell is shown in Fig. 2.11(a). The proposed 3π metadevice consists of 15 a-Si nanodisks where the first eight nanodisks cover the 0 to 2π (red-dotted area), and rest of the nanodisks cover 0 to π phase profile (green-dotted

area). This is working as a single large grating which consists with two different small gratings and there is no phase discontinuity between them. By alternatingly placing 8-disk unit cell and 7-disk unit cell together to design the multi-order 3π supercell metasurfaces, we combine two different beam deflectors, i.e., beam deflector made by 8-disks-unit metasurface with deflection angle θ_1 and beam deflector made by 7-disks-unit metasurface with deflection angle θ_2. In such a case, they can be considered as working independently and adding transverse wave vectors k_1 and k_2 on the beam that illuminated at the 8-disk unit cells and 7-disk unite cells, respectively. Thus, we can divide the input beam into two parts with the proportion that can be controlled by the length and phase of the unit cell. Such a meta-deflector can multiplex the input beam into different parts and route them in different angles. Figure 2.11(b) shows the transmission and phase response of the individually chosen nanodisk. The individual nanodisk exhibits high transmission efficiency which enhances the overall efficiency of the device. The calculated transmission spectra for different diffraction orders are shown in Fig. 2.11(c).

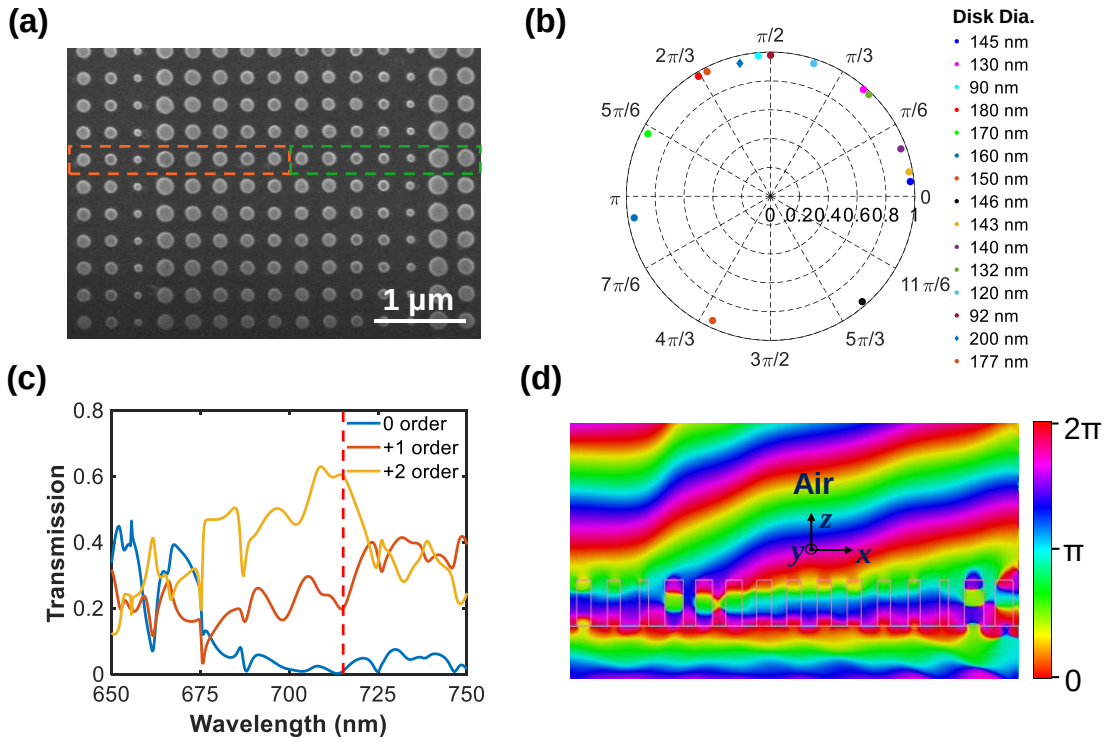

Figure 2.11 (a) SEM image of the fabricated 15-nanodisks supercell (3π-phase response) based metasurfaces with 90×90 μm^2 total size. (b) Transmittance and phase in polar format at the operating wavelength of 715 nm. (c) Simulated transmittance spectra for different diffraction orders. (d) Simulated wave propagation through the proposed metadevices where the nanodisks covered 0 to 3π-phase response [69].

According to Fig. 2.11(c), the proposed advanced meta-deflector transmits 23% of incoming light in $+1^{st}$ diffraction order and around 60% light diffracts to the $+2^{nd}$ diffraction order at the operating wavelength of 715 nm. The wave propagation of the proposed 15 nanodisks (3π phase) is shown in Fig. 2.11(d). Due to the large phase gradient of 1^{st} eight nanodisk provides beam deflection angle of 17.33^{o} while the lower phase gradient value of the remaining nanodisk bend the wave with a lower deflection angle of 9.80^{o}, respectively at operating wavelength 715 nm.

The experimentally measured transmission efficiency of the proposed gradient metadevice is 43% where the 0^{th} order and other orders show the transmittance of 7% and 36%, respectively at the operating wavelength of 633 nm (see Fig. 2.12(a)). Due to fabrication imperfection operating wavelength moves to the lower wavelength. The a-Si is highly absorptive for light with a wavelength of 633 nm. Therefore, it reduced the total transmission efficiency. We then investigated the far-field intensity profile from our meta-deflector, as shown in Fig. 2.12(b).

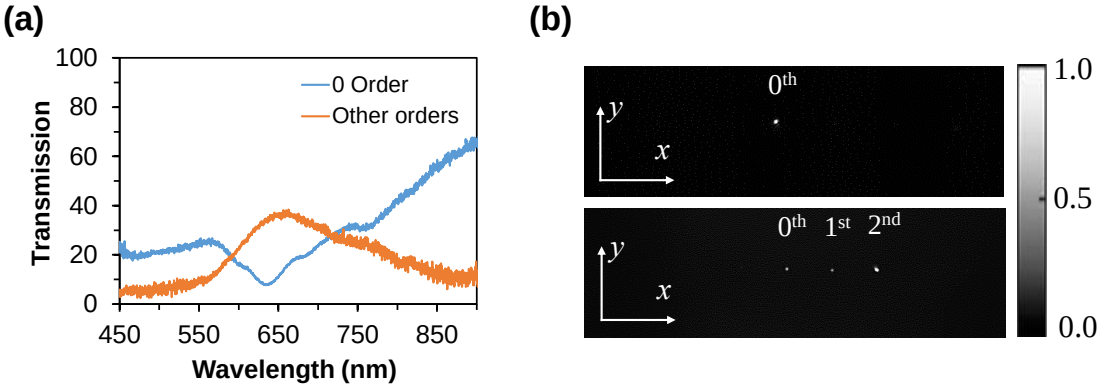

Figure 2.12 (a) Experimental measurement of transmission spectra for zero and other orders, and (b) the experimental investigation of the far-field profiles of the incident light intensity (top) and transmitted light intensity (bottom) captured by a CCD [69].

Due to the introduction of two different phase profiles (0 to 2π and 0 to π), the proposed metasurface shows light deflection not only in $+1^{st}$ order but, also $+2^{nd}$ order. It agrees well with our numerically predicted results (see Fig. 2.11(c)). Here, $+2^{nd}$ order appears due to π phase response of the last 7 nanodisks, corresponding to the $+1^{st}$ order diffraction from the 7 disks supercell. Light passing through the $+1^{st}$ and $+2^{nd}$ orders are 22% and 50%, respectively with the close deflection angle of 8^{o}. The measured deflection

efficiencies are 10% and 20% of the $+1^{st}$ and $+2^{nd}$ diffraction orders, respectively. The findings are comparable with the reported work of nonintuitive geometry-based beam splitters where two wavelength splitter and five wavelengths splitter experimentally show the deflection efficiency of 56.4% and 17.1%, respectively at the operating wavelength of 900 nm [109]. In the proposed deflector, propagating waves coming from two different phase profile arrangement is joining correctly and deflecting the wave. Such metadevice-based approach may have potential applications in beam multiplexing. As a result, by arranging the nanodisk from a lower phase gradient to a higher phase gradient, a wave can be bent significantly with a large deflection angle.

The performance comparisons of the reported meta-deflectors with the proposed one are shown in Table 2.1.

Table 2.1 Performance comparisons of the experimentally reported metadeflectors.

Characteristics	Disk Mode	Wave. (nm)	Trans. Effi.	Defl. Effi.	Defl. Angle	Ref.
c-Si based circular nanodisk (8 unit cells)	Resonance	532	71%	67%	19.27°	[92]
poly-Si based square nanoblock (8 unit cells)	Resonance	1550	36%	-	13.1°	[93]
High-index chalcogenide based rectangular meta-atom (8 unit cells)	Resonance	5200	75%	60%	15.1°	[96]
Liquid crystal based circular nanodisks (6 unit cells)	Resonance	745	-	50%	12.0°	[97]
a-Si based circular nanodisk (8 unit cells)	Resonance	705	-	45%	10.3°	[106]
a-Si based larger supercell (15 unit cells)	Off-resonance	715	83%	71%	8.40°	This work [69]
a-Si based shorter supercell (8 unit cells)	Off-resonance	680	57%	43%	15.50°	This work [69]
a-Si based larger supercell (15 unit cells with 3π phase)	Off-resonance	633	43%	10%, 22%	8.0°	This work [69]

2.3 Subwavelength Metasurface Resonators for Terahertz Wavefront Manipulation

The principle of wavefront manipulation at the THz frequency remains the same as visible wavefront manipulation, where besides the transmission/ reflection amplitude, 2π phase control is needed. One of the ways is to spectrally overlap two resonant modes to accumulate the 0 to 2π phase response. Another approach is to create the metaunits patch on top of the metallic ground plane with a dielectric spacer in between [11, 110-112]. While selecting the metaunits to cover the 2π phase response, it is important to check that the resonators are underdamped i.e. the radiative decay rate is greater than the nonradiative decay rate [113, 114].

As we briefly discussed in the previous section that the phase discretisation level significantly improves the device performance, however, it also makes the fabrication process more complex. Due to large number of different unit-cells, it has a higher chance to impose fabrication imperfections. Moreover, the spatial dispersion and discretisation error also become more prominent. However, recently, Wang *et al.* proposed that by utilizing highly subwavelength metaunits ($<\lambda/14$), we can avoid these issues, and can significantly improve the device performance [115]. The major advantages of more subwavelength metaunits are localised response, the effect of mutual interaction is weaker, and minimise the spatial dispersion [113, 116].

Generally, at a lower frequency, the resonators can be highly miniaturised due to several reasons, such as high-index substrate, high-conductivity metals, the ability of reactive lumped elements, and so on [117-119]. However, the reactive lumped elements are not available at the THz spectral range, therefore the resonators miniaturisation strongly depends on the novel design of distributed structures. Usually, the reported sub-wavelength resonator size is around $\sim \lambda/5$, which has been utilised for wavefront manipulation at the THz frequencies [120, 121]. Very recently, deeply sub-wavelength resonators around $<\lambda/10$ has been demonstrated at the THz frequencies. These structures work based on the concept of spoof localised surface plasmon or scaling down the meander line structures [122-124]. However, it is yet to explore whether these concepts can be used for efficient wavefront manipulation since the effect of overdamping in these deep-subwavelength resonators was not specifically examined. At high frequency, the conductivity of the metal decreases, therefore it is highly challenging to make the resonators deeply-subwavelength without being overdamped.

In this work, we numerically and experimentally demonstrated that reshaping the capacitive gaps between the metallic patches is a suitable approach to create deeply subwavelength metaunits. We have shown the route to scale down the size of the resonator to $\lambda/25$, while remaining underdamped. Therefore, this approach enables mitigating the undesirable effects due to sparse discretisation, including spatial dispersion, mutual interaction, and discretisation error.

2.3.1 Design Concept

The traditional rectangular metaunit is shown in Fig. 2.13(a). The individual metaunit supports a series of resonances, and the impedance contribution of each resonance can be described by an effective RLC circuit. There are two ways to reshape the metaunit, which helps to red shift the resonance feature. The first technique is to reduce the width of the metallic patch which will increase the effective inductance (see Fig. 2.13(b)). Another technique is to reduce the gap between metallic patches, which will increase the effective capacitance (see Fig. 2.13(c)).

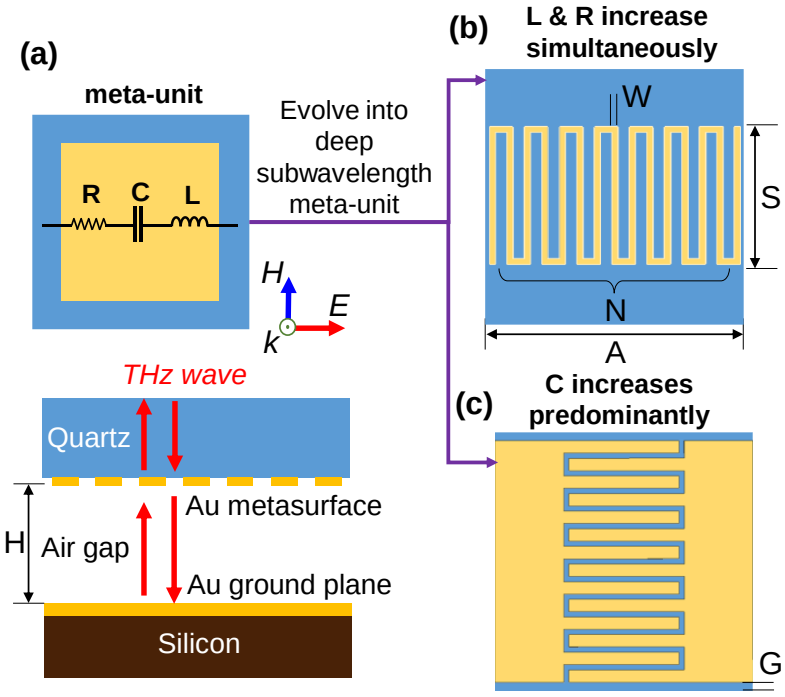

Figure 2.13 (a) Schematic of a reflective metasurface. The metallic patches can evolve into deep subwavelength metaunits by either (b) increasing the effective inductance L using a meander line or (c) increasing the effective capacitance C with a meander gap (interdigital capacitor) [79].

The optimised parameters of the designed metasurface are lattice constant A = 15 µm, width W = 0.3 µm, height of the air gap H = 6 µm, G = 1µm, finger length, S = 10 µm, and the number of interdigitated fingers N = 14. The thickness of the gold ground plane is 200 nm, and that of the patterned metallic layer is 100 nm. It is worthy to mention that, for a better comparison, we have maintained both designs of metaunits with the same lattice constant, number of fingers, width, finger length, as well as height H of the air gap. A similar type of shape transformation for the metallic patch to increase the effective inductance can also be applied to the dielectric gaps between patches to increase the effective capacitance. The patch can be transformed to a well-known meander line to increase the inductance [117, 125-127], while the gap can be transformed into a meander gap [128-130].

Due to high Ohmic loss of the metal, it is important to investigate the non-radiative decay rate which generally quickly exceeds in the meander line structure, as it becomes longer and thinner. Therefore, the resonance becomes overdamped, and achieving 0 to 2π phase response is difficult. To further investigate, conductivity effects on the reflection and phase for the meander line-based structure are shown in Figs. 2.14(a, b).

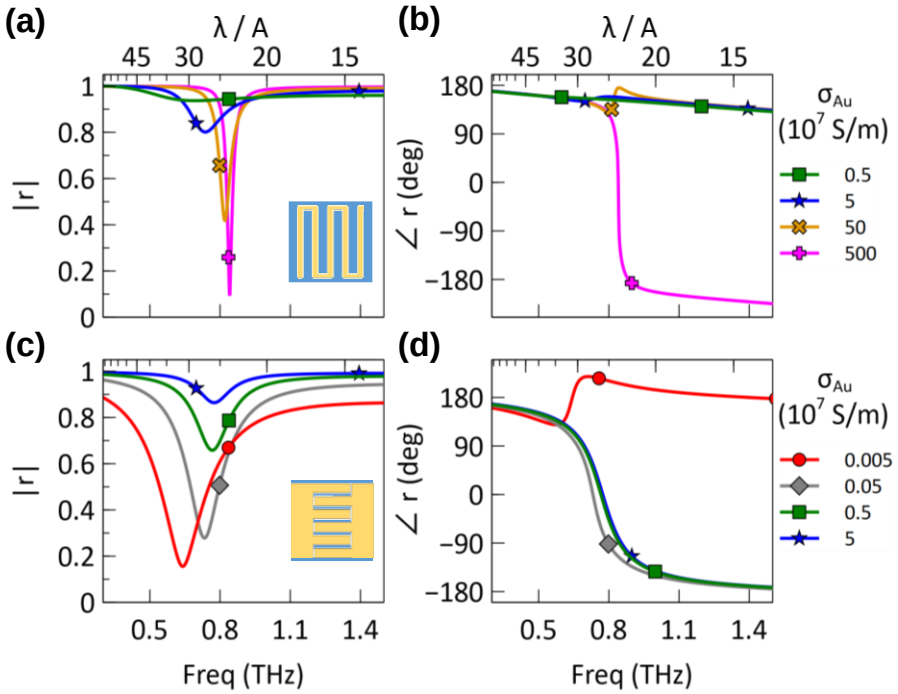

Figure 2.14 The simulated reflection (a) amplitude and (b) phase spectra of a metasurface with a meander line structure for different values of the conductivity of gold. The simulated reflection (c) amplitude and (d) phase response of a metasurface with a meander gap structure for different values of the conductivity of gold [79].

At the realistic conductivity value (σ_{au} = 5×106 - 5×107 *S/m* [131]), it exhibits a significant overdamp of the resonance (Fig. 2.14(a)). Even increasing the conductivity three orders of magnitude compared to the realistic conductivity, still meander line structure exhibits close to critical damping (near perfect absorption) due to intrinsically low radiative decay rate (Fig. 2.14(b)). On the other hand, conductivity effects on the meander gap design are shown in Figs. 2.14(c, d). The meander gap design shows a nice 0 to 2π phase response at the realistic conductivity value as well as for one order of magnitude lower than the realistic σ_{au} (Fig. 2.14(d)). From the linewidth of the resonance spectrums, it is also clearly visible that the radiative decay rate in the meander gap structure is much higher compared to the meander line structure. Therefore, for the further meta-deflector design we have considered meander gap based metasurface structure.

2.3.2 Simulated Beam Deflector for Terahertz Wavefront Manipulation

As we briefly discussed in the previous sec. 2.2 that, for efficient wavefront manipulation besides the amplitude (either transmission or reflection), it requires to have 0 to 2π phase coverage. In meander gap design, by varying the finger length *S*, we have achieved 0 to 2π phase profile while maintaining the high reflection efficiency for individual metaunit (Figs. 2.15(a, b)).

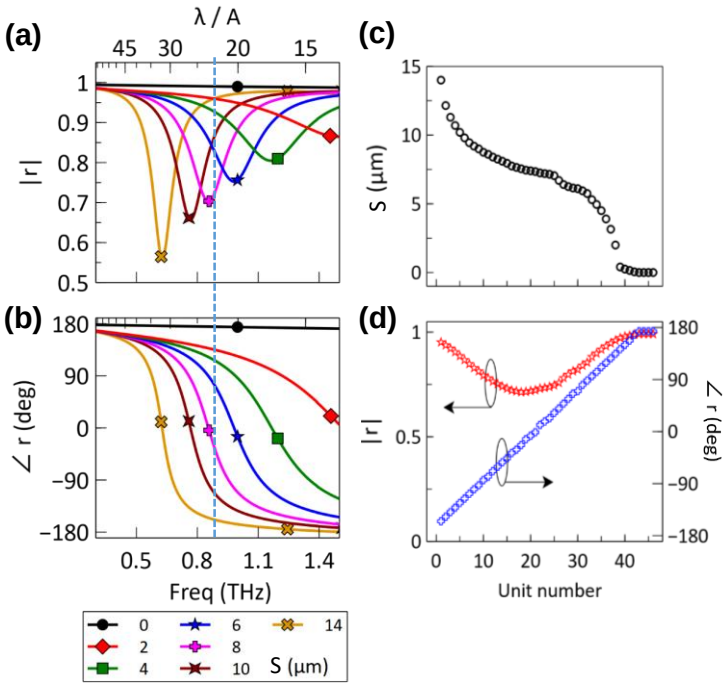

Figure 2.15 Simulated (a) reflection, and (b) phase response of the meander gap metasurface as a function of finger length S. (c) The chosen finger lengths over a supercell

of a metasurface beam deflector, and (d) the corresponding local reflection coefficients at 0.88 THz [79].

We have considered σ_{au} = 5×106 *S/m* which is one order of magnitude lower than the available σ_{au} value in the literature, considering the various loss mechanism such as surface roughness, grain boundary effects and the finite thickness effect of the gold film [131, 132]. It is worthy to note that, a large conductivity value can easily lead to 2π phase response. The challenging part is to achieve 2π phase profile with a low conductivity value. Due to the increase of finger length, the resonance frequency shows red shifts as shown in Fig. 2.15(a), and the corresponding phase response is shown in Fig. 2.15(b). Also, the resonant wavelength to the lattice constant becomes larger than 30 (Figs. 2.15(a, b)). We have used the Height H = 6 µm considering the experimental point of view. However, by increasing the heigh (H = 6 to 10 µm), we can even push the miniaturisation to 40A, which means the size of the resonator could be λ/40.

The proposed meta-deflector consists of 46 metaunits based supercell. The finger length of the metaunit is varied to cover the 2π phase response. The finger length of the metaunit (Fig. 2.15(c)), and its corresponding reflection amplitude and phase response (-180° to +180°) are shown in Fig. 2.15(d) at the operating frequency of 0.88 THz. The proposed metasurface works for y-polarised incidence. The size of the 46 metaunits based supercell is 690 µm, which leads to the calculated deflection angle in quartz being 13° at 0.88 THz. At this frequency, the size of the unit $A \approx \lambda/23$, and the capacitive gap $W \approx \lambda/1136$.

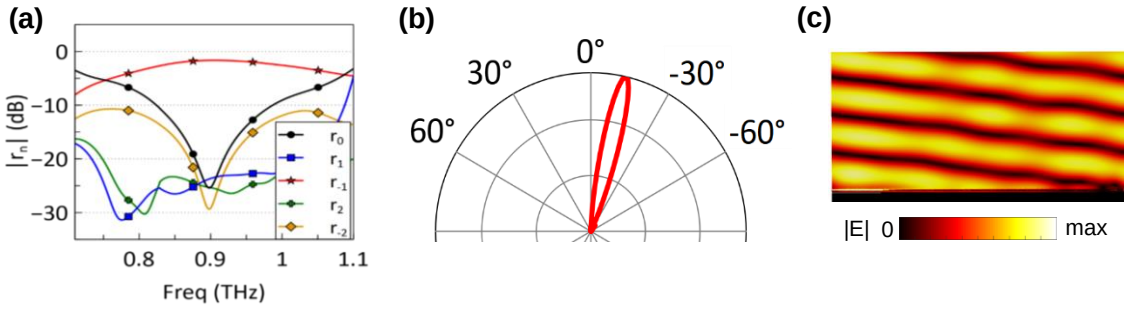

Figure 2.16 (a) Simulated reflection spectra for different diffraction orders. (b) Simulated far-field scattering pattern. (c) The time-averaged interference pattern of the incident and reflected electric fields [79].

The simulated diffraction coefficients of different diffraction orders are shown in Fig. 2.16(a). The operating wavelength slightly moves to 0.90 THz and exhibits the maximum light scattered towards the -1st diffraction order, 29% is lost as absorption and the remaining 3% is scattered in different diffraction orders. The far-field profile scattering profile is shown in Fig. 2.16(b). It exhibits the deflection of 13^{o} at the operating frequency of 0.90 THz. The electric field distribution is shown in Fig. 2.16(c), which exhibits nice beam bending.

2.3.3 Experimental Beam Deflector for Terahertz Wavefront Manipulation

To experimentally verify the highly subwavelength metaunit based beam-deflection, we have fabricated the metasurface using the advanced EBL technique. We have followed the standard fabrication steps as mentioned in sec. 2.2.2 to fabricate the sample. The fabricated metasurface area is 5×5 mm^2. It is well established that to fabricate the large micron size structure, generally photolithography is one of the promising techniques. However, photolithography technique require mask to pattern the structure, which is time consuming. Therefore, EBL is another alternative option to fabricate the structure. The main drawback of the EBL technique is its slow pattering time. Therefore, most of the fabricated metasurfaces area is in micrometre scale. THz applications generally require quite large pattering area (millimetre scale) which limits the use of EBL technique. However, in this work, we have used the advanced EBL technique to fabricate the 5×5 mm^2 pattering area within a very minimal pattering time (~ 2 hrs). In this structure, the challenging part is that we need a large patterning area as well as a nanometre scale gap size (300 nm). Therefore, we optimised the aperture size, step size, and doses in a way which allows the fast patterning as well as able to fabricate nanometre scale gap. In this work, we have used 30 kV EBL (Raith 150). We have used 3 nm Cr as an adhesive layer between the 1 mm thick quartz substrate and 100 nm gold surface. We have also used the zep photoresist for the patterning purposes. After developing the resist, the patterns were transferred to the Au film via ion milling. Finally, the resist was washed away. In parallel, another silicon substrate was covered by 200 nm Au, to act as a ground plane mirror. The photograph and dark-field microscopy images are shown in Figs. 2.17(b) and (c), respectively. From the dark-field microscopy image (Fig. 2.17(c)), it is clearly visible the different finger lengths, and a full supercell area along the x-axis. The SEM of the fabricated structure is shown in Figs. 2.17(d, e).

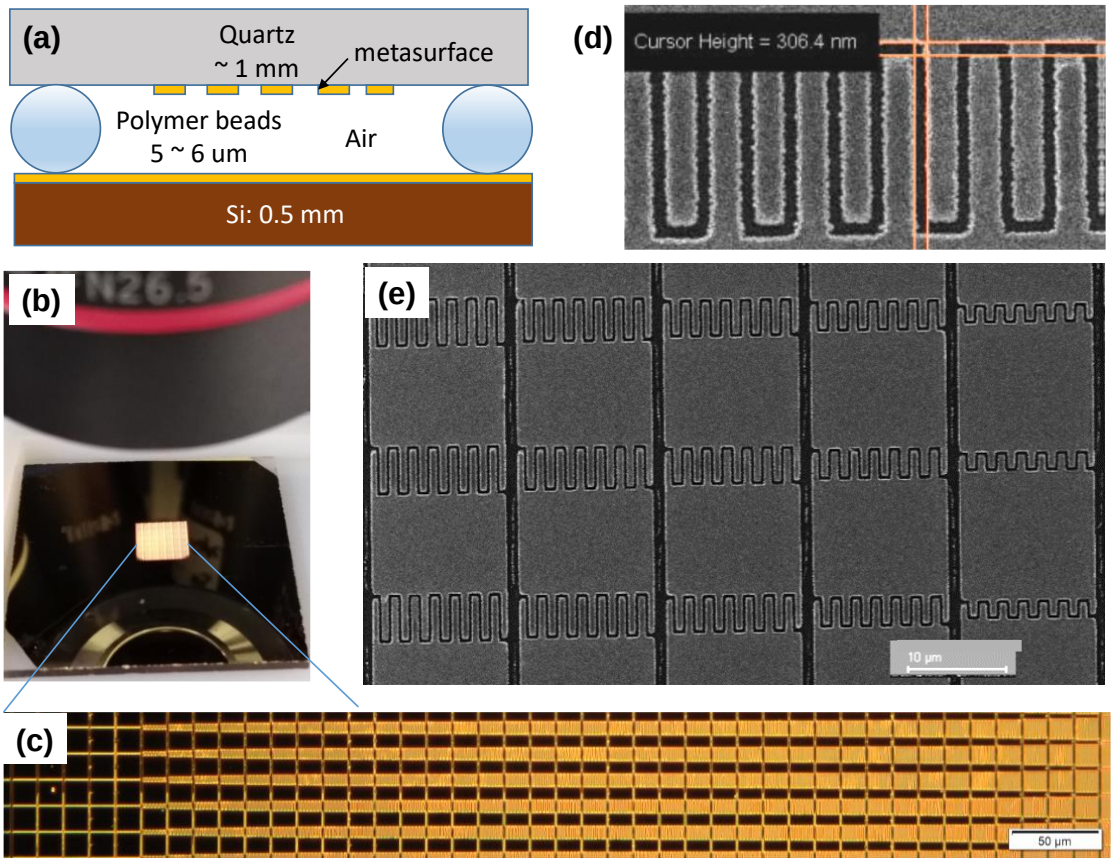

Figure 2.17 (a) Schematic of the metasurface sample. (b) Photograph, (c) dark-field microscopy image, and (d, e) scanning electron microscope (SEM) images of the fabricated sample [79].

The zoom view of the gap size is shown in Fig. 2.17(d), which confirms the fabricated meander gap size is 306 nm. To create an air gap, plastic balls with nominal dimensions 5–6 µm, commonly used as spacers in liquid crystal displays, were evenly distributed on the unpatterned regions of the metallic film (Fig. 2.17(a)). The metasurface sample was then covered with the ground plane substrate, and the two samples were bonded to each other using ultraviolet curing glue "Norland Optical Adhesive 60". To experimentally measure the deflection properties, we have used the angle-resolved THz time-domain microscopy [131], as shown in Fig. 2.18(a). A pair of fibre-based terahertz antennas were used as a transmitter and receiver. A rotator is used to control the incident and reflected light at a different angle (θ). The sample is positioned at the centre of the rotator. The light is transmitted at a normal incident angle, and the corresponding reflected light is captured by rotating the receiver in different diffraction angles. The experimentally measured angle-resolved spectra are shown in Fig. 2.18(b).

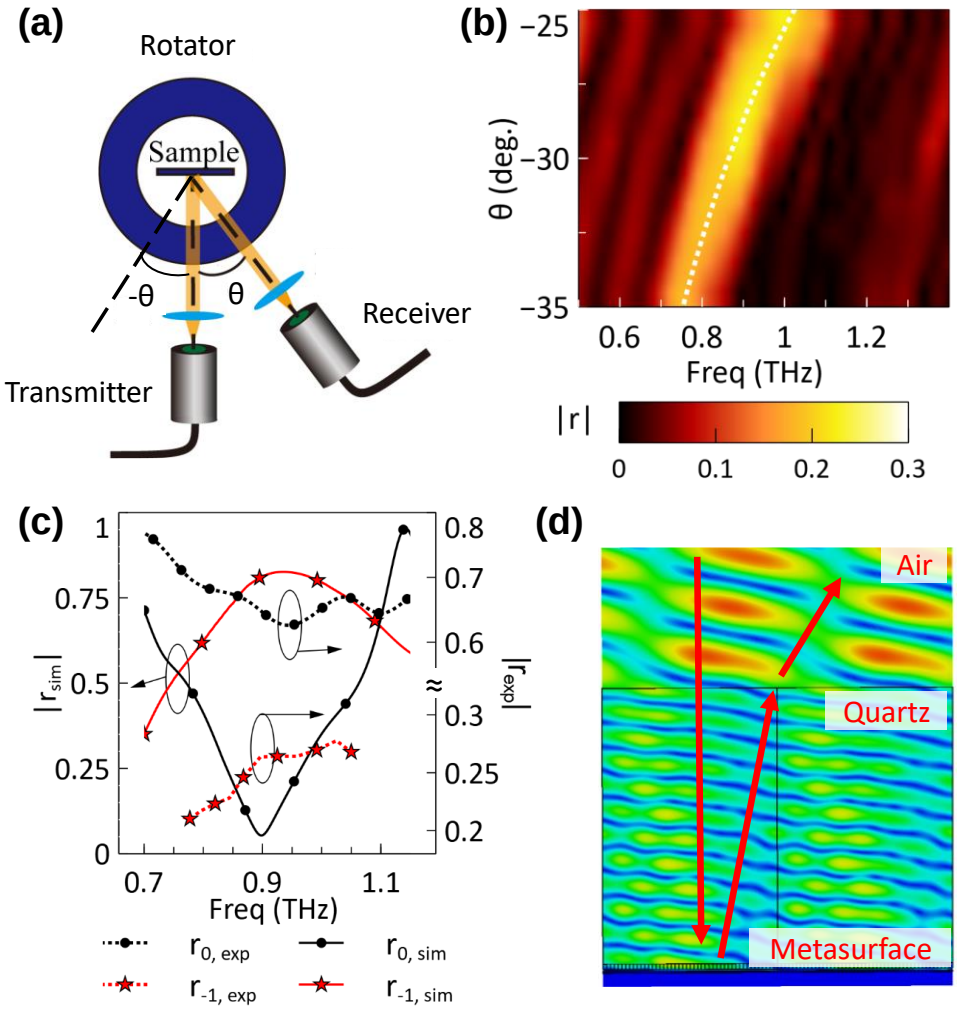

Figure 2.18 (a) Schematic of the experimental setup. (b) The measured angle-resolved reflection spectra. (c) Measured and simulated reflection spectra. (d) Simulated time-averaged field distribution of the sample with a 1 mm thick quartz substrate [79].

It is worthy to note that the deflection angle is -30° at 0.88 THz, which is larger compared to the deflection angle of -13° in quartz. This is because of the deflection angle is experimentally measured in an air medium. The measured and simulated reflection spectra in different diffraction orders are shown in Fig. 2.18(c). According to Fig. 2.18(c), we have experimentally shown that around 42% of incident light reflected secularly. The remaining 50% of light is lost due to absorption and spurious diffraction. The experimentally measured spectrum shows quite good agreement and exhibits a similar spectrum response to the numerically calculated results. Although, there are some discrepancies with the experimental and numerical values, however, this could happen due to several known and unknown factors, such as fabrication imperfections,

conductivity effect, surface roughness, uneven side walls, and so on. We have also further numerically proved that the proposed designed meta-deflector deflected the beam with -30^{o} at the air-medium which is well aligned with our experimental beam deflection angle result. Our numerical and experimental results demonstrates that the proposed metasurface perfectly works as a beam deflector, and that tailoring the capacitive gap is a practical strategy for constructing deeply subwavelength metaunits for metasurface devices.

2.4 Summary

In this chapter, I have numerically and experimentally showed the efficient wavefront manipulation at the visible and THz regimes. I have showed the deflection angle effects for the transmission and deflection efficiency at the visible wavelength. Later, optimised the 15 nanodisks based supercell which exhibits 95% transmission and deflection efficiency. I have also proposed another advanced beam deflector with 3π-phase gradient, which allows to multiplex the incoming beam and direct them to a large deflection angle. Finally, I have also demonstrated another deeply subwavelength mender-gap resonator based meta-deflector for efficient wavefront manipulation at the THz frequency. Utilising the advanced electron-beam lithography, the resonator size is reduced to $\approx \lambda/23$ with the capacitive gaps of $\approx \lambda/1136$. The proposed advanced mete-deflectors will pave the new possibilities for high-efficiency metadevices for the broad range of applications in the visible to THz regions.

Chapter 3

Diffractive Metagrating Based Optical Biosensor

The material in this chapter was in part presented in [74, 131].

Metasurface based sensing platform is one of the promising sensing technique in the optical sensing community due to its device miniaturisation, high-throughput, label-free detection capability, multiplexing facility, etc. [34, 41, 132, 133].

In this chapter, I will first present a hybrid metasurface based sensor in sec. 3.1. In the same section, I will also explain the optical sensing mechanism, and reasons for choosing diffractive metagrating based sensing platform. Subsequently, I will demonstrate a novel diffractive metagratings based optical sensing design concept and working principle in sec. 3.2. The diffractive metagrating based optical sensor is mainly divided into two parts based on their deflection angle and demonstrated the numerical and experimental refractive index measurement results in secs. 3.3 and 3.4. Finally, in sec. 3.5, I will demonstrate the functionalization process to detect the anti-Mouse IgG biomarker. Also, I will present the selectivity measurement and calculate the limit-of-detection of the proposed metagrating sensor.

3.1 Introduction

Over the last decade, significant progress in nanofabrication, nano-characterization, and computer modelling has led to the development of miniaturised sensing devices that allow the fast and reliable detection of molecules of interest [134-136]. The small footprint of miniaturised sensing devices has increased the appeal for their use in our daily life [137]. In particular, optical sensors are attractive due to their robustness, highly sensitive nature, and potential for use in wireless devices [138, 139]. To date, optical sensors have found a broad range of applications, including environmental monitoring, food safety, and medical diagnostics [133, 136, 139, 140]. Amongst the various optical sensing techniques in use, label-free sensing has been at the forefront of rapid and inexpensive detection paradigms [141]. Label-free sensing does not require chemical modification of the target molecule of interest, instead of using a receptor to capture the target through its binding properties [141, 142]. As high affinity and selectivity are desirable sensor properties,

biomolecules such as antibodies are frequently used as receptors due to their ability to recognise and tightly bind specific targets. Once target molecules have been bound, label-free sensors must then be capable of transducing these molecular interactions into a measurable signal. In optical sensors, this transduction occurs by encoding binding events into an optical signal via waveguides [143], micro-ring resonators [144], optical fibres [145], and metasurfaces [146, 147]. Amongst these platforms, optical metasurface-based sensors have thus far provided the highest potential for miniaturization as well as an accessible avenue for multiplexing of the analyte-fields [132].

Metasurfaces are ultrathin planar arrays of resonant nanostructures made of metallic or dielectric materials that can significantly manipulate light properties [3, 82, 148]. Resonant oscillations of free electrons in metallic nanostructures lead to localised surface plasmon resonances (LSPR), which exhibit strong field enhancement on the surface. Subsequently, the oscillation currents result in increased scattering at the resonant wavelength, whose spectral position is highly sensitive to the surface refractive index. The presence of analytes on the surface of the nanostructures can alter this surface refractive index. Therefore, plasmonic systems directly enable the transduction of target binding in label-free sensing platforms [147, 149]. However, the quality factor of LSPR resonances and therefore their spectral width is relatively broad, which limits the performance of LSPR-based sensors. More recently, replacing plasmonics with dielectric metasurfaces has enabled the generation of higher quality factor resonances. Dielectric metasurfaces can exhibit much narrower resonance spectral widths, including high-Q designs [150, 151]. They further allow for a larger sensing mode volume and engineering of the field profile. As a result, dielectric metasurfaces have enabled the development of highly sensitive sensing platforms [34, 133, 150, 151]. However, the hybrid (metal-dielectric) metasurface platform is another viable alternative, which can lead to a highly sensitive sensor, as well as a near-perfect absorber.

The schematic of a metal-dielectric (hybrid) metasurface platform is shown in Fig. 3.1(a), which exhibits a highly sensitive sensing response as well as work as a near-perfect absorber. We have used the gold mirror to prevent the transmission and used the a-Si nanodisk arrays on top of the gold mirror, which helps to excite the surface plasmon by scattering light through it at the normal incident. In the proposed hybrid metasurface structure, the suppression of the reflectance occurs due to the perfect matching of the electric dipole and magnetic dipoles, which is also known as impedance matching. At the

impedance matching wavelength, the proposed device shows near-perfect absorption, shown in Fig. 3.1(b).

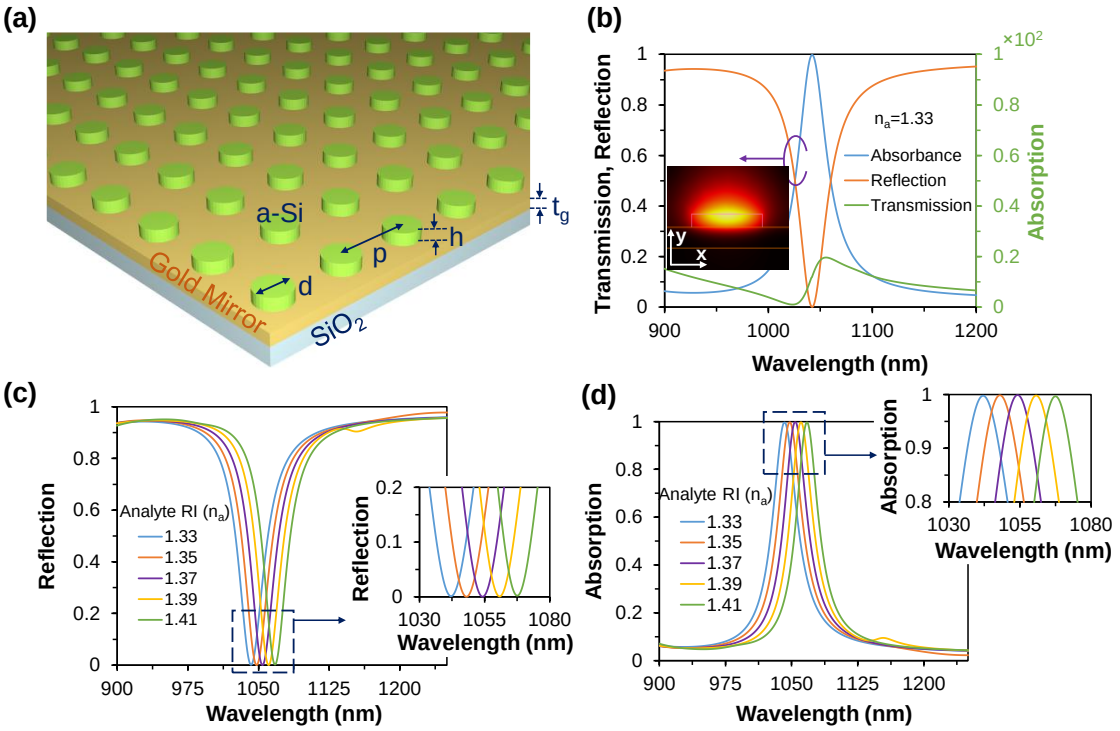

Figure 3.1 (a) Schematic of the hybrid metadevice, where the disk diameter, d = 230 nm, period, p = 670 nm, height, h = 50 nm, and gold thickness, t_g = 80 nm. (b) Absorption, reflection, and transmission spectra of the proposed metadevice with an embedding medium of n_a = 1.33. Inset shows near-field profile at the resonance wavelength of 1042 nm. (c) Reflection spectra, and (d) absorption spectra with varying analyte RI from 1.33 to 1.41 [131].

With varying analyte RI from 1.33 to 1.41, the proposed sensor shows a large resonant wavelength shift and exhibits the maximum sensitivity of 350 nm/RIU (Fig. 3.1I). Furthermore, the proposed device also shows near-perfect absorption regardless of the analyte RI variations from 1.33 to 1.41, shown in Fig. 3.1(d). Therefore, it is confirmed that the proposed hybrid metasurface device can work as a sensor as well as a perfect absorber.

Nevertheless, it is important to note that, in plasmonic, dielectric and hybrid metasurface-based sensors, the signal obtained is derived from the measurement of the shift in resonant wavelength when analytes are in close proximity to the metasurface.

Such measurements are performed either via analysis of the transmission/ reflection spectra or via measurement of the change of the intensity of transmission/ reflection at a fixed wavelength at the wing of the resonance. As such, the resonance shift measurements are highly sensitive to the intensity fluctuations and wavelength calibration of the input source, which limits the practical applicability of metasurface sensing outside of a laboratory setting. Therefore, there is a need to develop novel optical sensing techniques that simultaneously provide signal intensification while remaining robust against fluctuations in input source intensity and wavelength performance.

Unlike conventional metasurface-based sensors, diffraction-grating-based sensors can directly measure the ratio of the intensities of two diffraction orders from the grating. This diffraction intensity ratio (DIR = I_{-1}/I_0) is highly dependent on the surrounding environment. Therefore, the proximity of a target analyte to the grating leads to a change in the grating optical response, which is detected by the sensor [152-155]. Due to this ratiometric measurement, such grating-based sensors are robust to the fluctuation of light source intensity and do not require challenging background intensity-calibration of transmission or reflection spectra [131, 147, 149, 156]. To date, several grating-based diffraction sensors have been reported using different configurations such as asymmetric nanofluidic gratings [153], sinusoidal gratings [157], and 1D gratings [152]. However, all of these dielectric metagrating diffraction sensors are based on a non-resonant sensing mechanism that limit the maximization of the DIR and enhancement of the near-field intensity. As a result, they display considerably lower sensitivities than resonant-metasurface sensors. To date, there are no reports of resonant metagrating diffraction-based sensing platforms.

To address the shortcomings of existing dielectric metagrating sensing platforms, we propose and demonstrate a novel sensing platform that combines the advantages of both diffraction-based and resonant metasurface-based sensing. Our platform makes use of a resonant metagrating consisting of a series of dielectric nanostructures, called meta-atoms, where the individual meta-atoms exhibit a Mie-type resonance. Such resonances can scatter the waves in the forward direction while imprinting a phase in the range from 0 to 2π. Therefore, by arranging meta-atoms of different transverse dimensions and having an optimal phase discretisation, one can efficiently manipulate the optical wavefront of the incident light. In particular, one can inscribe a linear phase gradient, mimicking a blazed grating, to deflect the incident light to a single diffraction order. Such

a unique metagrating arrangement [31] enables maximizing the light transmitted into the first diffraction order while minimizing the light in the zeroth diffraction order in a resonant fashion [69, 92, 158, 159]. The detection signal, measured as DIR, can therefore be significantly enhanced, which can, in turn, boost the platform's limit of detection (LOD). In addition, the resonant nature of the meta-atoms of our metagrating can significantly enhance the sensitivity of the metagrating operation to target analytes on its surface. Altogether, these factors intensify the response of our metagrating sensors, granting them exceptional and significantly improved sensitivity, relative to blazed and other grating approaches.

3.2 Diffractive Metagrating Design Concept and Working Principle

Our metagrating consists of a set of nanodisks of different sizes to impose a phase from 0 to 2π on the transmitted light as shown in Fig. 3.2(a). This set of nanodisks forms the unit-cell (red dashed box), which is periodically repeated to form the metagrating. The light transmitted through the metagrating is split into different diffraction orders, where each diffraction order carries a fraction of the power from the incident beam. These fractions are determined by the phase ramp imprinted by the metagrating, which is highly sensitive to its surface refractive index, thus in turn to the presence of analytes on its surface. Since the arrangement of nanodisks mimics a perfect 0 to 2π phase ramp, the incident light is efficiently channelled to a single diffraction order, unlike the other diffraction grating-based sensors, in which the input power is split to multiple diffraction orders [155, 157]. Changes in diffraction profiles due to analytes proximal to the grating can be magnified by simultaneously maximizing the transmission in the -1st diffraction order while minimizing the transmission zeroth order and measuring the ratio of transmittance between orders. The schematic of the DIR data set as a function of RI is shown in Fig. 3.2(b). As both intensities, I_{-1} and I_0 depend on the RI values, the use of the DIR data set intensifies the sensing performance and enables the easy identification of the surrounding RI. This DIR signal is independent of the incident intensity, which is factored out in the ratio of power between the two diffraction orders.

As a result, the metagrating optical sensor is robust to the fluctuations of the input intensity. The diffraction pattern further provides calibration of the incident light wavelength, which is often an issue when a fixed-wavelength laser is used to measure the

sensing response in resonant metasurface sensors. The deflection angle from the metagrating can be calculated using the diffraction equation:

$$n_{tra}\sin\theta_{tra} = n_{inc}\sin\theta_{inc} - m\lambda/d \tag{3.1}$$

where n_{inc} and n_{tra} are the refractive index of the incident and transmission medium, respectively. Θ_{inc} and θ_{tra} are the incident and deflection angles, respectively, λ is the operating wavelength, m is the integer number of the diffraction order, and d is the grating (super-cell) period.

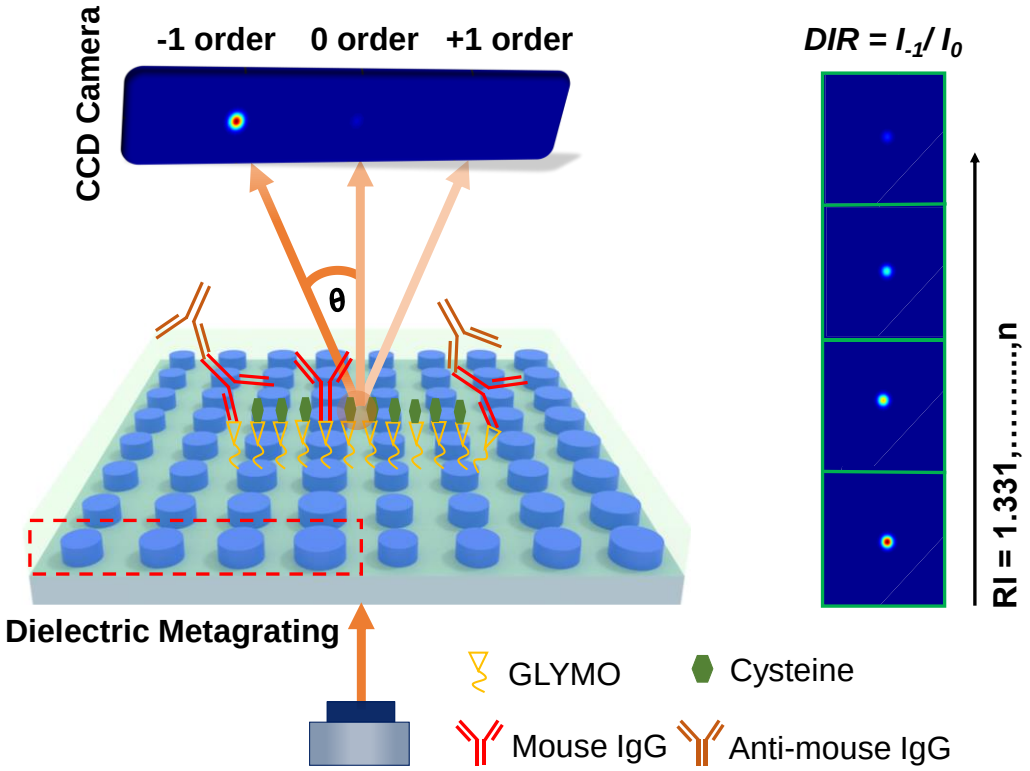

Figure 3.2 (a) Schematic of dielectric diffractive metagrating sensor where the supercell consists of nine nanodisks, and (b) Schematic of DIR data set as a function of RI [74].

The period d is known with high accuracy from the nanofabrication, therefore, the precision measurement of the deflection angle (in the air) from the metagrating provides a good calibration for the laser wavelength. Therefore, the metagrating sensor is also robust to fluctuations of the incident laser wavelength, which can often occur due to temperature or driving laser current fluctuations.

To design our metagrating, we employed nanodisks operating in the Huygens' resonant regime [60]. The Huygens' regime is achieved by spectrally overlapping the ED and MD resonances of the nanodisks, leading to a near-unity transmission along with 0 to 2π phase coverage. This overlap condition is in fact agile to the presence of analytes on the surface of the nanodisks and results in an improved metagrating sensitivity. To optimise the metagrating design, we modelled the metagrating and varied the height and periodicity of the nanodisk for operation in the near-infrared spectral range. This spectral range is advantageous for practical considerations, offering accessible laser sources (laser diodes) and simple detection using CMOS cameras. Our numerical models suggested an optimized nanodisk of 130 nm in height and a period of 500 nm, which enables Huygens' condition for operation in the near-infrared at the wavelength of 850 nm.

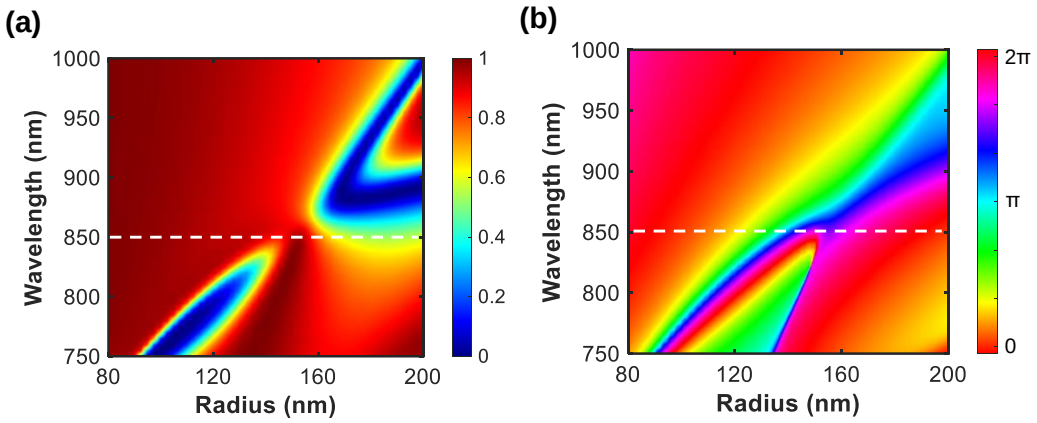

Figure 3.3 Numerically calculated (a) transmission and (b) phase profile for a variation of the nanodisk radius 80 nm to 200 nm with height 130 nm at a constant period of p = 500 nm for silicon-nanodisk metasurfaces embedded in a homogeneous medium with n = 1.331. The white-dashed line indicates the overlap of electric and magnetic resonances at a wavelength of 850 nm [74].

For the metagrating design, we have used a-Si, which is substantially transparent with a high refractive index over this spectral range. We next performed numerical simulations where we varied the nanodisks' radii from 80 to 200 nm. To optimise the individual nanodisk parameters for our metagrating, we use the Matlab-based RCWA to examine the transmission properties of periodic arrays of nanodisks. Such periodic arrays can accurately approximate the local transmission properties of a metagrating composed of gradually varying nanodisks. RCWA has been widely used for investigating the

transmission properties of periodic structures due to its fast convergence and accurate calculations. RCWA is a freely available open-source software package that works in the frequency domain [102, 103]. We have used $\lambda/12$ spatial resolution and up to 7-order Fourier harmonics in both the *x* and *y* directions, which ensures the convergence of the resonant meta-atoms. Figures 3.3(a, b) show the calculated transmittance and the phase accumulation through an array of homogeneous nanodisks, respectively. Notably, at 850 nm, we achieved a transmission window with a near-unity transmission (Fig. 3.3(a)) and 0 to 2π phase profile (Fig. 3.3(b)). We have optimised our metagrating for operation in water as an embedding medium (n = 1.331) to match our sensing experiments.

We have proposed and investigated two metagratings, where one consists of four nanodisks based supercell and the other one consists of nine nanodisks based supercell. Equation 3.1 allows us to calculate the deflection angle for the two metagrating designs. The large deflection angle (LDA) design, having four nanodisks, has periodicity d = 2,000 nm, corresponding to a diffraction angle of 18.6 ° in water (n = 1.331) at 850 nm. When using our experimental setup, the angle is measured in air (n = 1), once the light exits the microfluidic cell used for sensing, resulting in an external deflection angle of 25.2 °. For the small deflection angle (SDA), having nine nanodisks, design with d = 4,500 nm, the corresponding diffraction angle is 8.2 ° in water at 850 nm (or a 10.9 ° external angle in the air). We note that in both cases, the angles are measured at a normal incidence of the input beam (θ_{inc}= 0).

3.3 Metagrating with Large Deflection Angle Based RI Sensing

The optimised LDA metagrating consists of four nanodisks with radii of 126, 138, 147, and 165 nm, as shown in Fig. 3.4(a). These nanodisk sizes provide a phase gradient from 0 to 2π with $\pi/2$ phase increments. To investigate the scattering property of the LDA metagrating, we calculated the transmission spectrum (metagrating embedded in water, n = 1.331) as shown in Fig. 3.4(b). The numerical studies were carried out using CST Microwave studio in the frequency domain. A tetrahedral mesh was used for accurate numerical analysis. The waveguide ports have been used with unit cell boundary conditions to calculate the s-parameters of the LDA metagratings. For our metagrating, the maximum transmission to the -1st diffraction order was calculated to be 42%, while the light transmitted to the 0th order is 2.5%. The remaining power of the incident beam

is distributed into other diffraction orders in forward and backward directions. The observed distribution of the transmitted light to a single diffraction order is highly beneficial for diffractive sensing to maximise the measured signal, which is defined as the ratio between two diffraction orders.

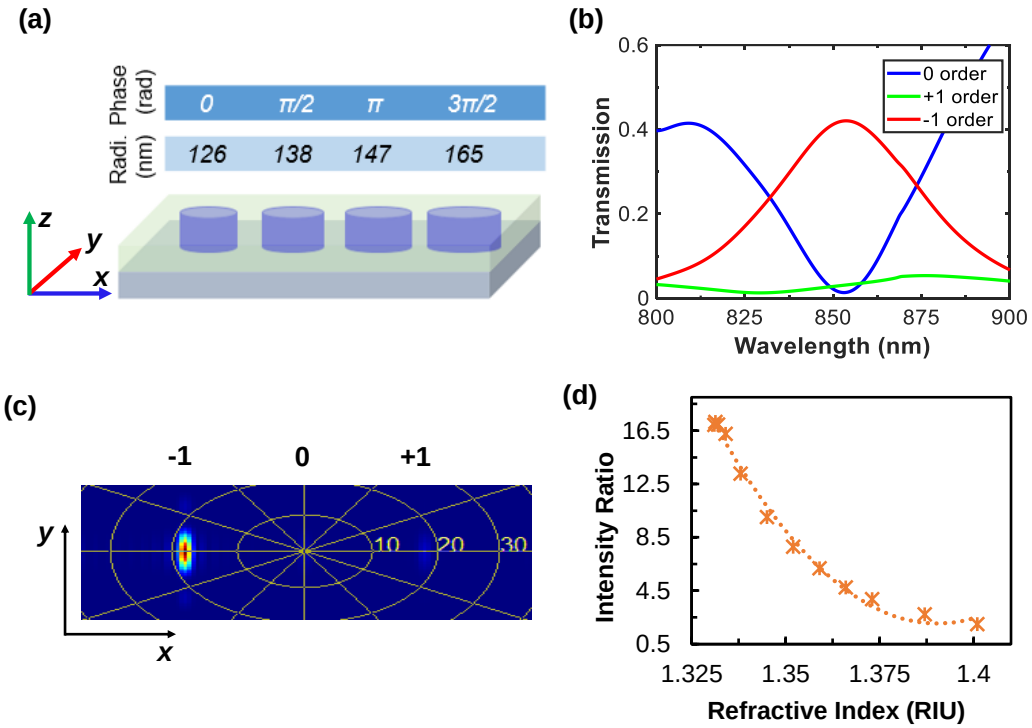

Figure 3.4 (a) Schematic of the smaller supercell which consists of four nanodisks, which is responsible for a phase shift from 0 to 2π with π/2 phase increments. (b) Simulated transmittance spectra for different diffraction orders. (c) The simulated far-field profile obtained by the LDA gradient metasurface resulting in a diffraction angle of 18.6 ° at 850 nm. (d) Sensor response obtained as the diffraction intensity ratio of the -1st and 0th diffraction orders, together with a polynomial fit as a function of the analyte's refractive index [74].

In order to numerically calculate the deflection angle, we investigated the far-field of the LDA metagrating using finite-difference time-domain (FDTD) simulations. A plane wave source was used with periodic boundary conditions in the *x*-*y* axis, and perfectly matched layer (PML) boundary conditions were used in the *z*-axis. The results of our simulations for the *y*-polarisation incident beam are shown in Fig. 3.4(c). The metagrating causes the incident beam to deflect in the *x*-direction to the -1st diffraction order at a deflection angle of 18.6 ° (in water). As can be seen in Fig. 3.4(c), this diffraction order

carries most of the incident light, while the 0^{th} (transmitted) diffraction order only carries a small portion of incident beam power.

To quantify the sensitivity of our diffractive sensor, we define the sensor's signal as, $DIR = I_{-1}/I_0$, where I_{-1} and I_0 refer to the intensities of the -1^{st} and 0^{th} diffraction orders, respectively. Our metagrating minimises I_0 and maximises I_{-1}, thus quadratically maximizing the signal *DIR*. When different analytes are in close proximity to the surface of the gratings, the optimised deflection condition is disturbed, which results in both an increase of I_0 and a decrease of I_{-1}, thus amplifying the observed signal change. The resonant behaviour of the metagrating further enhances its sensitivity to the change of the surrounding environment with a factor proportional to the quality factor of the resonance, which for this grating is $Q \approx 20$ (Fig. 3.4(b)). In contrast, non-resonant grating exhibits a low-Q response, which will lead to minimal sensing performance due to the change of the surrounding medium [160, 161].

To study the effect of the immediate environment on the performance of our diffraction metagrating platform we calculated full transmission spectra with different diffraction orders while varying the surrounding RI from 1.331 to 1.401. The range of the RI is derived from the experimental conditions, corresponding to the change of the RI of a mixture of glycerol and deionised (DI) water [162]. Due to the increase of RI, the 0^{th} and -1^{st} diffraction order transmission spectra exhibit a redshift. As a result, the light transmitted through the 0^{th} diffraction order increases, and the light transmitted through the -1^{st} diffraction order decreases which leads to the downward DIR slope as shown in Fig. 3.4(d). It is also noticeable that at the higher RI values, the difference between two adjacent DIR values is reduced, as a result, the sensor sensitivity is saturated. Furthermore, we have defined the metagrating sensitivity as $S = \Delta s/\Delta n$, where $\Delta s = DIR_1 - DIR_2$ is the change of intensity ratio and Δn is the change of RI. As seen in Fig. 3.3(d), the LDA metagrating shows a maximum sensitivity of 762 RIU^{-1} in the sensing range of 1.331 to 1.401, which is higher than other diffraction sensors [157]. Figure 3.4(d) also shows the 2^{nd} order polynomial fitting within this broad RI variation. The polynomial fitting provides a guide to the eye to the nonlinear data points. In our work, we have used the 2^{nd} order polynomial fitting to show the trend of the response.

To verify our concept experimentally, we fabricated the LDA metagrating by electron beam lithography (EBL) combined with reactive ion etching. The detail of the fabrication process is mentioned in Fig. 2.5. The SEM image of the fabricated LDA

metagrating is shown in Fig. 3.5(a). The red dashed region indicates a single supercell, which consists of four nanodisks. The fabricated sample is integrated into a microfluidic channel for analyte delivery and illuminated at normal incidence to the metagrating. We measured the transmission spectra using a homebuilt transmission setup (see Fig. 2.6(c)) using 5x and 100x objectives to discriminate between the transmission of the 0^{th} and the other diffraction orders. These measurements provided the operating wavelength, ~850 nm, which corresponds to the minimum light transmission at the 0^{th} diffraction order and maximum transmission at the first diffraction order. An image of the microfluidic system integrated with the metagrating is shown in Fig. 3.5(b).

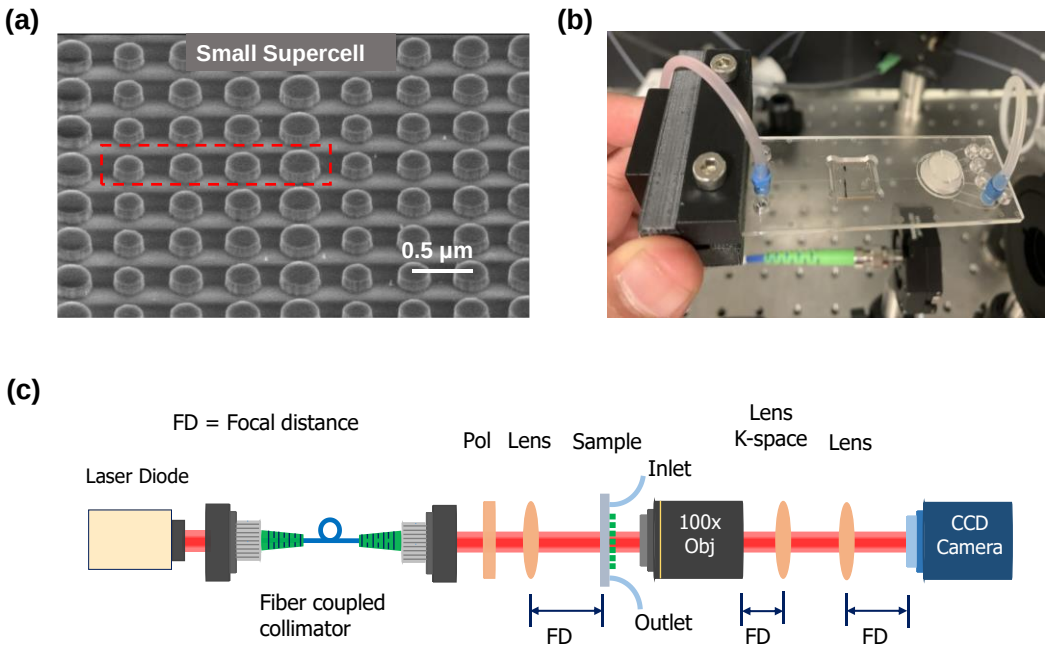

Figure 3.5 (a) SEM image of the tilted fabricated LDA metagrating. (b) Real image of the microfluidic system integrated with LDA metagrating, and (c) experimental setup for the diffraction measurement [74].

The fabricated sample is embedded in a microfluidic chip. Our microfluidics chip supports two input channels, wherein channel 1 is for reference (DI water) and channel 2 is for the analyte of interest. We flow DI water through channel 1 to achieve a base refractive index, and then use channel 2 to induce a change in the refractive index by flowing analyte of interest. I have performed the sensing measurement along with my colleague Shridhar Manjunath.

We have measured the far-field optical properties of the LDA metagrating using the optical setup, shown in Fig. 3.5(c). To perform the diffraction experiment, I have developed the free-space optical setup. I used a laser diode with a power of ~5 mW and a central wavelength of 850 nm. The laser power and laser operating wavelengths (±10 nm) were tuned using the power and temperature controllers, respectively. Fibre-coupled collimators were used to produce parallel beams which lead to the best possible coupling of light into and out of a fibre. A polariser has been used to make the incident beam polarisation according to the measurement requirements. We used a microfluidic channel to continuously flow glycerol at a range of concentrations from 0.5% to 50% v/v and maintained the flow rate at 15 µL/min with a maximum pressure of 15 psi.

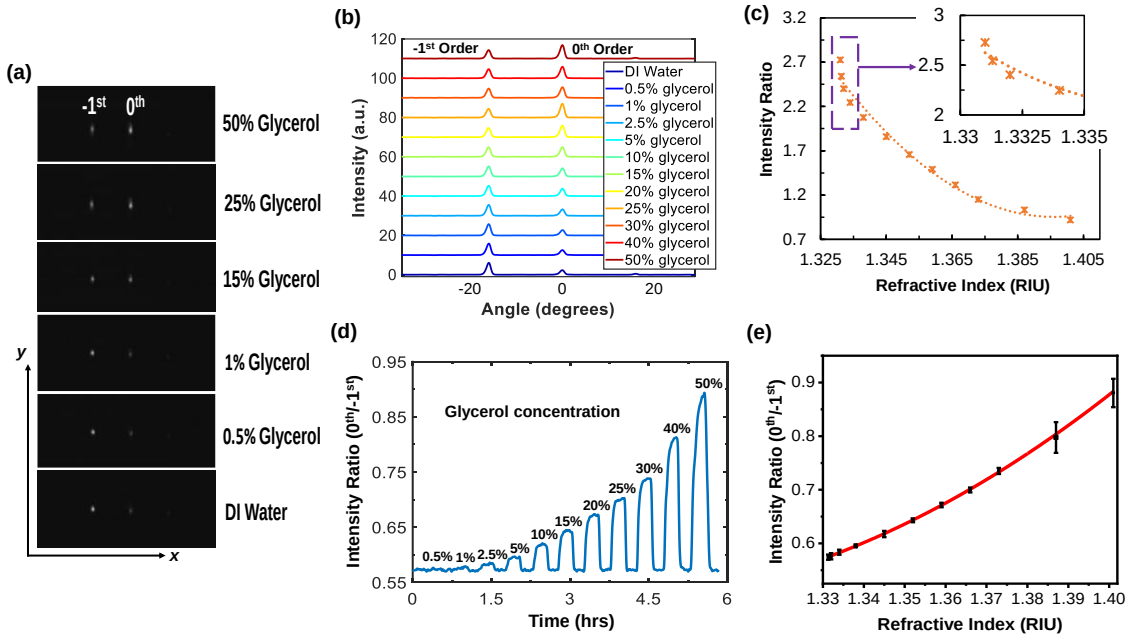

Figure 3.6 Experimental large deflection angle results. (a) Far-field profiles of the incident light with varying glycerol concentrations. (b) The line scan of diffraction intensity with varying the glycerol concentration in water up to 50% (v/v). (c) DIR signal measurement and the corresponding polynomial fitting as a function of RI of the glycerol-water mixture. Inset shows a magnified scale for the sensitivity estimation. (d) Real-time DIR response to the variation of glycerol concentration, and (e) 2nd order polynomial fitting of intensity ratio as a function of the analyte RI [74].

The 100x objective was used to collect all the transmitted light passing through the sample. A lens has been placed in a focal distance of the objective which helps to establish

a k-space measurement environment. Another additional lens is placed at a focal distance of the CCD camera to image the back focal plane in real space. The real and k-space measurement has been carried out by altering (keeping and removing) the k-space lens. In the end, a CCD camera was placed at a focal distance from the real-space measuring lens to capture the far-field images.

To perform the RI measurement, a series of glycerol (Univar AJA242) solutions were prepared from 50% (v/v) to 0.5% (v/v) by serially diluting in 18 MΩ.cm DI water with refractive index spanning a range of 1.401 to 1.3313. As can be seen in the experimentally measured far-field profiles (Fig. 3.6(a)), with the rise in glycerol concentration and therefore RI [149], the light transmission through the 0^{th} and -1^{st} diffraction orders increases and decreases, respectively. As further proof, we analysed the line scans of the far-field profiles, shown in Fig. 3.6(b). In the line scan analysis, we integrated the intensity over 30 vertical pixels covering each of the individual diffraction orders to enhance the calculation accuracy and average them, accordingly, confirming the observed changes in transmittance to the 0^{th} and -1^{st} diffraction orders. To probe the limit of detection, we gradually reduced the concentration of glycerol and experimentally demonstrated that our sensor can detect as low as 0.5% (v/v) concentration of glycerol solution in water. Subsequently, by quantifying the diffraction intensity ratio of the -1^{st} to 0^{th} diffraction orders, we have shown the correlation between the DIR and RI in Fig. 3.6(c). This result shows that the experimental sensitivity of the proposed sensor is 616 RIU^{-1}, which is 19% lower than the numerically calculated value, presented in Fig. 3.4(d), i.e. 762 RIU^{-1}. This difference might be due to several factors, including fabrication imperfections, impurities of the water medium, arbitrary scatterings of the uneven surface of the microfluidic channel, etc. Nevertheless, this sensitivity exhibits a 2^{nd} order polynomial trend.

We next performed RI measurements using a real-time monitoring system, flowing glycerol at set concentrations for 15 minutes at a flow rate of 15 µL/min and captured the signal every 15 seconds. Between each successive glycerol concentration, DI water was flown at the same flow rate to wash the microfluidic channel and remove residual glycerol. The subsequent results for successive flow cycles, shown here as the intensity ratio between the 0^{th} and -1^{st} diffraction orders at glycerol concentrations from 0.5% to 50% are shown in Fig. 3.6(d) (for better slope representation). Notably, our metagrating sensor exhibits a stable response over successive exposures to glycerol and washes, with the response returning to the same baseline during each wash. In addition, the correlation

between the intensity ratio and refractive index is shown in Fig. 3.6(e), further validating the above results.

As our resonant metagrating sensor is based on maximizing the light at a certain diffraction order, this approach theoretically allows for further sensitivity optimization by controlling the deflection angle. In particular, earlier studies have revealed that by increasing the deflection angle, the transmission efficiency decreases, and subsequently, the diffraction efficiency diminishes significantly [69, 163]. Accordingly, we next investigated a metagrating sensor with a small deflection angle.

3.4 Metagrating with Small Deflection Angle Based RI Sensing

Our SDA metagrating consists of nine a-Si nanodisks with radii of 126 to 200 nm as determined from the 2D transmission and phase responses shown in Figs. 3.3(a, b). The polar plot of the transmitted phase and transmission efficiency of chosen nanodisks is shown in Fig. 3.7(a). The transmission efficiency of individual disks is close to unity, and the disks can efficiently cover the 0-2π phase range with small-discretised values of 2π/9.

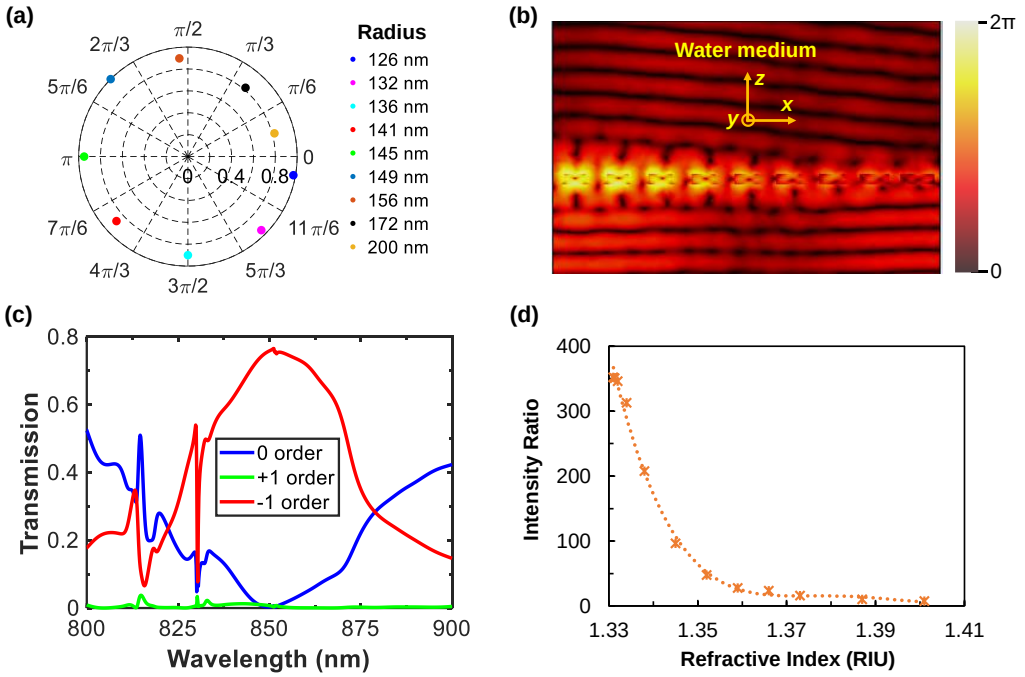

Figure 3.7 Simulated SDA metagrating results. (a) Transmittance and phase in polar format at the operating wavelength of 850 nm. (b) Simulated phase profile obtained by the metasurface resulting in a diffraction angle of 8.2 ° at 850 nm wavelength. (c) Simulated transmittance spectra for different diffraction orders, and (f) polynomial fitting of DIR signal as a function of the analyte RI [74].

As a result, the coupling between nanodisks is more stable, which leads to beam deflection with higher efficiency. This higher efficiency indicates that the sensor response can be significantly enhanced with the use of an SDA metagrating. The simulated phase profile of the propagating waves through our SDA metagrating is shown in Fig. 3.7(b) at the operating wavelength of 850 nm. The calculated deflection angle in the water environment surrounding the silicon metagrating is 8.2 degrees. The transmission spectra of different diffraction orders are shown in Fig. 3.7(c). The SDA metagrating is able to transmit a maximum of 77% of incident light at the -1st diffraction order, which is nearly twice the transmission compared to the LDA metagrating while transmitting only 0.22% of incident light in the 0th diffraction order.

As with the LDA metagrating, when the analyte RI increases, the light transmitted to the -1st diffraction order decreases, while the light transmitted to the 0th order increases (Fig. 3.7(d)). The 4th order polynomial fit is used where the quadratic part is dominant. The calculated maximum sensitivity of the SDA metagrating is therefore measured to be as high as 26,266 RIU^{-1} within the sensing range of 1.331 to 1.401. This sensitivity represents a 35-fold higher sensing response in comparison to the LDA sensor and a considerable increase over previously reported diffractive sensors, as shown in Table 3.1.

Table 3.1. Performance comparisons of the reported dielectric diffraction sensors.

Characteristics	Operating wavelength (nm)	Sen. Process		RI range	Sens. (RIU^{-1})	LOD	Ref.
		Bulk	Surface				
Porous silicon 1D grating	632	×	√	NA	NA	41.7 nM	[152]
Asymmetric optofluidic grating	635	√	√	1.334-1.373	2.416	NA	[153]
Asymmetric Fraunhofer diffraction	532	√	×	1.33416-1.33406	11,000	NA	[155]
Sinusoidal relief grating	632	√	×	1.36-1.59	-557	NA	[157]
Diffractive metagrating	850	√	√	1.331-1.401	26,266	~770 fM	This work [74]

We also compared our sensor's response with a conventional blazed grating that we designed using the same a-Si material and deflection angle as the SDA metagrating. Notably, our SDA metagrating exhibits a six-fold higher sensing response compared to the conventional blazed grating.

We next experimentally confirmed the simulated sensitivity enhancement presented by the SDA resonant metagrating. An SEM of the fabricated SDA metagrating is shown in Fig. 3.8(a), where the red dashed area indicates a single supercell consisting of nine nanodisks. The experimental transmission spectra of different diffraction orders are shown in Fig. 3.8(b). The measured 0^{th} diffraction order exhibited only 6% transmission, while the other (first plus higher) diffraction orders exhibited transmission of 50%. Although the simulated transmission spectra (-1^{st} order) have a sharp dip at around 830 nm however, this is not visible in the measured transmission spectra mainly due to the lower resolution of the spectrometer. However, this particular sharp dip does not influence our results which are based on broader Mie-resonant features.

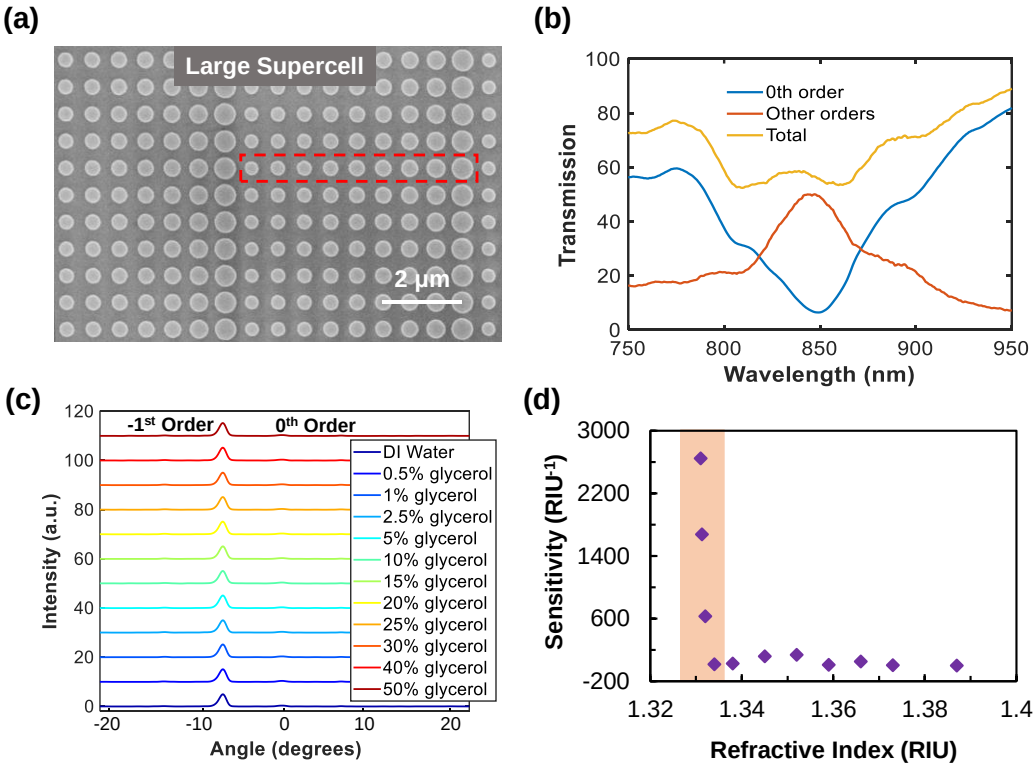

Figure 3.8 Experimental SDA metagrating results. (a) SEM image of the fabricated SDA metagrating. (b) Experimental transmission results of different diffraction orders. (c) The line scan of diffraction intensity with varying the glycerol concentration in water up to 50% (v/v), and (d) sensitivity response as a function of RI [74].

Later, we performed the RI measurement using the same continuous flow microfluidic system and assay protocol mentioned above. The diffraction intensity in the different diffraction orders with the variation of glycerol concentration is shown in Fig. 3.8I. When the glycerol concentration is increased, light transmitting through the 0^{th} diffraction order is increased, albeit to a lesser extent than with the LDA metagrating. Nonetheless, the intensity ratio of SDA metagrating is four times higher than the LDA metagrating. This leads to a significantly improved sensing response with a maximum sensitivity of 2,645 RIU^{-1} (Fig. 3.8(d)), which is higher than that reported for other diffraction-based sensing approaches [153, 157]. To realise the effect of fabrication imperfections, we have investigated the response in the ideal simulation case as well as with a 50% variation from the ideal simulation case. To reflect such imperfections, we have increased the transmitted light to the 0^{th} diffraction order and reduced transmitted light to the -1^{st} diffraction order by 50%, correspondingly. By considering this deviation from the ideal case, our calculated maximum sensitivity becomes 4,210 RIU^{-1}, which is comparable to the experimentally measured sensitivity. Notably, as the glycerol concentration further increases, the SDA metagrating response sharply drops (Fig. 3.8(d), outside of the shaded region). This is a characteristic of the optimization process undertaken to enhance the sensor's response at a target refractive index. The proposed metagrating is optimised for DI water medium (ideal case) where the maximum light diffracted in the -1^{st} diffraction order and minimum light diffracted in the 0^{th} diffraction order. With the increase of refractive index, the ideal condition is void, such as, light diffraction in the -1^{st} order starts decreasing and the 0^{th} order starts increasing. In this design, the SDA metagrating displays its highest sensitivity at low refractive indices reflecting its use in aqueous systems. Although we have here characterised the sensor over a broad range of RI's, in practical applications, such as in biosensing, the observed RI changes tend to be small in comparison due to low analyte concentrations. These small RI changes have previously proven challenging to detect with less sensitive platforms [135]. However, the acute sensitivity of our platform at aqueous RI's makes it suitable for the detection of analytes at these low concentrations, which is a desirable application of optical sensors.

We have further investigated the oblique incidence effect on the LDA and SDA metagratings, shown in Fig. 3.9. With the increase of incident angle, the light transmission in different diffraction orders for LDA metagrating changes rapidly compared to the SDA

metagrating. In LDA metagrating, at normal incidence, the maximum light is transmitting at the -1st diffraction order. However, at 6 degrees incident angle, most of the light starts to transmit at the 0th diffraction order (Fig. 3.9(a)). On the other hand, with the increase of incidence angle, the light transmitted in the 0th diffraction order is slightly increased in SDA metagrating (Fig. 3.9(b)). However, while the oblique incidence is 12 degrees the light transmitting through the 0th and -1st diffraction order is almost equal. Based on these responses, we concluded that the SDA metagrating response is more stable for the oblique incidence compared to the LDA metagrating.

Therefore, to exemplify such unique biosensing capability in the final part of our work we investigated the SDA metagrating as a compact biosensor of IgG antibodies.

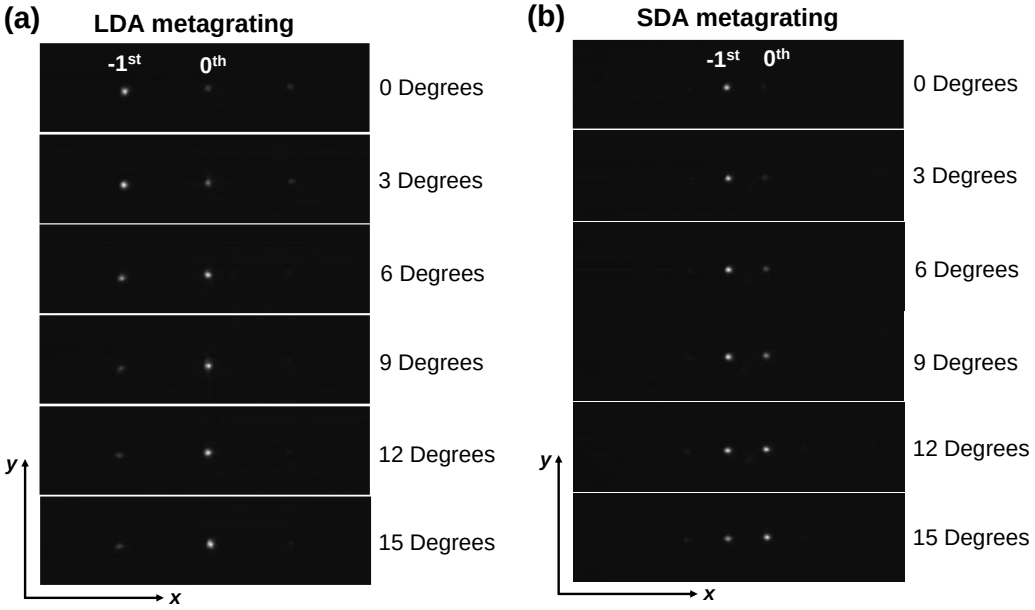

Figure 3.9 Experimentally measured oblique incidence effect on (a) large deflection angle metagrating, and (b) small deflection angle metagrating while varying the oblique incidence from 0 to 15 degrees [74].

3.5 Metagrating with Small Deflection Angle Based Biosensing

The high sensitivity of the SDA metagrating response to refractive index changes seen above indicates that the resonant metagratings are well suited for biosensing applications. In such applications, the capture of a biomolecule at the sensor surface induces a change in the local refractive index relative to that of the bulk solution. Therefore, while the

sensing principle remains the same as above, biosensing, in addition, requires the selective capture and detection of the target biomolecule from an often complex medium. To validate our SDA metagrating sensors for biosensing applications, we next verified its capacity to detect the binding of anti-Mouse IgG antibodies, which are commonly used detection antibodies for biosensor benchmarking trials and for signal enhancement in 64 immune-sensors. The resulting antibody binding measurements should therefore provide a metric for both our sensors' capacity to detect the binding of a detection antibody to its target as well as their sensitivity to the capture of moderately sized biomolecules by surface-immobilised antibodies.

Before proceeding to the experimental biosensing characterizations, we will discuss the surface functionalization and antibody immobilization process, as well as antibody binding assay in secs 3.5.1 and 3.5.2. My colleagues Shridhar Manjunath and Buddini Karawdeniya developed the surface functionalization process. I along with Shridhar Manjunath finally performed the diffraction measurement for the different concentrations of the anti-mouse IgG.

3.5.1 Surface Functionalization and Antibody Immobilization

Functionalization involves 3 main steps: surface salinization, immobilization of the capture antibody, and blocking of any unreacted epoxide groups to prevent undesirable non-specific protein attachment (Fig. 3.10(a)). Prior to functionalization, the substrate was cleaned by sonication in acetone and isopropanol followed by drying under nitrogen. The substrate was then treated with oxygen plasma (1 min at 120 W power) to enrich the surface with hydroxyl groups, followed by submerging in 1% v/v 3-Glycidyloxypropyl-trimethoxysilane (GLYMO) in anhydrous toluene for 2 hours. To remove unbound GLYMO and obtain a uniform silane layer, the substrate was sonicated in anhydrous toluene for 30 s followed by baking for 30 minutes at 110^{o} C. To immobilise the Mouse IgG, 100 µL of 80 µg/mL antibody solution in 10 mM sodium phosphate buffer (pH 9.5) was added to the substrate and incubated for 2 hours at room temperature followed by a thorough wash using DI water. Subsequently, the sample is incubated in a 10 mM cysteine solution in 10 mM sodium phosphate buffer (pH 9.5) for 15 minutes to destroy or block any unreacted epoxide groups. This incubation was followed by another DI water wash and drying under a nitrogen stream.

3.5.2 Antibody Binding Assay

The anti-Mouse IgG was diluted to the working concentrations (50 µg/mL, 5 µg/mL, 0.5 µg/mL, 50 ng/mL, 10 ng/mL, 5 ng/mL, 1 ng/mL, 0.5 ng/mL, 50 pg/mL, 5pg/mL, 0.5 pg/mL) using 10 mM sodium phosphate buffer (pH 7.4). Working samples were added to the substrate and incubated for 15 minutes at room temperature. Following incubation, the sample was rinsed thoroughly with DI water and dried under a nitrogen stream to remove unbound anti-Mouse IgG. The effect of nonspecific binding and the presence of contaminants in the test sample were also investigated. For further details please refer to Fig. 3.11. Optical measurements were carried out in the dry state as three independent trials of at least five replicate measurements each. Due to the dry state environment, the resonant wavelength undergoes a hypochromic shift from 850 nm to 820 nm. We, therefore, performed biosensing measurements at a wavelength of 820 nm.

3.5.3 Biosensing and Detection Limit Measurements

To simulate a stable test system, we immobilised a primary antibody (Mouse IgG) onto the dielectric metagrating using silicon to amine/sulfhydryl coupling strategy (Sec. 3.5.1, Fig. 3.10(a)). After confirming stable Mouse IgG immobilization (Fig. 3.10(b)), we performed an anti-Mouse IgG binding assay by measuring the diffraction intensity ratio between the 0^{th} and -1^{st} diffraction orders at a range of analyte concentrations from 5×10^{-10} to 5×10^{-3} mg/mL (3.1 fM to 312 nM), shown in Fig. 3.10(c). The resulting sensor response was fitted with the four-parameter logistic fit, shown with a red curve in Fig. 3.10(c).

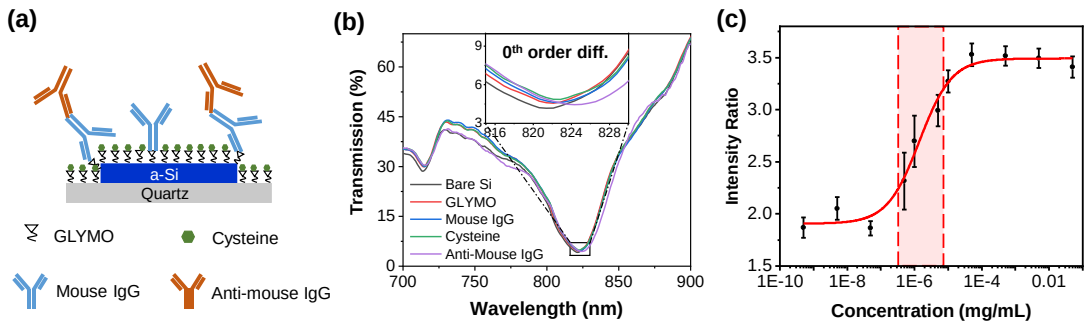

Figure 3.10 (a) Schematic illustration of surface functionalization for selective biosensing of anti-Mouse IgG. (b) Experimentally measured transmission for the zeroth-

order diffraction during the different binding steps. (c) A plot of the average intensity ratio *vs.* anti-Mouse IgG concentration in the range of 5×10^{-10} to 5×10^{-2} mg/mL (3.1 fM to 312 nM). Each point is an average of three trials with error bars representing the standard deviation. The red curve represents a four-parameter logistic fit with the shaded area showing a detection range from 3×10^{-7} mg/mL to 6.5×10^{-6} mg/mL (IC_{20} to IC_{80}) [74].

From the fitted model, the assay's LOD (IC_{10}) was calculated to be 123 pg/mL (~770 fM) with a detection range (calculated as IC_{20} to IC_{80}) of 3×10^{-7} mg/mL to 6.5×10^{-6} mg/mL and a dynamic range of roughly 80%. Notably, these results are comparable to the reported affinities of tight-binding antibodies [164], suggesting that our sensing platform can be used to transduce most immunoassays.

It is therefore also likely that the measured LOD is bounded by antibody binding affinity rather than by platform sensitivity. Additionally, we demonstrate that the sensor does not show significant non-specific binding and it is sufficiently selective to the target antibody in the presence of off-target antibodies, showing potential for sensing of biological samples (Fig. 3.11). It is important to note that our sensing concept is based on the intensity ratio of the zeroth and the first order peaks, and not on the individual intensity of each peak. As a result, while the resonance shift may appear small (approximately 0.75 nm, Fig. 3.11), the sensing response in the form of intensity ratio is inherently magnified and changes by approximately a factor of two (Fig. 3.10I). This amplification of the signal is one of the major benefits of the resonant sensing concept, introduced here. The reproducibility of the sensor response is shown in Fig. 3.10I. In addition, while many biomolecular targets of interest are smaller than antibodies, the dynamic range observed for antibody binding suggests that the binding of smaller biomolecules could still be accurately detected, especially if detection antibodies are used to enhance the signal obtained. As such, these results demonstrate that SDA metagratings are suitable for use in optical biosensing.

3.5.4 Nonspecific Binding and Signal Contamination Analysis

We have tested the level of nonspecific antibody binding to the cysteine-blocked GLYMO-treated surface using 50 μg/mL anti-mouse IgG target without prior immobilization of the mouse-IgG bioreceptor. No detectable signal change was observed in these conditions, as shown by Fig. 3.11(a), indicating that there is no significant

nonspecific antibody binding occurring. To test the platform selectivity, we further performed a second test of the fully functionalised sensor, including immobilization of the mouse-IgG bioreceptor, then added 50 μg/mL of an arbitrary off-target (anti-NFL) antibody in PBS buffer at pH 7.4 instead of anti-mouse IgG. Again, no detectable response to the off-target analyte has been observed, as shown by Fig. 3.11(c).

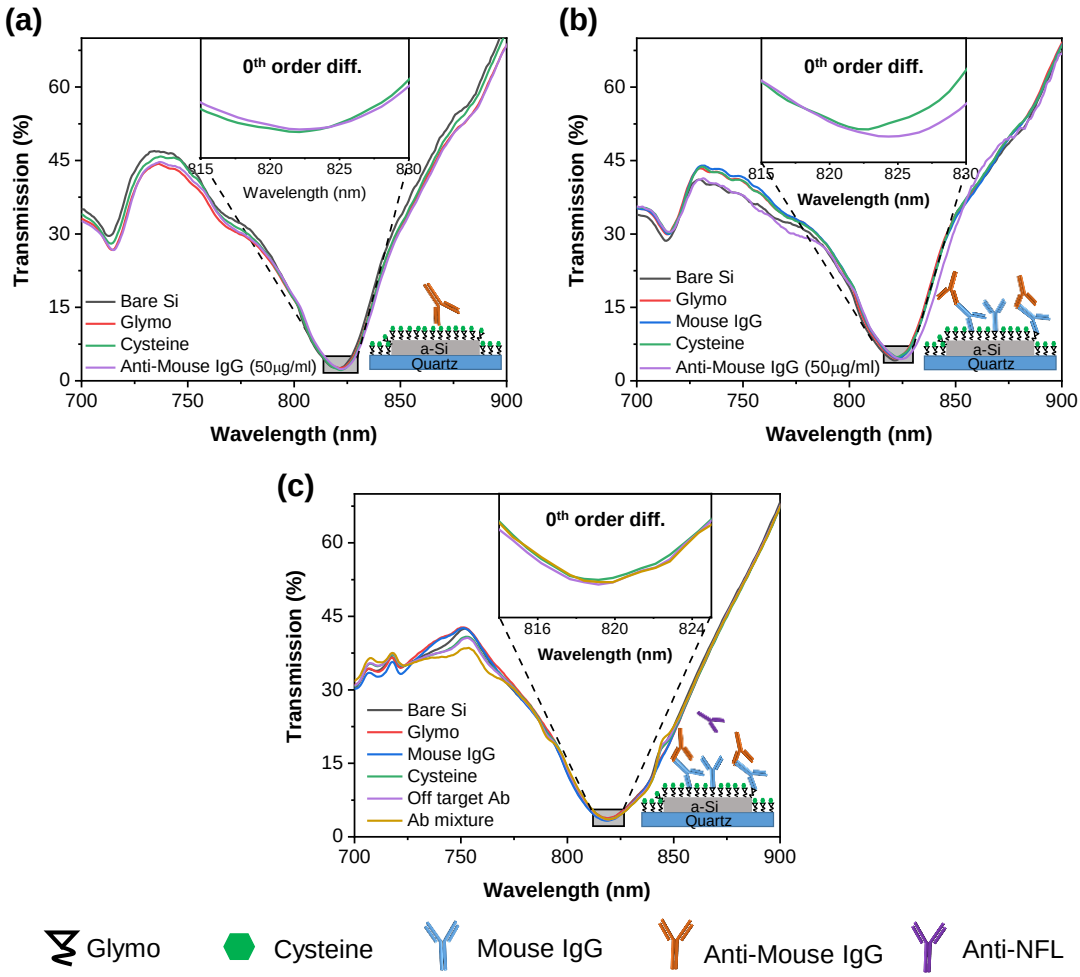

Figure 3.11 (a) Measured transmission spectra without the mouse IgG receptor to observe any non-specific binding of the anti-mouse IgG (50 μg/mL) to the cysteine that showed no shift indicating the absence of any significant non-specific binding. (b) Measured transmission spectra from the original experiment with 1.48 nm shift observed for 50 μg/mL anti-mouse IgG, and (c) Measured transmission spectra of 50 μg/mL off-target antibody (anti-Neuro filament or anti-NFL) with no detectable response and a mixture of 1:1 anti-NFL and anti-mouse IgG (25 μg/mL final concentration each) with a 0.75 nm shift demonstrating the selectivity of the platform [74].

When a 1:1 (v/v) mixture of the off-target antibody and the anti-mouse antibody (25 μg/mL final concentration each) in PBS buffer at pH 7.4 was added to the functionalised sensor, a shift of 0.75 nm in the resonance peak was observed (for 50 μg/mL anti-mouse a shift of 1.48 nm was observed in Fig. 3.10 and Fig. 3.11(b)), as shown by Fig. 3.11(c), demonstrating the high selectivity of our metagrating sensor. The resonance shift of the proposed sensor is comparable with the previously reported works [136-138]. However, our proposed sensors are functioning based on the intensity, and its intensified response demonstrates changes by a factor of two (Fig. 3.10(c)). The sensitivity enhancement is a consequence of the proposed novel sensing concept using a metagrating and cannot be achieved by a regular metasurface.

3.6 Summary

In this chapter, I first demonstrated a hybrid metasurface-based optical sensor exhibiting a highly sensitive response (average sensitivity, 325 nm/RIU). This hybrid platform also allows to utilisation of the absorption phenomena. Therefore, my proposed hybrid-metadevice can work as a near-perfect absorber as well as a sensor, simultaneously. Subsequently, we designed and experimentally validated a novel label-free optical sensing platform that uses resonant dielectric metagratings. These metagratings can transduce changes in local RI caused by the presence of an analyte of interest into an optical signal with extremely high sensitivity in comparison to existing optical sensing platforms while remaining insensitive to fluctuations in the input light source. Here, two metagrating designs were investigated that exhibit different deflection angles and found that large deflection angle and small deflection angle metagratings show maximum sensitivities of 752 and 26,266 RIU^{-1}, respectively, in the RI range of 1.331 to 1.401, which is equivalent to a glycerol concentration of 0.5% to 50% in water. These sensors have also been shown to be capable of detecting a change in RI as small as 0.0003 (0.5% (v/v) glycerol). To further demonstrate the suitability of our metagrating sensors to real-world optical sensing applications, the small deflection angle metagrating sensor's capacity was verified to detect biomolecular binding events using a Mouse-IgG/ anti-Mouse IgG system. To our knowledge, the small deflection angle metagrating sensor exhibited the smallest anti-Mouse IgG limit of detection yet reported of ~770 fM. In addition, they function at a single wavelength, using a ratiometric analysis rather than a time-consuming full-spectrum analysis, thus greatly simplifying their use beyond the lab

bench. These results altogether demonstrate that our sensor concept presents a robust platform with significant signal amplification at low analyte concentrations, making it particularly suitable for label-free biosensing applications. Given the wide range of bioreceptors and other capture technologies that could be readily adapted for use with our platforms, this metagrating sensing platform provides a new avenue for the creation of on-demand response intensified optical sensors.

Chapter 4

Dielectric Metasurface Based Edge Detection

The material in this chapter was in part presented in [165].

In this chapter, I will present another advanced functionality of optical metasurfaces namely performing image processing. This functionality is based on Mie-type resonant dielectric metasurfaces which can perform the edge detection of an image. First, I will discuss the design concept of the dielectric metasurfaces. Subsequently, I will demonstrate the angular dispersion analysis and perform the numerical edge detection. Finally, I will demonstrate the experimental results of the optical edge detection including polarisation dependency and resolution of the edge detection.

4.1 Introduction

Analog spatial differentiator is an important optical computational device that can be potentially used in the field of high-speed edge detection and optical image processing [32, 166]. Edge detection is one of the image processing techniques, which helps to decrease dramatically the complexity of an image, keeping the information about the shape and the position of objects. Edge detection enhances silhouettes of the objects in the image by eliminating light everywhere else. Edge detection can be implemented numerically by filtering low frequencies in Fourier space or using Kernel convolution technique. However, for applications, where the speed of processing or the power consumption are critical, passive edge detection, without any additional post-computation, is crucial. One of such passive edge detection methods is a 4-*f* optical system with Fourier-plane filtering. The conventional 4-*f* systems are bulky, and limit their broad range of applications. To overcome these issues a passive direct k-space filtering is required, which can directly perform image differentiation without any need of Fourier transform.

Generally, Fourier filtering of sharp edges with inverse-Gaussian shape transmittance results in the edge detection effect. If the edges of a target image are not very sharp, which means its intensity function is smooth. By using the second derivative of the initial function, it is possible to predict the intensity function. It can be proven that

this concept mathematically in one dimension. For two dimensions, it is required to consider the second coordinate, however, the concept will be similar. Our filter is an inverse-Gaussian function in Fourier space, therefore it can be expressed as:

$$g(k) = 1 - e^{-\frac{k^2}{c^2}}. \tag{4.1}$$

where *k* refers to the space coordinate in Fourier space for one dimensional case, and *c* is a constant.

Let's assume, our initial image function is $f_{\text{im}}(x)$ and the resulted edge detection function is $f_{\text{ed}}(x)$. Now, the Fourier transform of the image intensity can be written as:

$$F_{im}(k) = \mathcal{F}\{f_{im}(x)\}. \tag{4.2}$$

To apply the inverse-Gaussian filter in Fourier space, we need to multiply the filter function *g(k)* with the Fourier transform of the image function $F_{im}(k)$.

$$g(k) \cdot F_{im}(k) = \left(1 - e^{-\frac{k^2}{c^2}}\right) \cdot \mathcal{F}\{f_{im}(x)\}.$$

For simplicity, we consider $c = 1$, so it can be express as:

$$g(k) \cdot F_{im}(k) = \left(1 - e^{-k^2}\right) \cdot F_{im}(k). \tag{4.3}$$

If the *k* value is small, then the Taylor series of the filter function can be expressed as:

$$g(k) = 1 - e^{-k^2} = k^2 - \frac{k^4}{2!} + \frac{k^6}{3!} - \frac{k^8}{4!} + \cdots \approx k^2. \tag{4.4}$$

The Fourier transform of a second derivative of a function is equivalent to multiplying the Fourier transform of the function itself to the square of the frequency

$$\mathcal{F}\left\{\frac{d^2 f_{im}(x)}{dx^2}\right\} \triangleq k^2 \cdot F_{im}(k). \tag{4.5}$$

Finally, the filter image will be achieved by doing the inverse Fourier transform of the multiplication of the Taylor expansion eq. 4.4, and Fourier transform of the image function eq. 4.2. Therefore, resulted edge detection can be express as:

$$f_{ed}(x) = \mathcal{F}^{-1}\left\{k^2 \cdot F_{im}(k)\right\} = \frac{d^2 f_{im}(x)}{dx^2}. \tag{4.6}$$

From eq. 4.6, we can say that the Fourier filtering with inverse-Gaussian shaped filter is exactly equal to the second derivative of the initial function.

To date, a very few optical image differentiators have been reported, which can directly perform the edge detection. The reported optical image differentiators can be categorised based on their materials, and device architectures, such as plasmonic planar structure [167, 168], dielectric 1D grating [169, 170], and dielectric 2D metasurfaces [13, 38, 171, 172]. In 2017, Zhu *et al.* experimentally reported a prism-based angle sensitive plasmonic differentiator, which was able to perform as a spatial frequency filter to detect the edge of an object by changing the phase and amplitude distribution of the incident beam [167]. More recently, multi-layered plasmonic differentiator has been experimentally demonstrated to enhance the edges of the target image, as well as to perform the phase gradient detection [168]. The reported plasmonic image differentiators are operating in reflection mode, which facilitates large phase span due to Fabry-Perot channel. However, it limits broad range of applications, as it is not directly compatible with standard image processing/ recognition systems [173, 174]. Additionally, plasmonic materials exhibit high intrinsic loss, and limited to extend the other frequency bands due to inherent resonance response of material properties [32]. To avoid these plasmonic material issues, dielectric materials has been utilised and performed the edge detection operation [169, 171, 173]. Recently, Cordaro *et al.* has experimentally realised all-dielectric metasurface based 1D grating approach to perform the 1^{st} and 2^{nd} order spatial differentiations, shown in Fig. 4.1 [169].

However, the reported grating-based approach is limited to polarisation dependency which could restrict their general applications. Very recently, all-dielectric 2D metasurface (silicon nanopillar) based image differentiation has been reported by Zhu *et al.*, which exhibits the 2^{nd} derivative operation in broadband range [13]. However, this work also exhibits polarisation dependency, where the s-polarisation incident exhibits invariant minimal transmission response as a function of incident angle, therefore, only p-polarised incident able to perform the edge detection. In this case also, polarisation dependency will limit the applications. Therefore, it is importance to understand the spatial dispersion of metasurface resonances of a different nature and achieve polarisation-independent spatial filtering to enable practical applications in vision technologies.

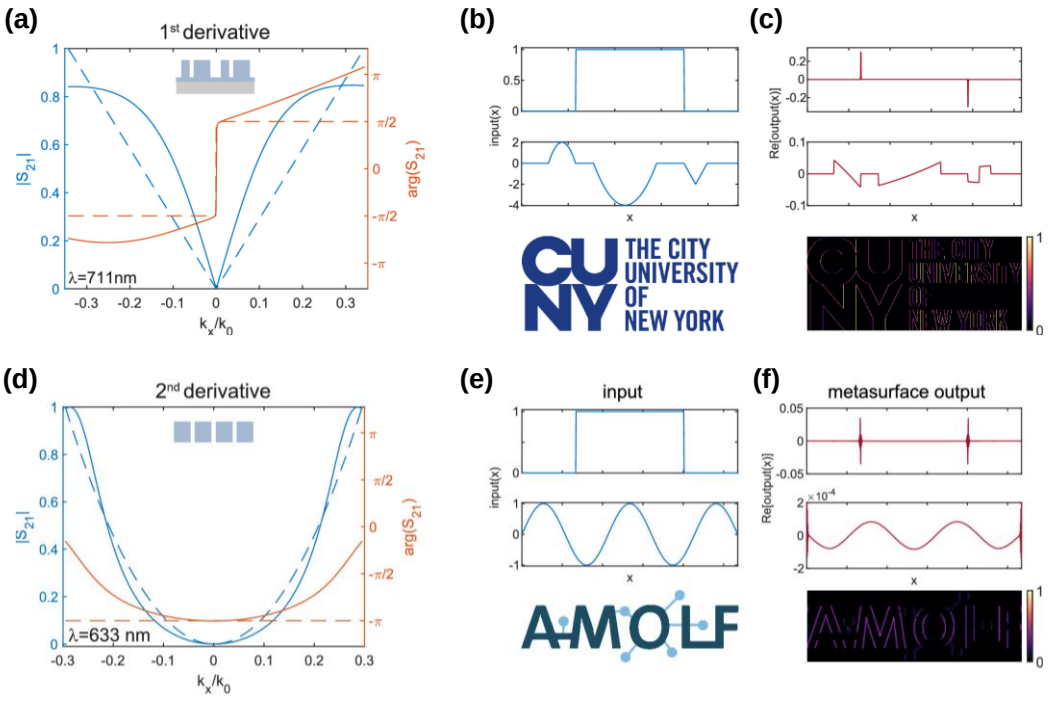

Figure 4.1 Simulated transfer functions of dielectric metasurfaces performing first- and second-order spatial differentiation. (a) Transmission amplitude |S21| (solid blue line) and phase arg(S21) (solid orange line) for the metasurface optimised for first-derivative operation (sketched in the inset) at λ = 711 nm. The simulated transfer function is compared to the ideal case (dashed lines). At the normal incident, the phase shows a π jump. (b) Rectangular and sinusoidal input functions and 2D image that are used to numerically test the metasurface operation. (c) Metasurface output for the input in part b. For the 2D image, differentiation is performed line by line along the x-axis. (d-f) Same as parts a-c but for second-derivative operation (metasurface geometry sketched in the inset) compared to the ideal case (dashed lines) at λ = 633 nm. The transmission reference plane is set such that the transmission phase at normal incidence is 0 [169].

In this chapter, Mie resonance caused by dipole distribution of the electromagnetic field inside the silicon nanodisks based edge detection has been demonstrated (see sec 1.3.2 for details). The edge detection process has been investigated both for the electric and magnetic dipole resonances and compared their effectiveness for edge detection. Finally, it was experimentally proved that magnetic type resonance provides edge detection response with higher efficiency. Mie type dipole resonances can be excited by the completely angularly symmetrical nanoparticles, for example, disks, that we used in

our experiments. It makes our edge detection effect polarisation insensitive, which is experimentally demonstrated in this work.

4.2 Metasurface Design

The proposed metasurface is composed of a-Si based nanodisks, which are arranged in hexagonal unit-cell, shown in Fig. 4.2. The hexagonal nanodisk arrangement provides the metasurface symmetry and helps to achieve more homogenous angular dispersion profile. I have used the CST microwave studio with unit-cell boundary condition to optimise the nanodisk parameters. I have optimised the nanodisk parameters where the disk radius (*r*) of 330 nm, height (*h*) 200 nm, and periodicity (*p*) 1000 nm. I have used the experimentally measured a-Si refractive index data and considered the glass substrate refractive index of 1.50 during the computational analysis.

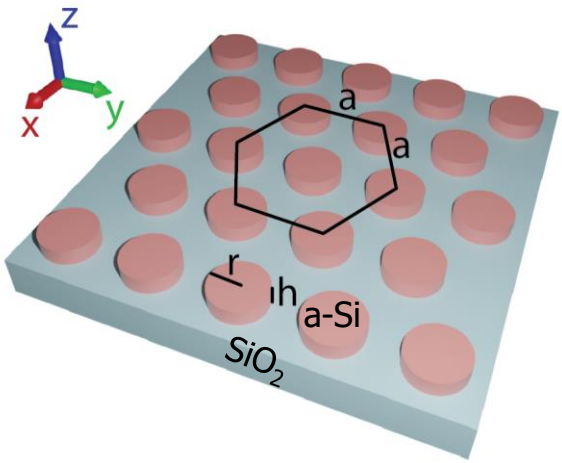

Figure 4.2 Schematic of the proposed all-dielectric metasurfaces [165].

The nanodisk parameters are optimised to achieve two pronounce electric and magnetic dipole resonances with large spectral gap between them. The simulated transmission spectrum is shown in Fig. 4.3(a). Figure 4.3(a) indicates that the resonance depths appear at 1400 nm and 1570 nm wavelengths, where the light transmission is almost zero at the normal incidence. We are aiming to make a high-pass spatial frequency filter, therefore, near-zero transmission at the normal incidence is highly desirable. Such a filter can precisely block the lower k-components of the image. To further investigate the resonance behaviour, we have analysed the Cartesian multipolar decomposition of the designed metasurface, shown in Fig. 4.3(b).

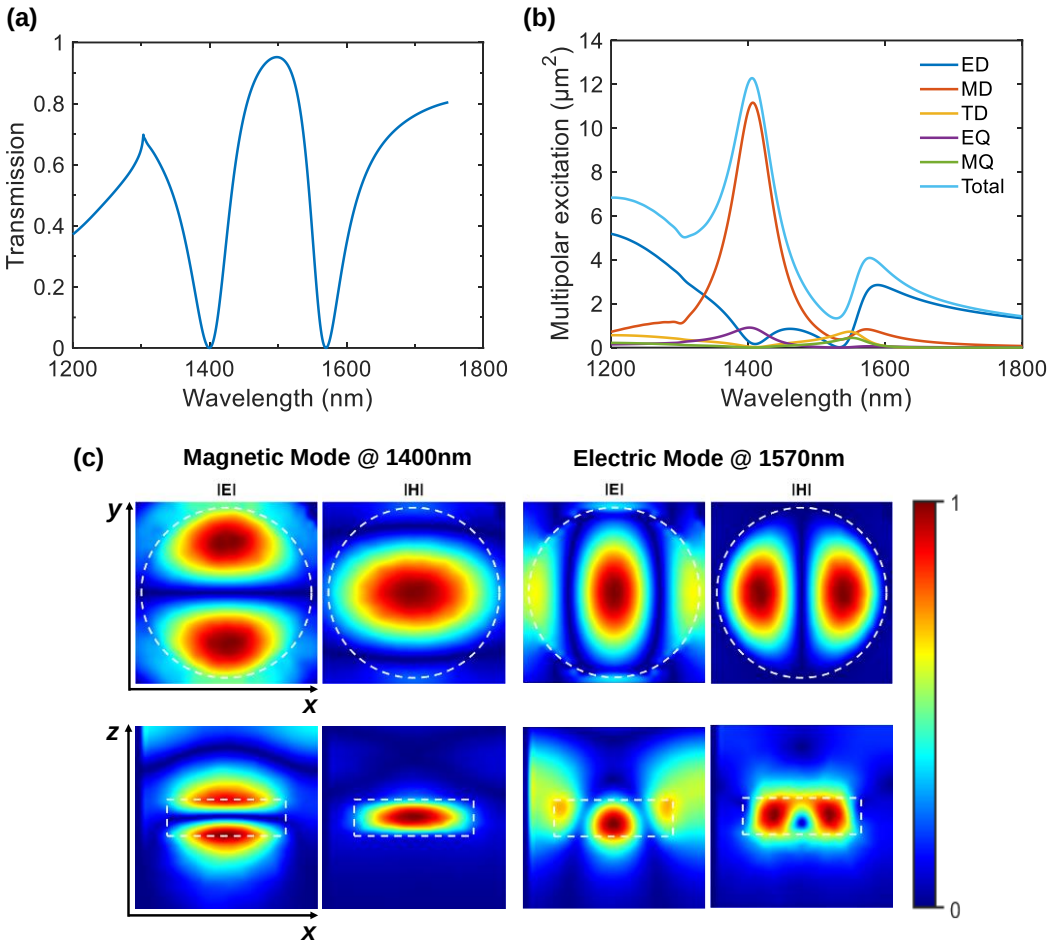

Figure 4.3 (a) Simulated transmission spectra. (b) Simulated multipolar decomposition under plane wave excitation, and (c) magnetic and electric field profiles at the resonant wavelengths [165].

I have used equations 1.9 - 1.12 to perform the Cartesian multipolar decomposition analysis. It is clearly visible in Fig. 4.3(b) that the resonance at 1400 nm is a MD resonance, which is dominant compared to the ED resonance (1570 nm). The dominant MD resonance is partly supported by the EQ resonance at the background. The mode-profiles at the ED and MD resonance wavelengths are shown in Fig. 4.3(c). Based on the mode-profiles, it confirms the Mie-type nature of the resonances, and the main multipole contributor to the resonance effect of ED and MD.

4.3 Angular Dispersion Analysis and Numerical Edge Detection

I have numerically investigated the angular dispersion at the electric and magnetic resonances, shown in Fig. 4.4. I have investigated the angular dispersion analysis using

the Lumerical FDTD software. In these simulations, I have used periodic boundary conditions. The results are presented for both horizontal x-polarisation and vertical y-polarisation states of light. At a specific polarisation state (x- or y-polarisation), I varied the in-plane and out-of-plane azimuthal angles.

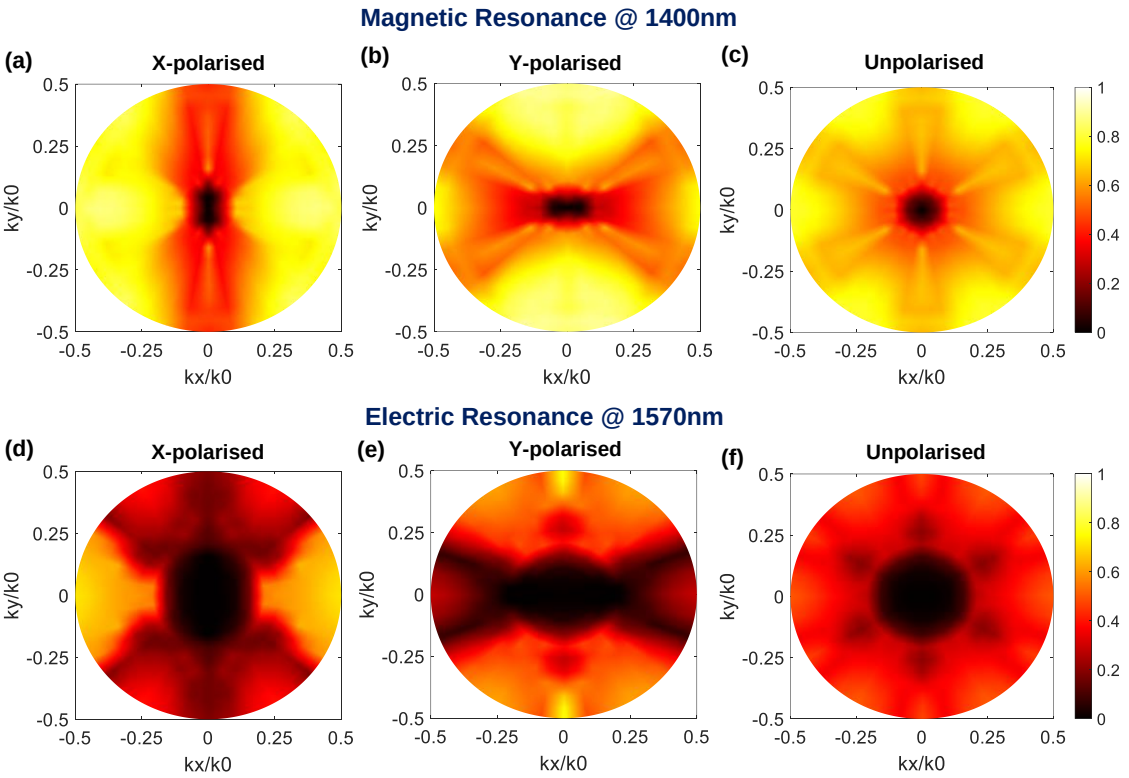

Figure 4.4 Simulated angular dispersion of the metasurface. (a) Transmittance of the metasurface with varying the incident angles up to 30 degrees at magnetic resonance wavelength of 1400 nm, and (b) transmittance of the metasurface with varying the incident light up to 30 degrees at the electric resonance wavelength of 1570 nm [165].

I altered the out of-plane azimuthal angles from 0 to 30° with a 1° iteration and in-plane azimuthal angles from 0 to 360° with a 2° iteration. Figures 4.4(a-c) shows the angular dispersion at the MD resonance wavelength of 1400 nm. At the normal incidence, x-polarised and y-polarised incidence light completely block the transmission. For the longer wavelength, it exhibits highly transmissive response. To get the results of transmittance for unpolarised light, I calculated the mean value between transmittance of x- and y-polarised states. Figure 4.4(c) exhibits the unpolarised angular dispersion which indicates better filter properties. Due to hexagonal disk arrangement, the six-fold of symmetry is clearly noticeable, and narrow down the near-zero transmission area.

Therefore, it will lead to achieve a nice inverse- Gaussian type angular dispersion response. This is the key criteria to have a clear edge detection of a target image, as the zero-transmission area will cut k-space frequencies that respond to the forward propagation of light. From angular dispersion analysis, it is also clearly noticeable that in x-polarized and y-polarized states, the maximum light transmits in only one direction either x or y-axis and other direction transmit less amount of light. However, unpolarized angular dispersion profile exhibits uniform light distribution in both directions. Therefore, unpolarized light will exhibit better edge detection compared to the x- and y-polarized states. The angular dispersion for electric resonance is shown in Figs. 4.4(d-f). The electric mode resonance also does not transmit the low frequency components. Also, the transmittance of the high frequencies is very low. Therefore, it blocks propagation for all k-space frequencies, which make such a filter impractical for real applications, because of its low efficiency. Therefore, for the experimental investigations, we have further considered the magnetic dipole resonance state.

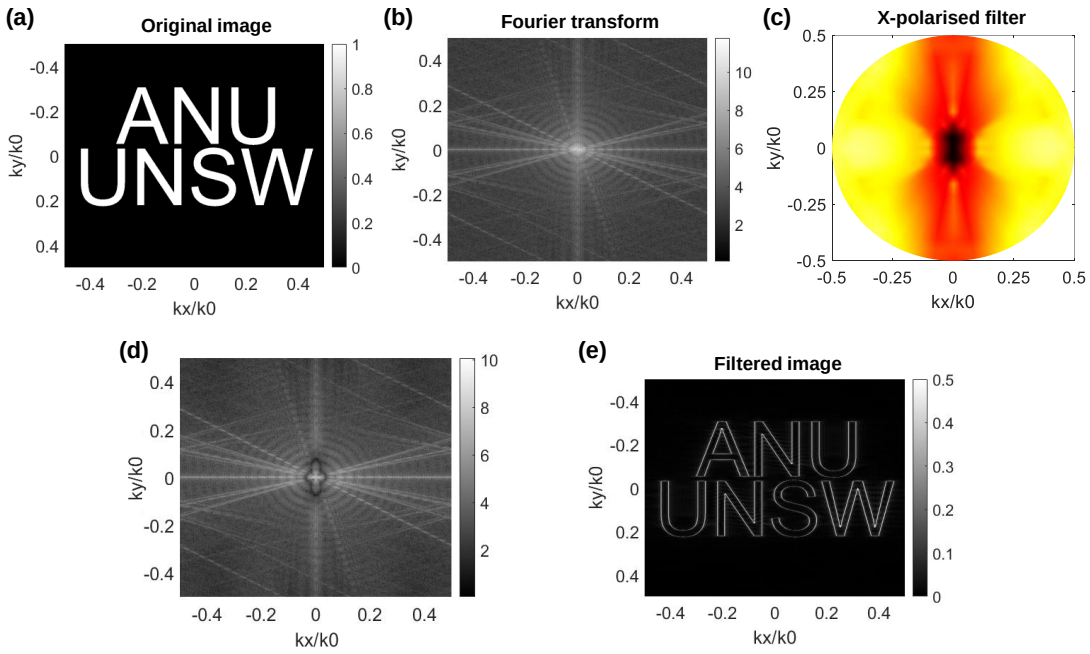

Figure 4.5 Image filtering process. (a) Target image. (b) Fourier transform of the target image. (c) x-polarised angular dispersion at the magnetic resonance wavelength of 1400 nm. (d) Multiplication result of Fourier transform and filter, and (e) filtered image.

Using the simulated filter, the detail filtering process is shown in Fig. 4.5. Figure 4.5(a) shows the target image which has several sharp edges. The image size is 1000 × 1000 pixels. The number of pixels, discretisation, can be arbitrary, it defines the discrete

frequency of our numerical experiment. The Fourier transform of the target image is shown in Fig. 4.5(b). Numerically designed x-polarisation angular dispersion response is shown in Fig. 4.5(c). As I described earlier, to perform the high efficiency edge detection, it requires to have a high-pass filter. In the given angular dispersion profile, if we do a line scan along the x- or y-axis at the normal incident, it will provide the inverse-Gaussian type response.

Therefore, it will work as a high-pass filter, which will cut the lower k-space frequencies. To apply the inverse-Gaussian filter in Fourier space, multiplied the designed filter with the Fourier transform, and the output is shown in Fig. 4.5(d). Finally, I implement the inverse Fourier transform of our filtered image, which leads to our desired edge detection of the given image (Fig. 4.5(e)).

The simulated edge detection image for the x-polarised, y-polarised, and unpolarised incident light at electric resonance and magnetic resonance states is shown in Fig. 4.6.

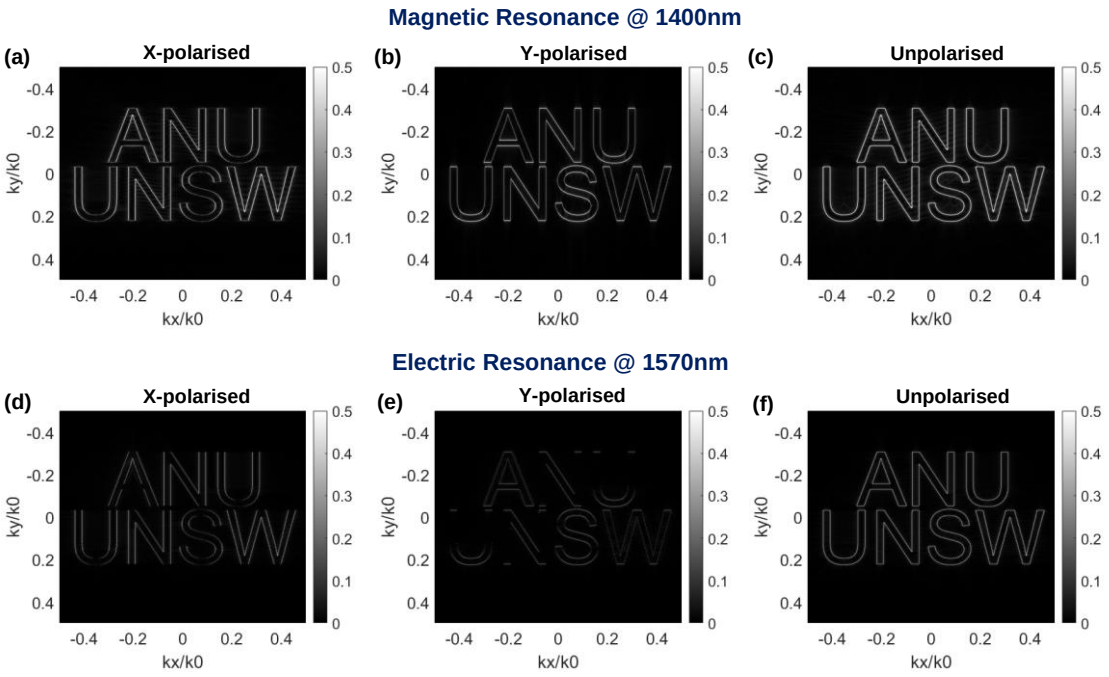

Figure 4.6 Simulated edge detection. At the magnetic dipole resonance wavelength of 1400 nm for (a) x-polarised, (b) y-polarised, and (c) unpolarised incident light. Edge detection at the electric dipole resonance wavelength of 1570 nm for (d) x-polarisation, (e) y-polarisation and (f) unpolarised incident light.

The simulated edge detection image for the x-polarised, y-polarised, and unpolarised incident light at electric resonance and magnetic resonance states is shown in Fig. 4.6. At the magnetic resonance state, the x-polarised (Fig. 4.6(a)) and y-polarisation (Fig. 4.6(b)) incident shows high efficiency edge detection as per the previous prediction based on the angular dispersion analysis. Therefore, unpolarised light provides even higher efficiency edge detection, as it processed based on the mean value of transmittance for x-polarised and y-polarised states. The edge detection at the electric resonance state is shown in Figs. 4.6(d-f). In angular analysis (Figs. 4.4(d-f)), we have seen that the transmittance of the high frequencies was low, therefore, most of the k-space frequencies are blocked. As a result, at the ED resonance, the efficiency of the edge detection in different polarisation states is poor.

4.4 Experimental Verification of Edge Detection

The SEM of the fabricated metasurface is shown in Fig. 4.7(a). The inset figure shows the zoomed view of the hexagonal nanodisk arrangement. The sample was fabricated following the standard EBL method followed by lift-off process. The detail of the fabrication process is given in Sec. 2.2.2. The experimentally measured linear transmission response is shown in Fig. 4.7(b).

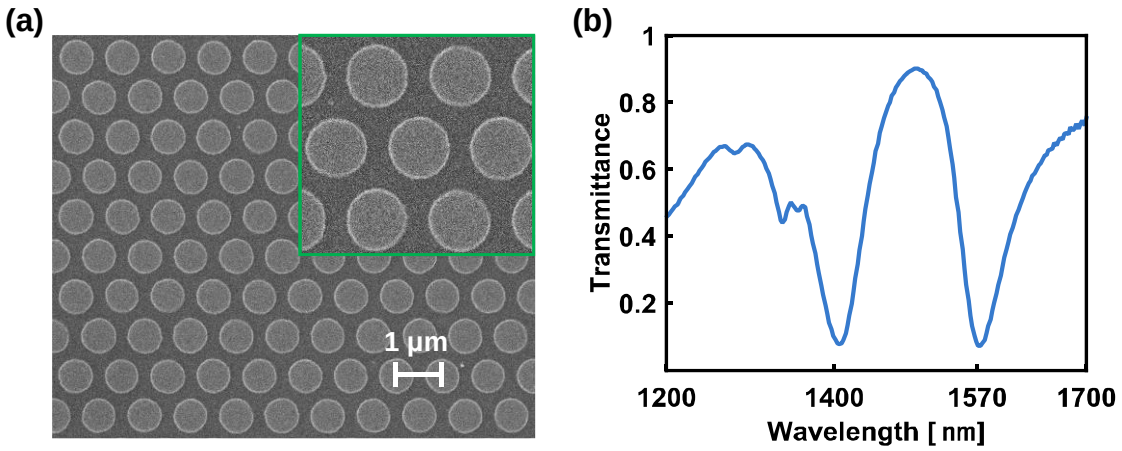

Figure 4.7 (a) SEM of the fabricated metasurfaces, and (b) experimentally measured transmission spectra [165].

The home-built transmission setup details are given in Sec. 2.2.2. The experimentally measured transmission spectra also show two resonance depths at the wavelength's of

1400 nm and 1570 nm. It has well agreement with the numerically calculated transmission spectra (see Fig. 4.3(a)). However, it is worthy to note that, at the resonance wavelengths, it exhibits around 8% transmission, which is because of the fabrication imperfection and residual angular spread around the zeroth *k*-vectors in our transmission setup. Although the ideal case has zero transmittance at the normal incidence, the 8% transmittance is still acceptable to achieve a clear edge detection of a target image. The experimental setup for the edge detection is shown in Fig. 4.8. We tried to make the experimental setup as simple as possible to make it suitable for the real-world applications. The setup has four major components such as a laser source, a target image, the fabricated metasurface (will work as a high-pass filter) and imaging camera with a lens at the focal distance. We have used a Chameleon tuneable femtosecond laser and Chameleon optical parametric oscillator (OPO). A set of filters after the OPO was used

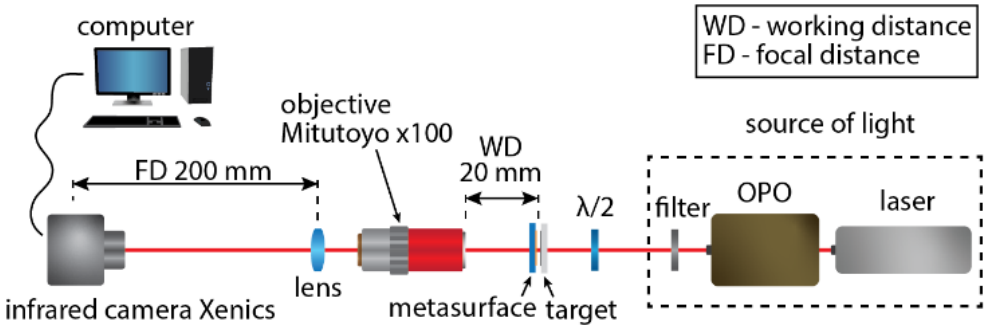

Figure 4.8 Schematic of the experimental setup for the edge detection [165].

to reduce the power to make it comparable to daylight level of several micro watts. The edge detection is a linear effect, and the intensity of light does not play any role unless it is high enough to damage the metasurface. The source of the light is linearly polarised, therefore, to investigate the polarisation dependency, we have used a half-wave plate. Rotating the half-wave plate, we rotate the polarisation of the laser light. We have used a R1L3S5P positive Thorlabs resolution test target to perform the edge detection. We placed the target close to the metasurface. Our fabricated metasurface size is 1×1 mm^2 size. Therefore, our target image should be half in linear size (500 µm) to be able to filter beams with high *k*-space frequencies (high angles). We have used a 100× objective to cover the higher angular lights. Finally, we captured the filtered image using a Xenics InGaAs infrared camera (XS-1.7-320).

We have used the NBS 1963A resolution target image to experimentally perform the edge detection. The target image has five horizontal and five vertical stripes with equal widths of the stripes and equal distances between them. The size of the stripes is 45 µm with equal gap size. The experimentally measured edge detection at the magnetic dipole resonance wavelength of 1400 nm is shown in Figs. 4.9(a, b). Figure 4.9(a) depicts the edge detection for the horizontal stripe, and Fig. 4.9(b) exhibits the edge detection for the vertical stripes. In Figures 4.9(a, b), there is a target image, and the edge detection image. We have captured the initial image and edge detection image by removing and inserting our designed metasurface filter. It is clearly noticeable that, the edge detection images show only the intensity lines at the boundary of the horizontal and vertical stripes. The overall intensity of the edge detection images is small.

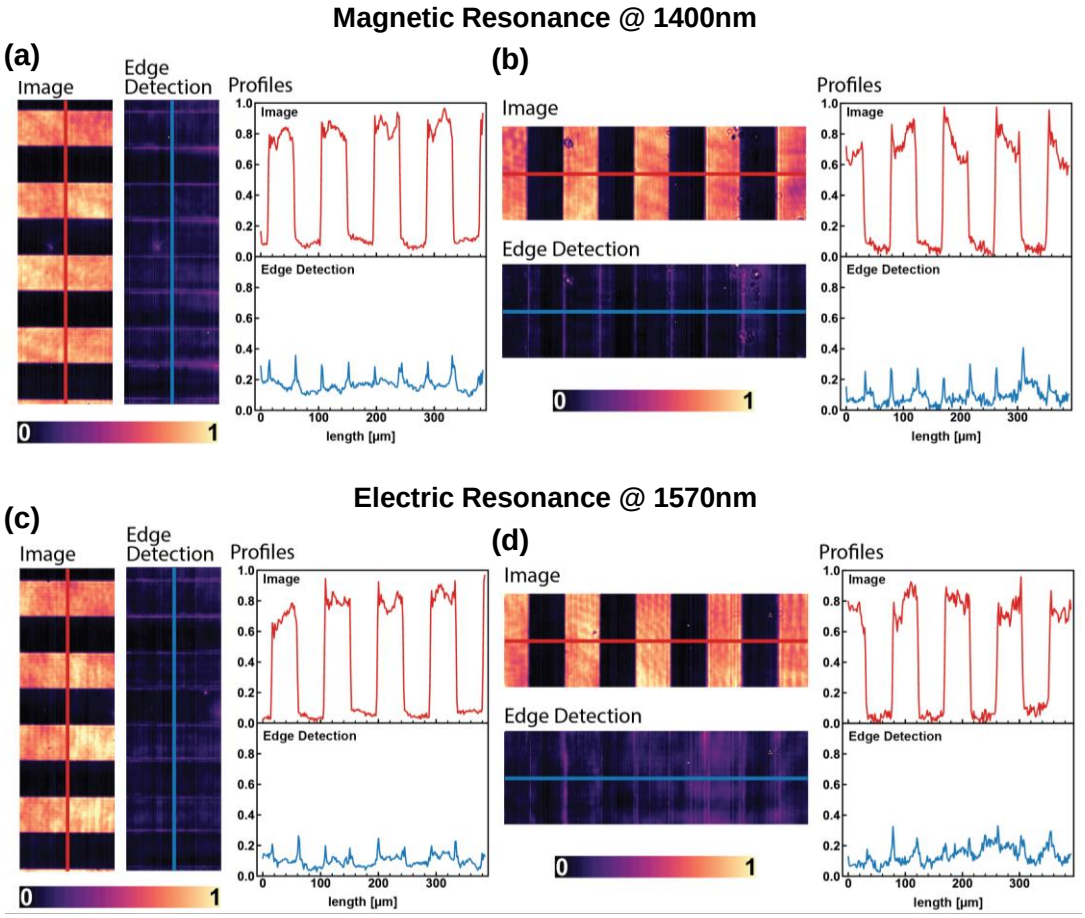

Figure 4.9 Experimental edge detection. Edge detection for the magnetic mode at 1400 nm for (a) horizontal stripes and (b) vertical stripes. Edge detection for the electric mode at 1570 nm for (a) horizontal stripes and (b) vertical stripes [165].

However, this is completely in agreement with the Fourier filtering theory, because we cut the high-intensity harmonics. We also performed a line scan for the horizontal and vertical stripes, which provides better quantitative analysis. From the line scan, it is clearly visible that the proposed metasurface can perform the edge detection for both horizontal and vertical stripes equally. Similarly, we have also experimentally performed the edge detection at the electric dipole resonance state, shown in Figs. 4.9(c, d). From the edge detection images as well as line scan, it is clearly visible that electric resonance state is also able to perform the edge detection for both horizontal (Fig. 4.9(c)) and vertical stripes (Fig. 4.9(d)).

I previously numerically predicted via angular dispersion analysis that (see Figs. 4.4(d-f)), edge detection efficiency in low at the electric resonance state. We also experimentally observed the similar scenario where the edges of the detected image are more pronounced at the magnetic resonance state compared to the electric resonance state. It is worthy to note that, as soon as low frequency special modes are cut and even a little transmittance remains for the higher frequencies, the edge detection effect can be observed.

We have further investigated the polarisation dependency of the proposed metasurface, shown in Fig. 4.10. In most of the real-world applications, light will be unpolarised, therefore, this is very critical to have a polarisation independent edge detection device. We experimentally observed the angular dependency for both horizontal stripes (Fig. 4.10(a)) and vertical stripes (Fig. 4.10(b)). We have measured the edge detection in four polarisation states such as, 0^o (horizontal), 45^o, 90^o (vertical) and 135^o. In this experiment, we have used the same target image and considered maximum pixel value for the edge detection result, as we are aiming to see the variation of the intensity due to different polarisation states. The higher intensity at the edges of the target is due to the alignment issues of the overall optical setup. Due to sophisticated optical system, due to small misalignment leads to a significant effect. However, from Figs. 4.10(a, b), it is clearly visible that edge detection response is almost same due to change of polarisation states. For better clarification, we have used an intensity line scan of the filtered image at the normal incidence, and considered it as a reference line. Later, subtracted the intensity for other polarisation states from the reference intensity line, and presented them accordingly. For both horizontal and vertical stripes, the edge detection effect is almost same for all four linear polarisation states. Therefore, we can say that the proposed metasurface exhibits polarisation independent edge detection response.

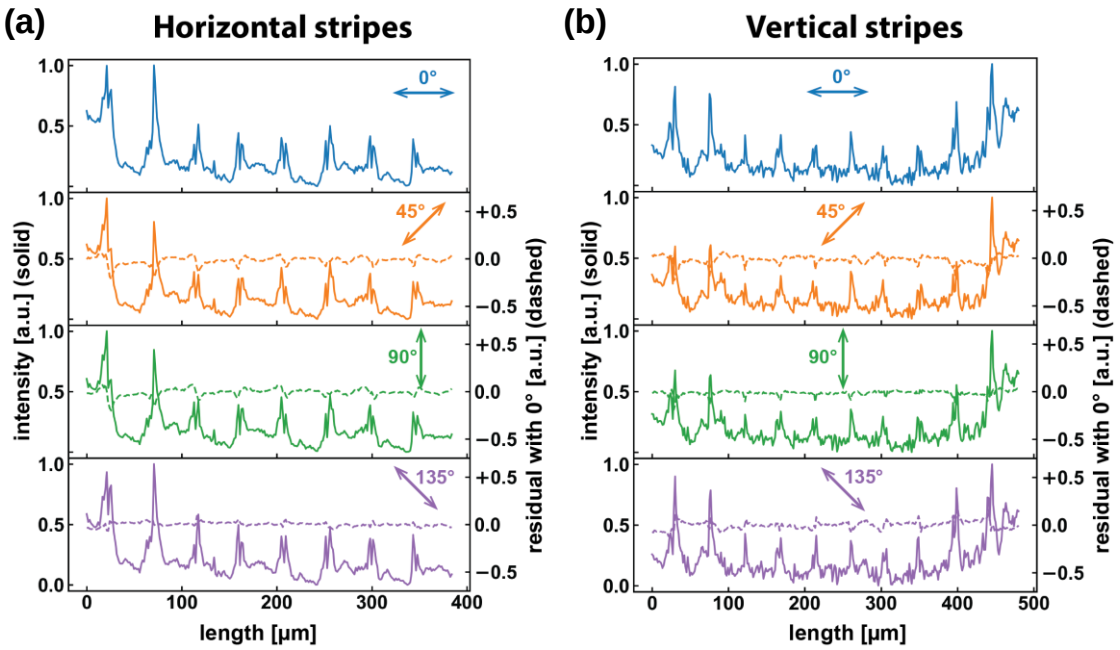

Figure 4.10 Polarisation dependence of the edge detection for the magnetic dipole resonance at 1400 nm for (a) horizontal stripes, and (b) vertical stripes [165].

4.5 Resolution of Edge Detection

To understand the edge detection performance, it is important to investigate how smallest features can be detected by the proposed dielectric metasurface. The smallest feature detection capability is also scientifically known as resolution. We define the resolution as the distance between two edges that can be clearly resolved after Fourier filtering with an inverse-Gaussian filter in k-space. We have considered single squared pulse function with the width 2T, shown in Fig. 4.11(a). Later, identify the width of the inverse-Gaussian filter by checking when two edges start blurring while passes through the high-pass filter. Figure 4.11(b) shows the Fourier transform of initial signal and filters with different widths. The blue curve indicates the pulse signal. The selective frequency transmittance has been determined by the inverse-Gaussian shape filter. It can be expressed as:

$$g(w) = 1 - e^{-\frac{\omega^2}{2\sigma^2}}, \tag{4.7}$$

where σ is the width of the filter. We have applied three filters with three different widths such as, $\sigma = \pi/2T$, $\sigma = \pi/T$, and $\sigma = 2\pi/T$.

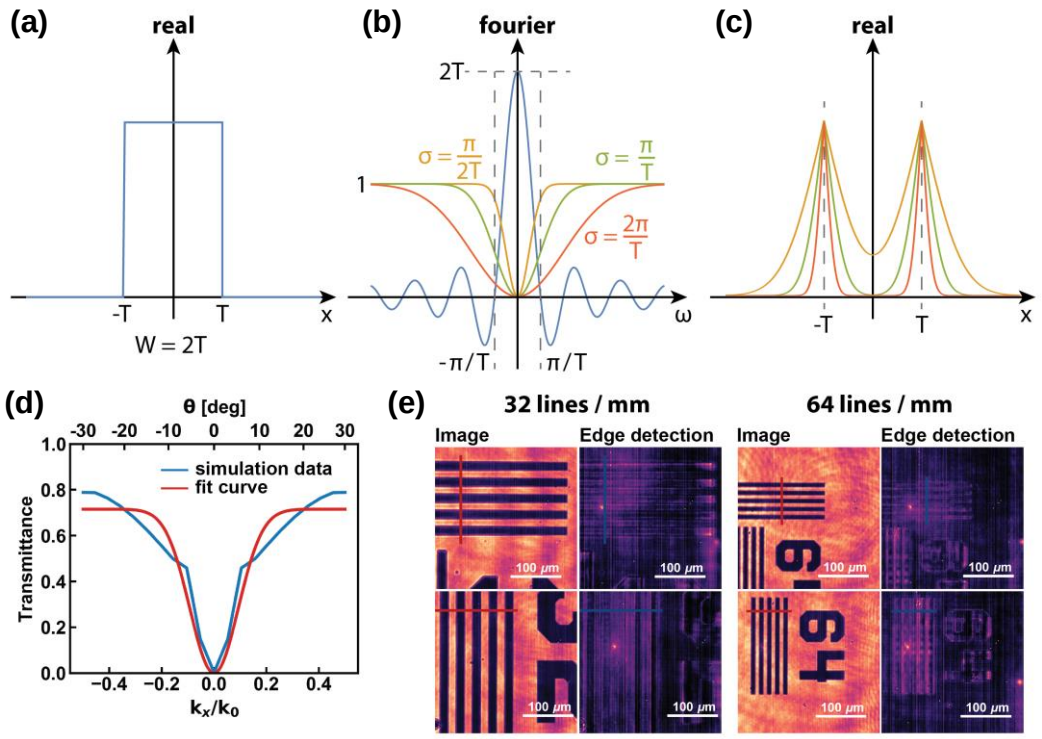

Figure 4.11 Resolution of edge detection. (a) Initial signal. (b) Fourier transform of the initial signal with different widths. (c) Filtered edge detection image. (d) Line scan of simulated x-polarised angular dispersion at the magnetic resonance of 1400 nm wavelength. (e) Experimental edge detection for targets with 32 and 64 lines per mm [165].

The results of the multiplication of different filters with the Fourier transform of the initial signal provide the filtered function. Finally, inverse Fourier of the filtered function provides the edge detection of the initial image, as shown in Fig. 4.11(c). According to Fig. 4.11(c), the edges of the initial signal start overlapping while used the filter width of $\sigma = \pi/T$ and $\sigma = 2\pi/T$. For the filter width of $\sigma = \pi/2T$, it shows the edges are almost half-overlap, however, they still can be resolved. We define W as the resolution of the edge detection for inverse-Gaussian filtering in the frequency, therefore, filter width can be expressed as, $\sigma = \pi/W$. Figure 4.11(d) shows the line scan of the simulated angular dispersion at the magnetic resonance wavelength of 1400 nm (see Fig. 4.4(a)). The width of the fitted curve is equal to $\sigma = 0.1k_0$, where $k_0 = 2\pi/\lambda$. So, the calculated resolution can be derived as:

$$W = \frac{\pi}{\sigma} = \frac{\pi}{0.1k_0} = \frac{\pi}{0.1} \times \frac{\lambda}{2\pi} = \frac{\lambda}{0.2} \quad . \tag{4.8}$$

The operating wavelength of the magnetic resonance is 1400 nm, so the resolution is $W = 1.4/0.2 = 7$ µm.

We have also experimentally measured the resolution of our metasurface edge detection. Figure 4.11(e) shows the horizontal and vertical stripes of 32 and 64 lines per mm, which gives the stripes widths of 15 µm and 8 µm, respectively. According to Fig. 4.11(e), while using the 64 lines per mm target, the filtered image exhibits the edges of the target image overlapping and blurred which matched well the calculated resolution.

4.6 Summary

In this chapter, I have numerically and experimentally demonstrated dielectric metasurface based advanced image processing technique in the form of edge detection without the need of any additional components. First, I have presented the metasurface design criteria and investigated the Mie-resonance features. Consequently, I have showed the numerical angular dispersion profiles for both electric and magnetic resonant states. The transmittance amplitude of the angular dispersion response works as a high-pass spatial frequency filter. I have also briefly described the numerical edge detection process. Next, I verified the numerical edge detection claims experimentally. A Thorlabs target image (NBS 1963A resolution) was used to experimentally perform the edge detection. The edge detection was carried out at both electric and magnetic resonance states. Our experimental results also exhibit that magnetic resonance state provides better edge detection efficiency compared to the electric resonance state. The polarisation independent edge detection response was experimentally verified, which is one of the key findings of this work. Finally, the resolution of the proposed metasurface was investigated to understand how smallest features are detectable using the proposed metasurface. The proposed metasurface numerically and experimentally showed that larger than 8 µm object is easily detectable. The presented metasurface is demonstrated a fully functioning ultrathin optical device for passive edge detection, possibly to integrate with any other optical system. The proposed silicon metasurfaces can pave the way for optical imaging applications, including microscopy and navigation for autonomous systems.

Chapter 5

Conclusion and Outlook

5.1 Conclusion

Since last few years, the development and study of optical metasurfaces has been a rapidly growing field of research, due to advanced control of light characteristics, such as polarisation, dispersion, amplitude, and phase. Optical metasurfaces can mimic the conventional optical elements with higher efficiency and resolutions. Moreover, optical metasurfaces can provide new functionalities with high efficiency, due to their spatially varying optical responses for wavefront manipulation, which is not achievable with conventional optics. The researchers have already explored all the possible fundamental applications using the optical metasurfaces by varying the geometries, working regimes, sophisticated designs, and so on. However, subwavelength wave discretisation is one of the key aspects, which can efficiently manipulate the incoming light. The efficient control of incoming light opens a new paradigm to achieve novel functionalities not possible with conventional optics.

In this thesis first (Chapter 1), I have presented the fundamentals of plasmonic and dielectric metasurfaces. Consequently, I have explored the recent development of metasurfaces. I have also investigated the different types of resonance behaviours for dielectric metasurfaces. Finally, I have extensively explored the phase discretisation concept to improve the efficiency of the metasurfaces. The arbitrary phase control using resonant and non-resonant nanostructures was also briefly studied.

In Chapter 2, I have numerically and experimentally shown the beam deflection with high efficiency at the visible and THz regions. First, I have presented the effect of the deflection angle on the metasurface performance. The proposed small deflection angle (8.60^{o}) based supercell showed the transmission efficiency of 95% with deflection efficiency of 95% at the operating wavelength of 715 nm. I have also presented an advanced beam-deflector by introducing 3π-phase gradient. It exhibits the multiplexing facility and leads to split the incoming beam into higher diffraction orders. Subsequently, I have presented the deeply subwavelength meander-gap resonator based efficient beam manipulation at the THz regime. An advanced EBL technique was used to reduce the

resonator size to $\lambda/23$ and capacitive gaps $\lambda/1136$, which significantly mitigate the undesirable effects due to sparse discretisation, including spatial dispersion, mutual interaction, and discretisation error.

In Chapter 3, I have shown a metasurface based novel optical sensing techniques with improved robustness and performance. Firstly, I have numerically demonstrated a hybrid metasurface (metal-dielectric) platform, which shows the near-unity absorbance and facilities to work as a refractive index sensor. Next, I have numerically and experimentally showed a novel dielectric metagrating based optical biosensing concept. This resonant metagrating based optical sensing approach enables the direct measurement of unknown analytes with enhanced sensitivity, and without the need for intensity calibrations. The proposed SDA metagrating provides significant signal intensification facility, which leads to achieve the maximum sensitivity of 26,266 RIU^{-1} within the sensing range of 1.331 to 1.401. The functionalisation process was carried out to detect the biomarker anti-Mouse IgG. The proposed SDA metagrating sensor exhibits the minimum femtomolar concentration anti-Mouse IgG detection capability with the LOD of ~770 fM. Additionally, the specificity of the sensor was investigated. The proposed sensor exhibits a highly selective capture of biomarkers in a complex medium.

In Chapter 4, I have shown another new functionality, image processing using dielectric metasurfaces. First, I briefly derived the 2^{nd} derivative of the Fourier transformation, which can perform the edge detection. I have numerically and experimentally demonstrated the dielectric metasurface based advanced image processing in the form of edge detection. A hexagonal lattice arrangement has been used to protect the symmetry and the Mie-type resonance features have been utilised to achieve high efficiency edge detection. I have numerically investigated the angular dispersion for different polarisation states, which exhibits very nice high-pass filter feature. Later, I numerically performed edge detection for different polarisation states at the ED and MD dipolar resonance wavelengths of 1400 nm and 1570 nm, respectively. Finally, this edge detection concept has been experimentally verified using a Thorlabs NBS 1963A resolution target image. The efficient edge detection was confirmed by detecting both horizontal and vertical stripes. Subsequently, the different polarisation effects were also experimentally investigated. The proposed metasurface showed the polarisation independent edge detection response, which is an important feature for real-world applications. Finally, the detection resolution of the proposed metasurface has been

numerically and experimentally measured and is found to be 8 µm for the designed metasurface.

Overall, in my thesis, I have extensively studied the subwavelength wave discretisation to reveal a new, flexible route to design the high efficiency metadevices with new advanced functionalities, such as smart beam deflection, metagrating based optical biosensing, and advanced image processing in a form of edge detection.

5.2 Outlook

The field of metasurface is a rapidly developing research area. In this thesis, I have focussed on three different applications controlling the phase responses of the meta-atoms and the metasurfaces. These works could be further extended significantly in several different directions.

The demonstrated feature of efficient beam steering (Chapter 2) can be applied for driverless or autonomous cars. The key part of the autonomous car is LiDAR. It helps to measure the distance of an object by illuminating the object with a pulsed laser and detect the reflected signal with a sensor [85]. Figure 5.1 shows the schematic diagram of the working principle of 3D LiDAR. From Fig. 5.1, it is noticeable that the incoming light needs to deflect to scan the objects. Therefore, a meta-deflector with large beam steering angle is highly desirable. Moreover, a dynamic beam steering feature is required to continuously scan the objects in different positions.

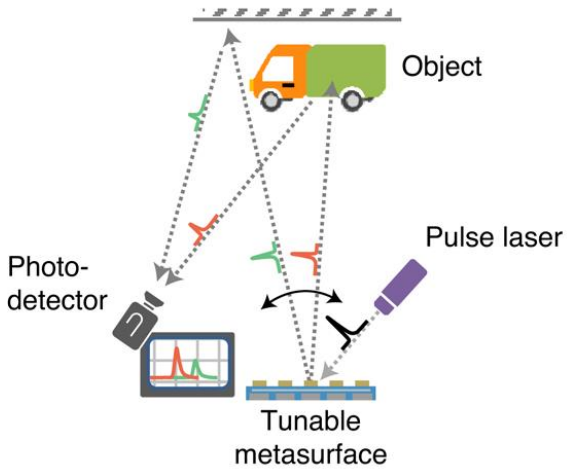

Figure 5.1 Schematic diagram of the 3D LiDAR working principle [85].

In Chapter 2, I have extensively studied the fundamentals of the beam deflector to enhance the deflection efficiency. Also, I experimentally demonstrated one smart deflector, which exhibits the possibility to multiplex the beams to route at a large deflection angle. By incorporating a dynamic beam steering feature via either liquid crystals, thermal tuning, phase-change materials, changing of the surrounding medium, and so on [175], one can possibly realise a fully functioning dynamic beam deflector.

Another possible interesting research direction could be to realise nanorobots based on meta-deflectors to kill cancer cells, deliver drugs to target tissues, or improve vaccine delivery. The schematic of magnetic nanorobots is shown in Fig. 5.2(a). Nanorobots are potentially the future of medical technology, especially for medical treatment of a patients [176]. As an example, one can use the nanorobots which will examine the cells from inside and destroy the affected cells. Very recently, Andren *et al.* proposed a microscopic meta-vehicles powered and steered by dielectric meta-deflector (see Fig. 5.2(b)) [177]. The proposed technique showed the transport of microscopic particles which can travel long distance even in a complex path. I strongly believe that using the advanced meta-deflector with microscopic particle movement features, one can realise fully functioning nanorobots for medical technology.

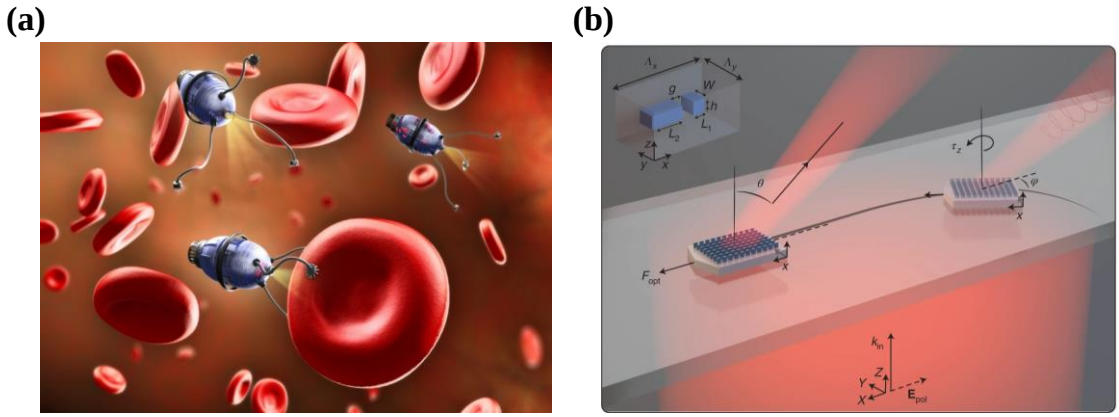

Figure 5.2 (a) Magnetic nanorobots [178], and (b) Microscopic metavehicles [177].

Integration of multiplex sensing feature is another important research direction, which could be realised using the proposed metagrating based sensing approach. As we briefly discussed in Chapter 3, the proposed resonant metagrating represents a highly sensitive platform with femtomolar concentration detection capability. Therefore,

integration of simultaneous multiple analyte detection capability in this metagrating platform will significantly improve the fast detection capability, will be cost effective, and will be able to avoid the false positive response, which will drastically boost the sensing technology.

Tuneable edge detection is also an important possible research direction. The tuneable feature will provide extra freedom to switch between the original and the edge detected object. As we briefly described in Chapter 4, the ultrathin dielectric metasurface can efficiently perform polarisation independent edge detection of a target image. It works by achieving nearly zero transmission dip at the normal incidence, which blocks the lower k-components, therefore performs the optical edge detection. Utilizing different states, e.g. one state will show low transmission and another state will show high transmission without change of the operating wavelength, then we will be able to utilise the metasurface for tuneable edge detection. Such tuneable feature can be realised by using liquid crystal cells, polarisation, phase change materials, changing the surrounding medium, and so on [175]. Therefore, there are plenty of room to investigate the efficient tuneable edge detection feature. Additionally, optical metasurface based high efficiency phase-contrast imaging is another important research direction, which could replace the conventional label-free microscopy technique to visualise the biological objects [12, 179, 180].

In summary, in my thesis, I have studied optical metasurfaces with advanced phase control feature to explore three different applications, such as beam deflection, optical biosensing, and edge detection. However, metasurfaces have a lot of room to explore in a different new avenue of technology, which will lead to smart and ultra-compact optical devices.

Bibliography

[1] C. L. Holloway, E. F. Kuester, J. A. Gordon, J. O'Hara, J. Booth, and D. R. Smith, "An overview of the theory and applications of metasurfaces: The two-dimensional equivalents of metamaterials," *IEEE Antennas and Propagation Magazine,* vol. 54, no. 2, pp. 10-35, 2012.

[2] A. V. Kildishev, A. Boltasseva, and V. M. Shalaev, "Planar photonics with metasurfaces," *Science,* vol. 339, no. 6125, 2013.

[3] N. Yu and F. Capasso, "Flat optics with designer metasurfaces," *Nature Materials,* vol. 13, no. 2, pp. 139-150, 2014.

[4] I. Staude and J. Schilling, "Metamaterial-inspired silicon nanophotonics," *Nature Photonics,* vol. 11, no. 5, pp. 274-284, 2017.

[5] H. H. Hsiao, C. H. Chu, and D. P. Tsai, "Fundamentals and applications of metasurfaces," *Small Methods,* vol. 1, no. 4, p. 1600064, 2017.

[6] Y. Kivshar and A. Miroshnichenko, "Meta-optics with Mie resonances," *Optics and Photonics News,* vol. 28, no. 1, pp. 24-31, 2017.

[7] P. Genevet, F. Capasso, F. Aieta, M. Khorasaninejad, and R. Devlin, "Recent advances in planar optics: from plasmonic to dielectric metasurfaces," *Optica,* vol. 4, no. 1, pp. 139-152, 2017.

[8] P. Qiao, W. Yang, and C. J. Chang-Hasnain, "Recent advances in high-contrast metastructures, metasurfaces, and photonic crystals," *Advances in Optics and Photonics,* vol. 10, no. 1, pp. 180-245, 2018.

[9] M. L. Brongersma, "The road to atomically thin metasurface optics," *Nanophotonics,* vol. 10, no. 1, pp. 643-654, 2021.

[10] W. Liu, H. Cheng, J. Tian, and S. Chen, "Diffractive metalens: from fundamentals, practical applications to current trends," *Advances in Physics: X,* vol. 5, no. 1, p. 1742584, 2020.

[11] G. Zheng, H. Mühlenbernd, M. Kenney, G. Li, T. Zentgraf, and S. Zhang, "Metasurface holograms reaching 80% efficiency," *Nature Nanotechnology,* vol. 10, no. 4, pp. 308-312, 2015.

[12] L. Wesemann *et al.*, "Nanophotonics enhanced coverslip for phase imaging in biology," *Light: Science & Applications,* vol. 10, no. 1, pp. 1-6, 2021.

[13] Y. Zhou, H. Zheng, I. I. Kravchenko, and J. Valentine, "Flat optics for image differentiation," *Nature Photonics,* vol. 14, no. 5, pp. 316-323, 2020.

[14] J. Hu, S. Bandyopadhyay, Y.-h. Liu, and L.-y. Shao, "A Review on Metasurface: From Principle to Smart Metadevices," *Frontiers in Physics,* vol. 8, p. 502, 2021.

[15] W. T. Chen, A. Y. Zhu, and F. Capasso, "Flat optics with dispersion-engineered metasurfaces," *Nature Reviews Materials,* vol. 5, no. 8, pp. 604-620, 2020.

[16] F. Hopkinson and D. Rittenhouse, "An optical problem, proposed by Mr. Hopkinson, and solved by Mr. Rittenhouse," *Transactions of the American Philosophical Society,* vol. 2, pp. 201-206, 1786.

[17] J. Huang and J. A. Encinar, *Reflectarray antennas*. John Wiley & Sons, 2007.

[18] D. Pozar and T. Metzler, "Analysis of a reflectarray antenna using microstrip patches of variable size," *Electronics Letters,* vol. 29, no. 8, pp. 657-658, 1993.

[19] Z. e. Bomzon, V. Kleiner, and E. Hasman, "Pancharatnam–Berry phase in space-variant polarization-state manipulations with subwavelength gratings," *Optics Letters,* vol. 26, no. 18, pp. 1424-1426, 2001.

[20] Z. e. Bomzon, V. Kleiner, and E. Hasman, "Formation of radially and azimuthally polarized light using space-variant subwavelength metal stripe gratings," *Applied Physics Letters,* vol. 79, no. 11, pp. 1587-1589, 2001.

[21] N. Yu *et al.*, "Light propagation with phase discontinuities: generalized laws of reflection and refraction," *Science,* vol. 334, no. 6054, pp. 333-337, 2011.

[22] N. Yu, F. Aieta, P. Genevet, M. A. Kats, Z. Gaburro, and F. Capasso, "A broadband, background-free quarter-wave plate based on plasmonic metasurfaces," *Nano Letters,* vol. 12, no. 12, pp. 6328-6333, 2012.

[23] W. Mo, X. Wei, K. Wang, Y. Li, and J. Liu, "Ultrathin flexible terahertz polarization converter based on metasurfaces," *Optics Express,* vol. 24, no. 12, pp. 13621-13627, 2016.

[24] D. Wen *et al.*, "Metasurface for characterization of the polarization state of light," *Optics Express,* vol. 23, no. 8, pp. 10272-10281, 2015.

[25] A. Shaltout, J. Liu, A. Kildishev, and V. Shalaev, "Photonic spin Hall effect in gap–plasmon metasurfaces for on-chip chiroptical spectroscopy," *Optica,* vol. 2, no. 10, pp. 860-863, 2015.

[26] D. A. Atchison, "Spectacle lens design: a review," *Applied Optics,* vol. 31, no. 19, pp. 3579-3585, 1992.

[27] M. Chen, R. Sabesan, K. Ahmad, and G. Yoon, "Correcting anterior corneal aberration and variability of lens movements in keratoconic eyes with back-surface customized soft contact lenses," *Optics Letters,* vol. 32, no. 21, pp. 3203-3205, 2007.

[28] S. Wang *et al.*, "A broadband achromatic metalens in the visible," *Nature Nanotechnology,* vol. 13, no. 3, pp. 227-232, 2018.

[29] W. T. Chen *et al.*, "A broadband achromatic metalens for focusing and imaging in the visible," *Nature Nanotechnology,* vol. 13, no. 3, pp. 220-226, 2018.

[30] F. Qin *et al.*, "Hybrid bilayer plasmonic metasurface efficiently manipulates visible light," *Science Advances,* vol. 2, no. 1, p. e1501168, 2016.

[31] K. E. Chong *et al.*, "Polarization-independent silicon metadevices for efficient optical wavefront control," *Nano Letters,* vol. 15, no. 8, pp. 5369-5374, 2015.

[32] Y. Zhou, W. Wu, R. Chen, W. Chen, R. Chen, and Y. Ma, "Analog optical spatial differentiators based on dielectric metasurfaces," *Advanced Optical Materials,* vol. 8, no. 4, p. 1901523, 2020.

[33] J. B. Mueller, N. A. Rubin, R. C. Devlin, B. Groever, and F. Capasso, "Metasurface polarization optics: independent phase control of arbitrary orthogonal states of polarization," *Physical Review Letters,* vol. 118, no. 11, p. 113901, 2017.

[34] O. Yavas, M. Svedendahl, P. Dobosz, V. Sanz, and R. Quidant, "On-a-chip biosensing based on all-dielectric nanoresonators," *Nano Letters,* vol. 17, no. 7, pp. 4421-4426, 2017.

[35] D. Zhang *et al.*, "Nanoscale beam splitters based on gradient metasurfaces," *Optics Letters,* vol. 43, no. 2, pp. 267-270, 2018.

[36] J. Li *et al.*, "Efficient polarization beam splitter based on all-dielectric metasurface in visible region," *Nanoscale Research Letters,* vol. 14, no. 1, pp. 1-7, 2019.

[37] X. Wang, Z. Nie, Y. Liang, J. Wang, T. Li, and B. Jia, "Recent advances on optical vortex generation," *Nanophotonics,* vol. 7, no. 9, pp. 1533-1556, 2018.

[38] H. Kwon, D. Sounas, A. Cordaro, A. Polman, and A. Alù, "Nonlocal metasurfaces for optical signal processing," *Physical Review Letters,* vol. 121, no. 17, p. 173004, 2018.

[39] A. Arbabi, Y. Horie, M. Bagheri, and A. Faraon, "Dielectric metasurfaces for complete control of phase and polarization with subwavelength spatial resolution and high transmission," *Nature Nanotechnology,* vol. 10, no. 11, pp. 937-943, 2015.

[40] G. Y. Lee, J. Sung, and B. Lee, "Recent advances in metasurface hologram technologies," *ETRI Journal,* vol. 41, no. 1, pp. 10-22, 2019.

[41] A. Tittl *et al.*, "Imaging-based molecular barcoding with pixelated dielectric metasurfaces," *Science,* vol. 360, no. 6393, pp. 1105-1109, 2018.

[42] H. Altug, S.-H. Oh, S. A. Maier, and J. Homola, "Advances and applications of nanophotonic biosensors," *Nature Nanotechnology,* vol. 17, no. 1, pp. 5-16, 2022.

[43] M. Inoue, A. Khanikaev, and A. Baryshev, "Nano-magnetophotonics," in *Nanoscale Magnetic Materials and Applications*: Springer, 2009, pp. 627-659.

[44] V. M. Shalaev, "Optical negative-index metamaterials," *Nature Photonics,* vol. 1, no. 1, pp. 41-48, 2007.

[45] R. Maas, J. Parsons, N. Engheta, and A. Polman, "Experimental realization of an epsilon-near-zero metamaterial at visible wavelengths," *Nature Photonics,* vol. 7, no. 11, pp. 907-912, 2013.

[46] A. Poddubny, I. Iorsh, P. Belov, and Y. Kivshar, "Hyperbolic metamaterials," *Nature Photonics,* vol. 7, no. 12, pp. 948-957, 2013.

[47] M. Noginov, M. Lapine, V. Podolskiy, and Y. Kivshar, "Focus issue: hyperbolic metamaterials," *Optics Express,* vol. 21, no. 12, pp. 14895-14897, 2013.

[48] A. Kuzyk *et al.*, "DNA-based self-assembly of chiral plasmonic nanostructures with tailored optical response," *Nature,* vol. 483, no. 7389, pp. 311-314, 2012.

[49] A. Boltasseva and H. A. Atwater, "Low-loss plasmonic metamaterials," *Science,* vol. 331, no. 6015, pp. 290-291, 2011.

[50] G. V. Naik, V. M. Shalaev, and A. Boltasseva, "Alternative plasmonic materials: beyond gold and silver," *Advanced Materials,* vol. 25, no. 24, pp. 3264-3294, 2013.

[51] J. Homola, "Present and future of surface plasmon resonance biosensors," *Analytical and Bioanalytical Chemistry,* vol. 377, no. 3, pp. 528-539, 2003.

[52] I. Khan, "Optical fiber based microwaves sensor using surface plasmon resonance," in *2012 International Conference on Informatics, Electronics & Vision (ICIEV)*, 2012, pp. 310-315: IEEE.

[53] A. K. Sharma, R. Jha, and B. Gupta, "Fiber-optic sensors based on surface plasmon resonance: a comprehensive review," *IEEE Sensors Journal*, vol. 7, no. 8, pp. 1118-1129, 2007.

[54] A. I. Kuznetsov, A. E. Miroshnichenko, Y. H. Fu, J. Zhang, and B. Luk'yanchuk, "Magnetic light," *Scientific Reports*, vol. 2, no. 1, p. 492, 2012.

[55] G. Mie, "Beiträge zur Optik trüber Medien, speziell kolloidaler Metallösungen," *Annalen der Physik*, vol. 330, no. 3, pp. 377-445, 1908.

[56] J. Tian, Q. Li, Y. Yang, and M. Qiu, "Tailoring unidirectional angular radiation through multipolar interference in a single-element subwavelength all-dielectric stair-like nanoantenna," *Nanoscale*, vol. 8, no. 7, pp. 4047-4053, 2016.

[57] C. Pfeiffer and A. Grbic, "Metamaterial Huygens' surfaces: tailoring wave fronts with reflectionless sheets," *Physical Review Letters*, vol. 110, no. 19, p. 197401, 2013.

[58] F. Monticone, N. M. Estakhri, and A. Alu, "Full control of nanoscale optical transmission with a composite metascreen," *Physical Review Letters*, vol. 110, no. 20, p. 203903, 2013.

[59] C. Pfeiffer, N. K. Emani, A. M. Shaltout, A. Boltasseva, V. M. Shalaev, and A. Grbic, "Efficient light bending with isotropic metamaterial Huygens' surfaces," *Nano Letters*, vol. 14, no. 5, pp. 2491-2497, 2014.

[60] M. Decker *et al.*, "High‐efficiency dielectric Huygens' surfaces," *Advanced Optical Materials*, vol. 3, no. 6, pp. 813-820, 2015.

[61] A. Howes, W. Wang, I. Kravchenko, and J. Valentine, "Dynamic transmission control based on all-dielectric Huygens metasurfaces," *Optica*, vol. 5, no. 7, pp. 787-792, 2018.

[62] C. Huygens, "Traité de la Lumière. Pieter van der Aa, Leyden," 1690.

[63] A. E. H. Love, "The integration of the equations of propagation of electric waves," *Philosophical Transactions of the Royal Society of London. Series A*, vol. 197, no. 287-299, pp. 1-45, 1901.

[64] M. Kerker, D.-S. Wang, and C. Giles, "Electromagnetic scattering by magnetic spheres," *JOSA*, vol. 73, no. 6, pp. 765-767, 1983.

[65] V. E. Babicheva and A. B. Evlyukhin, "Resonant lattice Kerker effect in metasurfaces with electric and magnetic optical responses," *Laser & Photonics Reviews*, vol. 11, no. 6, p. 1700132, 2017.

[66] X. Zhang and A. L. Bradley, "Wide-angle invisible dielectric metasurface driven by transverse Kerker scattering," *Physical Review B*, vol. 103, no. 19, p. 195419, 2021.

[67] A. Miroshnichenko, "Fano Resonances in Light Scattering by Finite Obstacles," in *Fano Resonances in Optics and Microwaves*: Springer, 2018, pp. 473-495.

[68] I. Staude *et al.*, "Tailoring directional scattering through magnetic and electric resonances in subwavelength silicon nanodisks," *ACS Nano*, vol. 7, no. 9, pp. 7824-7832, 2013.

[69] R. A. Aoni *et al.*, "High-efficiency visible light manipulation using dielectric metasurfaces," *Scientific Reports,* vol. 9, no. 1, pp. 1-9, 2019.

[70] E. Hasman, V. Kleiner, G. Biener, and A. Niv, "Polarization dependent focusing lens by use of quantized Pancharatnam–Berry phase diffractive optics," *Applied Physics Letters,* vol. 82, no. 3, pp. 328-330, 2003.

[71] G. J. Swanson, "Binary optics technology: the theory and design of multi-level diffractive optical elements," Massachusetts Inst. of Tech Lexington Lincoln Lab1989.

[72] V. A. Soifer, V. Kotlar, and L. Doskolovich, *Iteractive Methods For Diffractive Optical Elements Computation*. CRC Press, 2014.

[73] H. Liang *et al.*, "High performance metalenses: numerical aperture, aberrations, chromaticity, and trade-offs," *Optica,* vol. 6, no. 12, pp. 1461-1470, 2019.

[74] R. A. Aoni *et al.*, "Resonant Dielectric Metagratings for Response Intensified Optical Sensing," *Advanced Functional Materials,* p. 2103143, 2021.

[75] P. Lalanne, S. Astilean, P. Chavel, E. Cambril, and H. Launois, "Blazed binary subwavelength gratings with efficiencies larger than those of conventional échelette gratings," *Optics Letters,* vol. 23, no. 14, pp. 1081-1083, 1998.

[76] P. Lalanne, S. Astilean, P. Chavel, E. Cambril, and H. Launois, "Design and fabrication of blazed binary diffractive elements with sampling periods smaller than the structural cutoff," *JOSA A,* vol. 16, no. 5, pp. 1143-1156, 1999.

[77] Y. Akahane, T. Asano, B.-S. Song, and S. Noda, "High-Q photonic nanocavity in a two-dimensional photonic crystal," *Nature,* vol. 425, no. 6961, pp. 944-947, 2003.

[78] X. Ding *et al.*, "Ultrathin Pancharatnam‐Berry metasurface with maximal cross‐polarization efficiency," *Advanced Materials,* vol. 27, no. 7, pp. 1195-1200, 2015.

[79] M. Liu *et al.*, "Deeply subwavelength metasurface resonators for terahertz wavefront manipulation," *Advanced Optical Materials,* vol. 7, no. 21, p. 1900736, 2019.

[80] W. T. Chen, A. Y. Zhu, M. Khorasaninejad, Z. Shi, V. Sanjeev, and F. Capasso, "Immersion meta-lenses at visible wavelengths for nanoscale imaging," *Nano Letters,* vol. 17, no. 5, pp. 3188-3194, 2017.

[81] A. E. Minovich, A. E. Miroshnichenko, A. Y. Bykov, T. V. Murzina, D. N. Neshev, and Y. S. Kivshar, "Functional and nonlinear optical metasurfaces," *Laser & Photonics Reviews,* vol. 9, no. 2, pp. 195-213, 2015.

[82] A. I. Kuznetsov, A. E. Miroshnichenko, M. L. Brongersma, Y. S. Kivshar, and B. Luk'yanchuk, "Optically resonant dielectric nanostructures," *Science,* vol. 354, no. 6314, 2016.

[83] G. Yoon, D. Lee, K. T. Nam, and J. Rho, "Geometric metasurface enabling polarization independent beam splitting," *Scientific Reports,* vol. 8, no. 1, pp. 1-8, 2018.

[84] C. U. Hail, D. Poulikakos, and H. Eghlidi, "High‐Efficiency, Extreme‐Numerical‐Aperture Metasurfaces Based on Partial Control of the Phase of Light," *Advanced Optical Materials,* vol. 6, no. 22, p. 1800852, 2018.

[85] J. Park *et al.*, "All-solid-state spatial light modulator with independent phase and amplitude control for three-dimensional LiDAR applications," *Nature Nanotechnology,* vol. 16, no. 1, pp. 69-76, 2021.

[86] S. Colburn *et al.*, "Broadband transparent and CMOS-compatible flat optics with silicon nitride metasurfaces," *Optical Materials Express,* vol. 8, no. 8, pp. 2330-2344, 2018.

[87] D. Lin *et al.*, "Polarization-independent metasurface lens employing the Pancharatnam-Berry phase," *Optics Express,* vol. 26, no. 19, pp. 24835-24842, 2018.

[88] D. Lin, P. Fan, E. Hasman, and M. L. Brongersma, "Dielectric gradient metasurface optical elements," *Science,* vol. 345, no. 6194, pp. 298-302, 2014.

[89] P. Lalanne and P. Chavel, "Metalenses at visible wavelengths: past, present, perspectives," *Laser & Photonics Reviews,* vol. 11, no. 3, p. 1600295, 2017.

[90] P. Kepič *et al.*, "Optically Tunable Mie Resonance VO2 Nanoantennas for Metasurfaces in the Visible," *ACS Photonics,* vol. 8, no. 4, pp. 1048-1057, 2021.

[91] A. J. Ollanik, J. A. Smith, M. J. Belue, and M. D. Escarra, "High-Efficiency All-Dielectric Huygens Metasurfaces from the Ultraviolet to the Infrared," *ACS Photonics,* vol. 5, no. 4, pp. 1351-1358, 2018.

[92] Z. Zhou *et al.*, "Efficient silicon metasurfaces for visible light," *ACS Photonics,* vol. 4, no. 3, pp. 544-551, 2017.

[93] M. I. Shalaev, J. Sun, A. Tsukernik, A. Pandey, K. Nikolskiy, and N. M. Litchinitser, "High-efficiency all-dielectric metasurfaces for ultracompact beam manipulation in transmission mode," *Nano Letters,* vol. 15, no. 9, pp. 6261-6266, 2015.

[94] A. Forouzmand and H. Mosallaei, "All‐Dielectric C‐Shaped Nanoantennas for Light Manipulation: Tailoring Both Magnetic and Electric Resonances to the Desire," *Advanced Optical Materials,* vol. 5, no. 14, p. 1700147, 2017.

[95] J. Cheng, D. Ansari-Oghol-Beig, and H. Mosallaei, "Wave manipulation with designer dielectric metasurfaces," *Optics Letters,* vol. 39, no. 21, pp. 6285-6288, 2014.

[96] L. Zhang *et al.*, "Ultra-thin high-efficiency mid-infrared transmissive Huygens meta-optics," *Nature Communications,* vol. 9, no. 1, p. 1481, 2018.

[97] A. Komar *et al.*, "Dynamic beam switching by liquid crystal tunable dielectric metasurfaces," *ACS Photonics,* vol. 5, no. 5, pp. 1742-1748, 2018.

[98] D. Sell, J. Yang, S. Doshay, R. Yang, and J. A. Fan, "Large-angle, multifunctional metagratings based on freeform multimode geometries," *Nano Letters,* vol. 17, no. 6, pp. 3752-3757, 2017.

[99] A. Forouzmand and H. Mosallaei, "Dynamic beam control via Mie-resonance based phase-change metasurface: a theoretical investigation," *Optics Express,* vol. 26, no. 14, pp. 17948-17963, 2018.

[100] M. Kim, J. Jeong, J. K. Poon, and G. V. Eleftheriades, "Vanadium-dioxide-assisted digital optical metasurfaces for dynamic wavefront engineering," *JOSA B,* vol. 33, no. 5, pp. 980-988, 2016.

[101] J. Cheng, S. Inampudi, and H. Mosallaei, "Optimization-based dielectric metasurfaces for angle-selective multifunctional beam deflection," *Scientific Reports,* vol. 7, no. 1, p. 12228, 2017.

[102] J. P. Hugonin and P. Lalanne, "Reticolo software for grating analysis, Institute of Optics Graduates School, Orsay, France," *https://www.lp2n.institutoptique.fr*, 2005.

[103] M. Moharam, E. B. Grann, D. A. Pommet, and T. Gaylord, "Formulation for stable and efficient implementation of the rigorous coupled-wave analysis of binary gratings," *JOSA A,* vol. 12, no. 5, pp. 1068-1076, 1995.

[104] R. Liu, T. J. Cui, D. Huang, B. Zhao, and D. R. Smith, "Description and explanation of electromagnetic behaviors in artificial metamaterials based on effective medium theory," *Physical Review E,* vol. 76, no. 2, p. 026606, 2007.

[105] D. Smith, D. Vier, T. Koschny, and C. Soukoulis, "Electromagnetic parameter retrieval from inhomogeneous metamaterials," *Physical Review E,* vol. 71, no. 3, p. 036617, 2005.

[106] Y. F. Yu, A. Y. Zhu, R. Paniagua‐Domínguez, Y. H. Fu, B. Luk'yanchuk, and A. I. Kuznetsov, "High‐transmission dielectric metasurface with 2π phase control at visible wavelengths," *Laser & Photonics Reviews,* vol. 9, no. 4, pp. 412-418, 2015.

[107] L. Yang *et al.,* "High-efficiency all-dielectric transmission metasurface for linearly polarized light in the visible region," *Photonics Research,* vol. 6, no. 6, pp. 517-524, 2018.

[108] L. Zhang *et al.,* "Ultra-thin high-efficiency mid-infrared transmissive Huygens meta-optics," *Nature Communications,* vol. 9, no. 1, pp. 1-9, 2018.

[109] D. Sell, J. Yang, S. Doshay, and J. A. Fan, "Periodic dielectric metasurfaces with high‐efficiency, multiwavelength functionalities," *Advanced Optical Materials,* vol. 5, no. 23, p. 1700645, 2017.

[110] D. M. Pozar, S. D. Targonski, and H. Syrigos, "Design of millimeter wave microstrip reflectarrays," *IEEE Transactions on Antennas and Propagation,* vol. 45, no. 2, pp. 287-296, 1997.

[111] A. Pors, M. G. Nielsen, R. L. Eriksen, and S. I. Bozhevolnyi, "Broadband focusing flat mirrors based on plasmonic gradient metasurfaces," *Nano Letters,* vol. 13, no. 2, pp. 829-834, 2013.

[112] S. Yu, L. Li, G. Shi, C. Zhu, and Y. Shi, "Generating multiple orbital angular momentum vortex beams using a metasurface in radio frequency domain," *Applied Physics Letters,* vol. 108, no. 24, p. 241901, 2016.

[113] C. Qu *et al.,* "Tailor the functionalities of metasurfaces based on a complete phase diagram," *Physical Review Letters,* vol. 115, no. 23, p. 235503, 2015.

[114] Z. Miao *et al.,* "Widely tunable terahertz phase modulation with gate-controlled graphene metasurfaces," *Physical Review X,* vol. 5, no. 4, p. 041027, 2015.

[115] X. Wang *et al.,* "Extreme asymmetry in metasurfaces via evanescent fields engineering: Angular-asymmetric absorption," *Physical Review Letters,* vol. 121, no. 25, p. 256802, 2018.

[116] L. Cong, P. Pitchappa, C. Lee, and R. Singh, "Active phase transition via loss engineering in a terahertz MEMS metamaterial," *Advanced Materials,* vol. 29, no. 26, p. 1700733, 2017.

[117] G. Marrocco, "Gain-optimized self-resonant meander line antennas for RFID applications," *IEEE Antennas and Wireless Propagation Letters,* vol. 2, pp. 302-305, 2003.

[118] J. Baena, L. Jelinek, R. Marques, and J. Zehentner, "Electrically small isotropic three-dimensional magnetic resonators for metamaterial design," *Applied Physics Letters,* vol. 88, no. 13, p. 134108, 2006.

[119] P. Jin and R. W. Ziolkowski, "Metamaterial-inspired, electrically small Huygens sources," *IEEE Antennas and Wireless Propagation Letters,* vol. 9, pp. 501-505, 2010.

[120] T. Niu *et al.*, "Experimental demonstration of reflectarray antennas at terahertz frequencies," *Optics Express,* vol. 21, no. 3, pp. 2875-2889, 2013.

[121] I. Al-Naib and W. Withayachumnankul, "Recent progress in terahertz metasurfaces," *Journal of Infrared, Millimeter, and Terahertz Waves,* vol. 38, no. 9, pp. 1067-1084, 2017.

[122] A. Pors, E. Moreno, L. Martin-Moreno, J. B. Pendry, and F. J. Garcia-Vidal, "Localized spoof plasmons arise while texturing closed surfaces," *Physical Review Letters,* vol. 108, no. 22, p. 223905, 2012.

[123] P. A. Huidobro *et al.*, "Magnetic localized surface plasmons," *Physical Review X,* vol. 4, no. 2, p. 021003, 2014.

[124] Z. Gao, L. Wu, F. Gao, Y. Luo, and B. Zhang, "Spoof plasmonics: from metamaterial concept to topological description," *Advanced Materials,* vol. 30, no. 31, p. 1706683, 2018.

[125] P. Kolb, T. Salter, J. McGee, H. Drew, and W. Padilla, "Extreme subwavelength electric GHz metamaterials," *Journal of Applied Physics,* vol. 110, no. 5, p. 054906, 2011.

[126] W.-C. Chen, C. M. Bingham, K. M. Mak, N. W. Caira, and W. J. Padilla, "Extremely subwavelength planar magnetic metamaterials," *Physical Review B,* vol. 85, no. 20, p. 201104, 2012.

[127] H. Wong, K.-M. Luk, C. H. Chan, Q. Xue, K. K. So, and H. W. Lai, "Small antennas in wireless communications," *Proceedings of the IEEE,* vol. 100, no. 7, pp. 2109-2121, 2012.

[128] G. D. Alley, "Interdigital capacitors and their application to lumped-element microwave integrated circuits," *IEEE Transactions on Microwave Theory and Techniques,* vol. 18, no. 12, pp. 1028-1033, 1970.

[129] A. Lai, T. Itoh, and C. Caloz, "Composite right/left-handed transmission line metamaterials," *IEEE Microwave Magazine,* vol. 5, no. 3, pp. 34-50, 2004.

[130] W. Withayachumnankul, C. Fumeaux, and D. Abbott, "Compact electric-LC resonators for metamaterials," *Optics Express,* vol. 18, no. 25, pp. 25912-25921, 2010.

[131] A. A. Rifat, M. Rahmani, L. Xu, and A. E. Miroshnichenko, "Hybrid metasurface based tunable near-perfect absorber and plasmonic sensor," *Materials,* vol. 11, no. 7, p. 1091, 2018.

[132] M. Soler, A. Belushkin, A. Cavallini, C. Kebbi-Beghdadi, G. Greub, and H. Altug, "Multiplexed nanoplasmonic biosensor for one-step simultaneous detection of Chlamydia trachomatis and Neisseria gonorrhoeae in urine," *Biosensors and Bioelectronics,* vol. 94, pp. 560-567, 2017.

[133] N. Bontempi *et al.*, "Highly sensitive biosensors based on all-dielectric nanoresonators," *Nanoscale,* vol. 9, no. 15, pp. 4972-4980, 2017.

[134] C. Wu *et al.*, "Fano-resonant asymmetric metamaterials for ultrasensitive spectroscopy and identification of molecular monolayers," *Nature Materials,* vol. 11, no. 1, pp. 69-75, 2012.

[135] S. M. Borisov and O. S. Wolfbeis, "Optical biosensors," *Chemical Reviews,* vol. 108, no. 2, pp. 423-461, 2008.

[136] S. Zhang *et al.*, "Metasurfaces for biomedical applications: imaging and sensing from a nanophotonics perspective," *Nanophotonics,* vol. 10, no. 1, pp. 259-293, 2021.

[137] A. K. Yetisen, M. S. Akram, and C. R. Lowe, "Paper-based microfluidic point-of-care diagnostic devices," *Lab on a Chip,* vol. 13, no. 12, pp. 2210-2251, 2013.

[138] M. König *et al.*, "Unveiling the correlation between nanometer-thick molecular monolayer sensitivity and near-field enhancement and localization in coupled plasmonic oligomers," *ACS Nano,* vol. 8, no. 9, pp. 9188-9198, 2014.

[139] Z. Fusco *et al.*, "Photonic Fractal Metamaterials: A Metal‐Semiconductor Platform with Enhanced Volatile‐Compound Sensing Performance," *Advanced Materials,* vol. 32, no. 50, p. 2002471, 2020.

[140] A. A. Rifat *et al.*, "Photonic crystal fiber based plasmonic sensors," *Sensors and Actuators B: Chemical,* vol. 243, pp. 311-325, 2017.

[141] A. P. Turner, "Biosensors: sense and sensibility," *Chemical Society Reviews,* vol. 42, no. 8, pp. 3184-3196, 2013.

[142] H. Im *et al.*, "Label-free detection and molecular profiling of exosomes with a nano-plasmonic sensor," *Nature Biotechnology,* vol. 32, no. 5, pp. 490-495, 2014.

[143] D. Barshilia, L.-K. Chau, and G.-E. Chang, "Low-cost planar waveguide-based optofluidic sensor for real-time refractive index sensing," *Optics Express,* vol. 28, no. 19, pp. 27337-27345, 2020.

[144] W. Bogaerts *et al.*, "Silicon microring resonators," *Laser & Photonics Reviews,* vol. 6, no. 1, pp. 47-73, 2012.

[145] M. Rosenberg, B. W. Laursen, C. G. Frankær, and T. J. Sørensen, "A fluorescence intensity ratiometric fiber optics–based chemical sensor for monitoring pH," *Advanced Materials Technologies,* vol. 3, no. 12, p. 1800205, 2018.

[146] F. A. A. Nugroho, D. Albinsson, T. J. Antosiewicz, and C. Langhammer, "Plasmonic metasurface for spatially resolved optical sensing in three dimensions," *ACS Nano,* vol. 14, no. 2, pp. 2345-2353, 2020.

[147] N. Liu, M. Mesch, T. Weiss, M. Hentschel, and H. Giessen, "Infrared perfect absorber and its application as plasmonic sensor," *Nano Letters,* vol. 10, no. 7, pp. 2342-2348, 2010.

[148] M. Rahmani *et al.*, "Reversible thermal tuning of all‐dielectric metasurfaces," *Advanced Functional Materials,* vol. 27, no. 31, p. 1700580, 2017.

[149] R. Ahmed *et al.*, "Tunable fano‐resonant metasurfaces on a disposable plastic‐template for multimodal and multiplex biosensing," *Advanced Materials,* vol. 32, no. 19, p. 1907160, 2020.

[150] A. Leitis *et al.*, "Angle-multiplexed all-dielectric metasurfaces for broadband molecular fingerprint retrieval," *Science Advances,* 2019.

[151] F. Yesilkoy *et al.*, "Ultrasensitive hyperspectral imaging and biodetection enabled by dielectric metasurfaces," *Nature Photonics,* vol. 13, no. 6, pp. 390-396, 2019.

[152] C. Lv, Z. Jia, Y. Liu, J. Mo, P. Li, and X. Lv, "Angle-resolved diffraction grating biosensor based on porous silicon," *Journal of Applied Physics,* vol. 119, no. 9, p. 094502, 2016.

[153] F. Purr, M. Bassu, R. Lowe, B. Thürmann, A. Dietzel, and T. Burg, "Asymmetric nanofluidic grating detector for differential refractive index measurement and biosensing," *Lab on a Chip,* vol. 17, no. 24, pp. 4265-4272, 2017.

[154] N. L. Kazanskiy, S. N. Khonina, and M. A. Butt, "Subwavelength grating double slot waveguide racetrack ring resonator for refractive index sensing application," *Sensors,* vol. 20, no. 12, p. 3416, 2020.

[155] X. Tu, Y. Luo, T. Huang, J. Gan, and C. Song, "Optofluidic refractive index sensor based on asymmetric diffraction," *Optics Express,* vol. 27, no. 13, pp. 17809-17818, 2019.

[156] N. Kumawat, P. Pal, and M. Varma, "Diffractive optical analysis for refractive index sensing using transparent phase gratings," *Scientific Reports,* vol. 5, no. 1, pp. 1-10, 2015.

[157] S. Calixto, N. C. Bruce, and M. Rosete-Aguilar, "Diffraction grating-based sensing optofluidic device for measuring the refractive index of liquids," *Optics Express,* vol. 24, no. 1, pp. 180-190, 2016.

[158] Y. Ra'di, D. L. Sounas, and A. Alù, "Metagratings: Beyond the limits of graded metasurfaces for wave front control," *Physical Review Letters,* vol. 119, no. 6, p. 067404, 2017.

[159] S. C. Lee, K. J. Son, C. H. Han, J. Y. Jung, and S. C. Park, "Impact of comorbid asthma on severity of coronavirus disease (COVID-19)," *Scientific Reports,* vol. 10, no. 1, pp. 1-9, 2020.

[160] E. Khaidarov *et al.*, "Asymmetric nanoantennas for ultrahigh angle broadband visible light bending," *Nano Letters,* vol. 17, no. 10, pp. 6267-6272, 2017.

[161] A. Patri, S. Kena-Cohen, and C. Caloz, "Large-Angle, Broadband, and Multifunctional Directive Waveguide Scatterer Gratings," *ACS Photonics,* vol. 6, no. 12, pp. 3298-3305, 2019.

[162] C. Zhan, B.-W. Liu, Z.-Q. Tian, and B. Ren, "Determining the interfacial refractive index via ultrasensitive plasmonic sensors," *Journal of the American Chemical Society,* vol. 142, no. 25, pp. 10905-10909, 2020.

[163] F. Uleman, V. Neder, A. Cordaro, A. Alù, and A. Polman, "Resonant metagratings for spectral and angular control of light for colored rooftop photovoltaics," *ACS Applied Energy Materials,* vol. 3, no. 4, pp. 3150-3156, 2020.

[164] J. Landry, Y. Ke, G.-L. Yu, and X. Zhu, "Measuring affinity constants of 1450 monoclonal antibodies to peptide targets with a microarray-based label-free assay platform," *Journal of Immunological Methods,* vol. 417, pp. 86-96, 2015.

[165] A. Komar, R. A. Aoni, L. Xu, M. Rahmani, A. E. Miroshnichenko, and D. N. Neshev, "Edge Detection with Mie-Resonant Dielectric Metasurfaces," *ACS Photonics,* vol. 8, no. 3, pp. 864-871, 2021.

[166] S. AbdollahRamezani, K. Arik, A. Khavasi, and Z. Kavehvash, "Analog computing using graphene-based metalines," *Optics Letters,* vol. 40, no. 22, pp. 5239-5242, 2015.

[167] T. Zhu *et al.*, "Plasmonic computing of spatial differentiation," *Nature Communications,* vol. 8, no. 1, pp. 1-6, 2017.

[168] L. Wesemann *et al.*, "Selective near-perfect absorbing mirror as a spatial frequency filter for optical image processing," *APL Photonics,* vol. 4, no. 10, p. 100801, 2019.

[169] A. Cordaro, H. Kwon, D. Sounas, A. F. Koenderink, A. Alù, and A. Polman, "High-index dielectric metasurfaces performing mathematical operations," *Nano Letters,* vol. 19, no. 12, pp. 8418-8423, 2019.

[170] Z. Dong, J. Si, X. Yu, and X. Deng, "Optical spatial differentiator based on subwavelength high-contrast gratings," *Applied Physics Letters,* vol. 112, no. 18, p. 181102, 2018.

[171] L. Wan *et al.*, "Optical analog computing of spatial differentiation and edge detection with dielectric metasurfaces," *Optics Letters,* vol. 45, no. 7, pp. 2070-2073, 2020.

[172] J. Zhou *et al.*, "Optical edge detection based on high-efficiency dielectric metasurface," *Proceedings of the National Academy of Sciences,* vol. 116, no. 23, pp. 11137-11140, 2019.

[173] S. Abdollahramezani, O. Hemmatyar, and A. Adibi, "Meta-optics for spatial optical analog computing," *Nanophotonics,* vol. 9, no. 13, pp. 4075-4095, 2020.

[174] C. Guo, M. Xiao, M. Minkov, Y. Shi, and S. Fan, "Photonic crystal slab Laplace operator for image differentiation," *Optica,* vol. 5, no. 3, pp. 251-256, 2018.

[175] T. Badloe, J. Lee, J. Seong, and J. Rho, "Tunable Metasurfaces: The Path to Fully Active Nanophotonics," *Advanced Photonics Research,* vol. 2, no. 9, p. 2000205, 2021.

[176] F. Soto, J. Wang, R. Ahmed, and U. Demirci, "Medical micro/nanorobots in precision medicine," *Advanced Science,* vol. 7, no. 21, p. 2002203, 2020.

[177] D. Andrén, D. G. Baranov, S. Jones, G. Volpe, R. Verre, and M. Käll, "Microscopic metavehicles powered and steered by embedded optical metasurfaces," *Nature Nanotechnology,* vol. 16, no. 9, pp. 970-974, 2021.

[178] X. Wang *et al.*, "Intracellular manipulation and measurement with multipole magnetic tweezers," *Science Robotics,* vol. 4, no. 28, 2019.

[179] E. Engay, D. Huo, R. Malureanu, A.-I. Bunea, and A. Lavrinenko, "Polarization-Dependent All-Dielectric Metasurface for Single-Shot Quantitative Phase Imaging," *Nano Letters,* vol. 21, no. 9, pp. 3820-3826, 2021.

[180] J. Zhou *et al.*, "Two-dimensional optical spatial differentiation and high-contrast imaging," *National Science Review,* vol. 8, no. 6, p. nwaa176, 2021.

Experimental Refractive Index

I have measured the dielectric constant of a-Si using the ellipsometer and provided the refractive index data as a function of wavelength in Figure A.1.

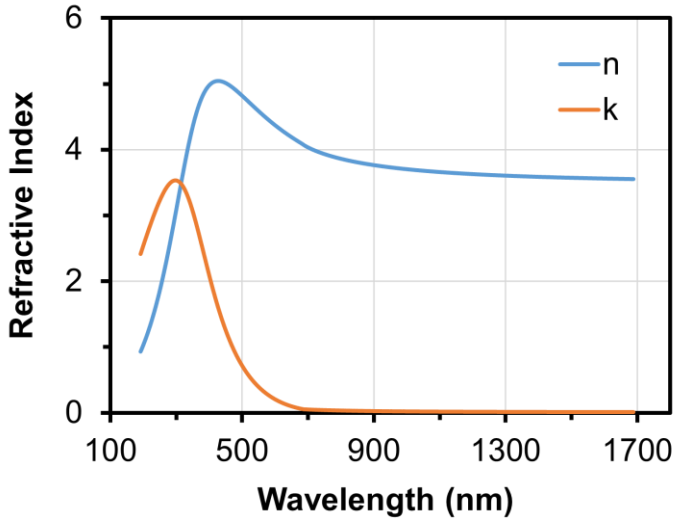

Figure A.1 Experimentally measured dielectric constants of a-Si.

I have also provided the experimentally measured refractive index data in Table A.1 for better reproducibility.

Table A.1 Experimentally measured dielectric constants of a-Si.

Wavelength (nm)	n	k	Wavelength (nm)	n	k
191.890457	0.932238	2.41191	755.107971	3.923263	0.037477
193.474548	0.950861	2.436371	756.68512	3.920745	0.03724
195.058731	0.969801	2.460763	758.262146	3.918254	0.037005
196.642975	0.989063	2.485083	759.839111	3.915788	0.036773
198.22731	1.008652	2.509328	761.415894	3.913347	0.036544
199.811707	1.028572	2.533494	762.992615	3.91093	0.036317
201.396194	1.048828	2.557578	764.569214	3.908538	0.036092
202.980759	1.069424	2.581574	766.14563	3.90617	0.03587
204.565399	1.090364	2.605479	767.722046	3.903825	0.03565
206.150101	1.111654	2.629288	769.298218	3.901504	0.035432
207.734894	1.133298	2.652997	770.874329	3.899204	0.035217
209.319748	1.1553	2.6766	772.450256	3.896927	0.035004
210.904694	1.177666	2.700091	774.026123	3.894672	0.034793

212.489716	1.200399	2.723467	775.601807	3.892439	0.034584
214.074799	1.223504	2.746719	777.177368	3.890226	0.034378
215.659958	1.246986	2.769842	778.752869	3.888035	0.034173
217.245193	1.270848	2.79283	780.328186	3.885864	0.033971
218.830475	1.295096	2.815675	781.903442	3.883713	0.03377
220.415848	1.319735	2.838371	783.478455	3.881582	0.033572
222.001297	1.344767	2.86091	785.053406	3.879471	0.033376
223.586792	1.370198	2.883285	786.628235	3.877379	0.033182
225.172394	1.396031	2.905488	788.202942	3.875307	0.032989
226.758026	1.422271	2.927509	789.777466	3.873253	0.032799
228.34375	1.448922	2.949341	791.351929	3.871217	0.032611
229.92952	1.475986	2.970973	792.926208	3.8692	0.032424
231.515381	1.503469	2.992399	794.500366	3.867201	0.03224
233.101288	1.531373	3.013605	796.074402	3.865219	0.032057
234.687286	1.559701	3.034585	797.648315	3.863255	0.031876
236.273315	1.588457	3.055325	799.222046	3.861308	0.031697
237.859421	1.617644	3.075817	800.795715	3.859378	0.031519
239.445602	1.647264	3.096048	802.369202	3.857465	0.031344
241.03183	1.67732	3.116007	803.942566	3.855568	0.03117
242.618134	1.707814	3.135682	805.515747	3.853688	0.030997
244.204514	1.738747	3.155061	807.088867	3.851824	0.030827
245.790939	1.770121	3.174131	808.661804	3.849975	0.030658
247.377411	1.801937	3.19288	810.234619	3.848142	0.030491
248.963959	1.834196	3.211293	811.807312	3.846325	0.030325
250.550583	1.866899	3.229358	813.379822	3.844523	0.030161
252.137238	1.900044	3.247059	814.952271	3.842736	0.029999
253.723969	1.933633	3.264384	816.524536	3.840964	0.029838
255.310745	1.967663	3.281315	818.096619	3.839206	0.029679
256.897583	2.002134	3.29784	819.668579	3.837463	0.029521
258.484497	2.037043	3.313943	821.240417	3.835735	0.029365
260.071472	2.072389	3.329607	822.812134	3.83402	0.02921
261.658478	2.108167	3.344817	824.383667	3.832319	0.029057
263.245544	2.144373	3.359556	825.955078	3.830633	0.028905
264.832642	2.181005	3.373809	827.526367	3.828959	0.028755
266.41983	2.218056	3.387558	829.097473	3.8273	0.028606
268.00705	2.255522	3.400786	830.668457	3.825653	0.028458
269.59433	2.293394	3.413476	832.239258	3.82402	0.028312
271.181702	2.331667	3.425613	833.809937	3.822399	0.028167
272.769073	2.370332	3.437176	835.380493	3.820792	0.028023
274.356506	2.40938	3.448151	836.950867	3.819197	0.027881
275.944	2.448802	3.458518	838.521118	3.817614	0.027741
277.531555	2.488587	3.468261	840.091187	3.816044	0.027601
279.119141	2.528724	3.477363	841.661133	3.814486	0.027463
280.706787	2.569201	3.485805	843.230957	3.81294	0.027326
282.294495	2.610004	3.493572	844.800598	3.811406	0.02719
283.882233	2.651119	3.500645	846.369995	3.809884	0.027056
285.470001	2.692531	3.507008	847.939331	3.808374	0.026922
287.057831	2.734224	3.512645	849.508606	3.806875	0.02679
288.645721	2.776182	3.51754	851.077637	3.805387	0.02666

290.233643	2.818386	3.521677	852.646484	3.803911	0.02653
291.821594	2.860816	3.525042	854.21521	3.802446	0.026401
293.409637	2.903455	3.527618	855.783813	3.800992	0.026274
294.997711	2.946281	3.529392	857.352234	3.799548	0.026148
296.585785	2.989271	3.530352	858.920532	3.798116	0.026023
298.17395	3.032404	3.530484	860.488586	3.796694	0.025899
299.762146	3.075656	3.529776	862.056519	3.795283	0.025776
301.350372	3.119003	3.528218	863.62439	3.793882	0.025654
302.93866	3.16242	3.525799	865.192017	3.792491	0.025534
304.526978	3.205881	3.52251	866.75946	3.791111	0.025414
306.115326	3.249358	3.518344	868.326843	3.78974	0.025296
307.703705	3.292825	3.513293	869.893921	3.78838	0.025178
309.292175	3.336254	3.507351	871.46106	3.78703	0.025062
310.880646	3.379616	3.500514	873.027832	3.785689	0.024946
312.469147	3.422883	3.492779	874.594543	3.784358	0.024832
314.057678	3.466024	3.484144	876.161011	3.783036	0.024718
315.646301	3.509011	3.474608	877.727417	3.781724	0.024606
317.234924	3.551813	3.464171	879.29364	3.780422	0.024494
318.823547	3.594399	3.452836	880.85968	3.779128	0.024384
320.412262	3.63674	3.440607	882.425476	3.777844	0.024274
322.001007	3.678806	3.427488	883.991211	3.776569	0.024166
323.589783	3.720564	3.413486	885.556824	3.775303	0.024058
325.178558	3.761987	3.398609	887.122192	3.774046	0.023951
326.767395	3.803042	3.382867	888.687378	3.772797	0.023845
328.356262	3.843702	3.366269	890.252441	3.771557	0.02374
329.94516	3.883938	3.34883	891.817261	3.770326	0.023636
331.534088	3.923719	3.330562	893.382019	3.769104	0.023533
333.123047	3.963018	3.31148	894.946594	3.767889	0.023431
334.712036	4.001809	3.291601	896.510925	3.766684	0.023329
336.301056	4.040064	3.270944	898.075195	3.765486	0.023229
337.890076	4.077758	3.249527	899.639282	3.764297	0.023129
339.479187	4.114866	3.22737	901.203125	3.763116	0.02303
341.068298	4.151365	3.204495	902.766785	3.761942	0.022932
342.65741	4.187232	3.180924	904.330261	3.760777	0.022834
344.246582	4.222445	3.156682	905.893677	3.75962	0.022738
345.835754	4.256984	3.131792	907.456848	3.758471	0.022642
347.424988	4.290831	3.10628	909.019836	3.757329	0.022547
349.014221	4.323967	3.080171	910.582703	3.756195	0.022453
350.603455	4.356378	3.053494	912.145325	3.755068	0.02236
352.192749	4.388046	3.026274	913.707825	3.753949	0.022267
353.782074	4.41896	2.99854	915.270142	3.752837	0.022175
355.371399	4.449106	2.970321	916.832336	3.751733	0.022084
356.960754	4.478475	2.941644	918.394226	3.750636	0.021994
358.55014	4.507056	2.912539	919.956055	3.749547	0.021904
360.139526	4.534842	2.883035	921.5177	3.748464	0.021815
361.728943	4.561826	2.85316	923.079102	3.747389	0.021727
363.31842	4.588005	2.822944	924.64032	3.74632	0.021639
364.907867	4.613373	2.792416	926.201355	3.745259	0.021553
366.497345	4.637928	2.761604	927.762329	3.744204	0.021467

368.086853	4.66167	2.730537	929.323059	3.743156	0.021381
369.676331	4.684598	2.699243	930.883484	3.742115	0.021296
371.2659	4.706715	2.66775	932.443848	3.741081	0.021212
372.855438	4.728023	2.636084	934.004089	3.740054	0.021129
374.445007	4.748525	2.604274	935.564087	3.739033	0.021046
376.034607	4.768227	2.572344	937.12384	3.738018	0.020964
377.624207	4.787134	2.540321	938.683472	3.73701	0.020883
379.213806	4.805253	2.508229	940.242859	3.736008	0.020802
380.803406	4.822593	2.476093	941.802124	3.735013	0.020721
382.393066	4.839161	2.443935	943.361206	3.734024	0.020642
383.982727	4.854969	2.41178	944.920105	3.733041	0.020563
385.572388	4.870024	2.379648	946.478821	3.732065	0.020485
387.162048	4.88434	2.347561	948.037292	3.731094	0.020407
388.75177	4.897927	2.315538	949.595581	3.73013	0.02033
390.341461	4.910797	2.283601	951.153687	3.729172	0.020253
391.931152	4.922963	2.251766	952.711731	3.728219	0.020177
393.520874	4.934438	2.220052	954.269409	3.727273	0.020102
395.110626	4.945237	2.188474	955.826965	3.726332	0.020027
396.700348	4.955371	2.157051	957.384399	3.725397	0.019953
398.2901	4.964857	2.125797	958.941528	3.724468	0.019879
399.879822	4.973708	2.094725	960.498535	3.723545	0.019806
401.469604	4.981938	2.06385	962.055359	3.722627	0.019733
403.059387	4.989564	2.033183	963.611938	3.721715	0.019661
404.649139	4.9966	2.002738	965.168335	3.720809	0.01959
406.238922	5.003059	1.972526	966.724487	3.719908	0.019519
407.828705	5.008959	1.942555	968.280579	3.719012	0.019449
409.418488	5.014314	1.912837	969.836426	3.718122	0.019379
411.00824	5.019139	1.88338	971.39209	3.717237	0.019309
412.598053	5.023449	1.854191	972.947449	3.716358	0.019241
414.187836	5.027259	1.82528	974.502747	3.715483	0.019172
415.777649	5.030584	1.796651	976.0578	3.714615	0.019104
417.367432	5.033438	1.768313	977.61261	3.713751	0.019037
418.957275	5.035837	1.740269	979.167297	3.712892	0.01897
420.547058	5.037794	1.712526	980.72168	3.712039	0.018904
422.136871	5.039323	1.685087	982.276001	3.71119	0.018838
423.726654	5.04044	1.657958	983.829956	3.710347	0.018773
425.316467	5.041156	1.63114	985.383911	3.709509	0.018708
426.90625	5.041487	1.604638	986.9375	3.708675	0.018643
428.496033	5.041445	1.578453	988.490906	3.707847	0.018579
430.085785	5.041044	1.552588	990.04425	3.707023	0.018516
431.675598	5.040296	1.527043	991.59729	3.706204	0.018453
433.265381	5.039213	1.501821	993.150085	3.70539	0.01839
434.855133	5.037808	1.476923	994.702759	3.70458	0.018328
436.444916	5.036094	1.452348	996.255188	3.703776	0.018267
438.034668	5.034081	1.428097	997.807434	3.702976	0.018205
439.62442	5.031781	1.404171	999.359375	3.70218	0.018145
441.214203	5.029205	1.380566	1011.95813	3.695886	0.017666
442.803894	5.026365	1.357286	1015.335327	3.694247	0.017543
444.393646	5.02327	1.334327	1018.713074	3.692627	0.017421

445.983398	5.019931	1.311688	1022.091431	3.691026	0.017301
447.57309	5.016358	1.289369	1025.470337	3.689444	0.017182
449.162781	5.01256	1.267368	1028.849854	3.68788	0.017066
450.752502	5.008548	1.245682	1032.229736	3.686334	0.016951
452.342194	5.00433	1.22431	1035.610474	3.684806	0.016837
453.931824	4.999916	1.20325	1038.991577	3.683295	0.016726
455.521545	4.995312	1.182499	1042.373291	3.681802	0.016616
457.111176	4.99053	1.162055	1045.755615	3.680326	0.016507
458.700775	4.985575	1.141917	1049.13855	3.678866	0.0164
460.290436	4.980457	1.122079	1052.522095	3.677422	0.016294
461.880035	4.975183	1.102541	1055.906006	3.675995	0.01619
463.469635	4.969759	1.083299	1059.290649	3.674584	0.016088
465.059174	4.964194	1.06435	1062.675903	3.673188	0.015987
466.648743	4.958495	1.045692	1066.061646	3.671808	0.015887
468.238281	4.952667	1.027321	1069.447998	3.670443	0.015788
469.827789	4.946717	1.009234	1072.834717	3.669093	0.015691
471.417328	4.940652	0.991427	1076.22229	3.667758	0.015595
473.006775	4.934478	0.973899	1079.610229	3.666437	0.015501
474.596283	4.9282	0.956644	1082.998901	3.665131	0.015408
476.18573	4.921824	0.939661	1086.388062	3.663838	0.015316
477.775146	4.915357	0.922946	1089.777832	3.66256	0.015225
479.364563	4.908801	0.906496	1093.168213	3.661295	0.015135
480.953949	4.902163	0.890306	1096.55896	3.660043	0.015047
482.543304	4.895448	0.874374	1099.950439	3.658805	0.01496
484.13266	4.88866	0.858696	1103.342529	3.65758	0.014874
485.721985	4.881804	0.84327	1106.735107	3.656368	0.014789
487.311279	4.874885	0.828091	1110.128174	3.655168	0.014705
488.900543	4.867905	0.813157	1113.521973	3.653981	0.014622
490.489807	4.860871	0.798463	1116.91626	3.652807	0.01454
492.07901	4.853785	0.784007	1120.311279	3.651644	0.01446
493.668213	4.84665	0.769785	1123.706665	3.650494	0.01438
495.257416	4.839472	0.755794	1127.102661	3.649355	0.014301
496.846527	4.832253	0.742031	1130.499268	3.648228	0.014224
498.435638	4.824996	0.728492	1133.896362	3.647112	0.014147
500.02475	4.817706	0.715174	1137.294189	3.646008	0.014072
501.613831	4.810384	0.702074	1140.692505	3.644915	0.013997
503.20282	4.803035	0.689189	1144.091309	3.643833	0.013923
504.79184	4.79566	0.676515	1147.490845	3.642761	0.01385
506.380798	4.788263	0.66405	1150.890869	3.641701	0.013778
507.969788	4.780847	0.651789	1154.291382	3.640651	0.013707
509.558685	4.773413	0.639731	1157.692627	3.639611	0.013637
511.147552	4.765964	0.627873	1161.09436	3.638582	0.013567
512.73645	4.758503	0.61621	1164.496582	3.637563	0.013499
514.325256	4.751032	0.60474	1167.899536	3.636554	0.013431
515.914001	4.743554	0.593461	1171.302979	3.635554	0.013364
517.502747	4.736069	0.582369	1174.706909	3.634565	0.013298
519.091431	4.72858	0.571461	1178.111572	3.633585	0.013233
520.680115	4.72109	0.560735	1181.516724	3.632614	0.013169
522.268799	4.7136	0.550187	1184.922485	3.631653	0.013105

523.857361	4.706112	0.539816	1188.328735	3.630701	0.013042
525.445923	4.698627	0.529617	1191.735596	3.629758	0.01298
527.034485	4.691147	0.519589	1195.143066	3.628825	0.012918
528.622986	4.683674	0.509729	1198.551025	3.6279	0.012857
530.211426	4.676209	0.500035	1201.959717	3.626983	0.012797
531.799866	4.668754	0.490503	1205.368896	3.626076	0.012738
533.388245	4.66131	0.481131	1208.778564	3.625177	0.012679
534.976563	4.653878	0.471916	1212.188843	3.624286	0.012621
536.564819	4.64646	0.462857	1215.599731	3.623404	0.012564
538.153137	4.639056	0.45395	1219.011108	3.62253	0.012507
539.741333	4.631669	0.445194	1222.423096	3.621664	0.012451
541.329468	4.624299	0.436585	1225.835693	3.620806	0.012396
542.917603	4.616946	0.428122	1229.248901	3.619956	0.012341
544.505737	4.609613	0.419803	1232.662598	3.619113	0.012287
546.09375	4.6023	0.411624	1236.076904	3.618279	0.012233
547.681763	4.595008	0.403584	1239.491821	3.617452	0.01218
549.269653	4.587738	0.395681	1242.907227	3.616632	0.012128
550.857544	4.580491	0.387912	1246.323242	3.61582	0.012076
552.445435	4.573267	0.380275	1249.739746	3.615016	0.012025
554.033264	4.566068	0.372768	1253.156982	3.614218	0.011975
555.620972	4.558893	0.365389	1256.574585	3.613428	0.011924
557.20874	4.551744	0.358137	1259.99292	3.612645	0.011875
558.796387	4.544622	0.351008	1263.411865	3.611868	0.011826
560.384033	4.537527	0.344002	1266.831299	3.611099	0.011778
561.971558	4.530459	0.337115	1270.251221	3.610336	0.01173
563.559082	4.52342	0.330347	1273.671753	3.609581	0.011682
565.146606	4.516409	0.323696	1277.093018	3.608831	0.011635
566.734009	4.509428	0.317158	1280.514648	3.608089	0.011589
568.32135	4.502475	0.310734	1283.937012	3.607352	0.011543
569.90863	4.495553	0.30442	1287.359863	3.606623	0.011498
571.495911	4.488662	0.298216	1290.783325	3.605899	0.011453
573.08313	4.481802	0.292118	1294.207275	3.605182	0.011408
574.670288	4.474973	0.286127	1297.631836	3.604471	0.011364
576.257324	4.468175	0.28024	1301.056885	3.603766	0.011321
577.84436	4.46141	0.274454	1304.482666	3.603068	0.011278
579.431335	4.454677	0.26877	1307.908936	3.602375	0.011235
581.018311	4.447976	0.263185	1311.335815	3.601688	0.011193
582.605164	4.441308	0.257697	1314.763306	3.601007	0.011151
584.192017	4.434673	0.252305	1318.191162	3.600331	0.01111
585.778687	4.428071	0.247008	1321.619873	3.599662	0.011069
587.365417	4.421504	0.241804	1325.04895	3.598998	0.011029
588.952026	4.414969	0.236691	1328.47876	3.598339	0.010989
590.538635	4.408469	0.231668	1331.908936	3.597687	0.010949
592.125122	4.402002	0.226734	1335.339844	3.597039	0.01091
593.711609	4.39557	0.221887	1338.77124	3.596397	0.010871
595.297974	4.389172	0.217126	1342.203247	3.59576	0.010833
596.884338	4.382808	0.21245	1345.635742	3.595129	0.010795
598.470581	4.376479	0.207856	1349.06897	3.594502	0.010757
600.056763	4.370184	0.203345	1352.502686	3.593881	0.01072

601.642944	4.363924	0.198913	1355.93689	3.593265	0.010683
603.229004	4.357698	0.194562	1359.371826	3.592654	0.010647
604.815063	4.351507	0.190288	1362.807129	3.592048	0.01061
606.401001	4.34535	0.186091	1366.243164	3.591447	0.010575
607.986877	4.339229	0.181969	1369.679688	3.590851	0.010539
609.572632	4.333142	0.177922	1373.116943	3.59026	0.010504
611.158447	4.327089	0.173948	1376.554565	3.589673	0.010469
612.74408	4.321071	0.170046	1379.99292	3.589091	0.010435
614.329712	4.315088	0.166215	1383.431641	3.588514	0.010401
615.915283	4.309139	0.162454	1386.871094	3.587941	0.010367
617.500732	4.303225	0.158761	1390.311035	3.587373	0.010334
619.086121	4.297344	0.155136	1393.751709	3.586809	0.010301
620.671509	4.291498	0.151577	1397.192749	3.58625	0.010268
622.256714	4.285686	0.148084	1400.634521	3.585696	0.010236
623.841919	4.279908	0.144656	1404.076782	3.585145	0.010203
625.427063	4.274163	0.14129	1407.519531	3.584599	0.010172
627.012085	4.268452	0.137987	1410.963013	3.584058	0.01014
628.597046	4.262775	0.134746	1414.406982	3.58352	0.010109
630.181946	4.257131	0.131565	1417.851563	3.582987	0.010078
631.766785	4.25152	0.128443	1421.296631	3.582458	0.010047
633.351501	4.245942	0.12538	1424.742432	3.581933	0.010017
634.936157	4.240396	0.122374	1428.188599	3.581411	0.009987
636.520813	4.234882	0.119426	1431.635498	3.580894	0.009957
638.105347	4.229401	0.116533	1435.082886	3.580381	0.009928
639.689758	4.223951	0.113695	1438.530884	3.579872	0.009898
641.274109	4.218532	0.110911	1441.97937	3.579367	0.00987
642.858459	4.213145	0.10818	1445.428467	3.578866	0.009841
644.442627	4.207788	0.105502	1448.878174	3.578368	0.009812
646.026733	4.202462	0.102875	1452.328491	3.577874	0.009784
647.610779	4.197165	0.100299	1455.779297	3.577384	0.009756
649.194763	4.191897	0.097773	1459.230713	3.576898	0.009729
650.778687	4.186659	0.095296	1462.682739	3.576415	0.009701
652.362488	4.181448	0.092867	1466.135254	3.575936	0.009674
653.946167	4.176265	0.090486	1469.588379	3.575461	0.009648
655.529846	4.17111	0.088151	1473.042114	3.574989	0.009621
657.113403	4.16598	0.085863	1476.496338	3.57452	0.009595
658.696899	4.160875	0.083621	1479.951172	3.574055	0.009568
660.280273	4.155796	0.081423	1483.406494	3.573594	0.009542
661.863586	4.150739	0.079268	1486.862549	3.573136	0.009517
663.446777	4.145705	0.077158	1490.319092	3.572681	0.009491
665.029907	4.140692	0.075089	1493.776123	3.57223	0.009466
666.612976	4.135698	0.073063	1497.233887	3.571782	0.009441
668.195923	4.130722	0.071078	1500.692139	3.571337	0.009416
669.778809	4.125762	0.069134	1504.151001	3.570895	0.009392
671.361572	4.120814	0.067229	1507.610352	3.570457	0.009368
672.944275	4.115877	0.065364	1511.070313	3.570022	0.009343
674.526917	4.110946	0.063538	1514.530884	3.56959	0.00932
676.109375	4.106017	0.06175	1517.991943	3.569161	0.009296
677.691833	4.101083	0.06	1521.453613	3.568735	0.009272

679.27417	4.096136	0.058287	1524.915894	3.568312	0.009249
680.856384	4.091164	0.056611	1528.378662	3.567893	0.009226
682.438538	4.086147	0.054971	1531.842041	3.567476	0.009203
684.02063	4.08105	0.053367	1535.30603	3.567062	0.009181
685.6026	4.075793	0.051799	1538.77063	3.566651	0.009158
687.184448	4.069965	0.050546	1542.235718	3.566244	0.009136
688.766235	4.064646	0.050175	1545.701416	3.565839	0.009114
690.3479	4.059728	0.049803	1549.167725	3.565436	0.009092
691.929504	4.055032	0.049435	1552.634521	3.565037	0.00907
693.510925	4.050501	0.049069	1556.101807	3.564641	0.009049
695.092346	4.046103	0.048706	1559.569824	3.564247	0.009027
696.673645	4.041821	0.048347	1563.03833	3.563856	0.009006
698.254822	4.03764	0.047992	1566.507568	3.563468	0.008985
699.835938	4.03355	0.04764	1569.977173	3.563082	0.008964
701.416931	4.029544	0.047292	1573.44751	3.562699	0.008944
702.997864	4.025616	0.046947	1576.918213	3.562319	0.008923
704.578613	4.02176	0.046607	1580.389648	3.561941	0.008903
706.159302	4.017972	0.04627	1583.861572	3.561566	0.008883
707.739929	4.014248	0.045936	1587.334106	3.561194	0.008863
709.320435	4.010586	0.045607	1590.807251	3.560824	0.008843
710.900757	4.006982	0.045281	1594.280884	3.560457	0.008824
712.481079	4.003433	0.044958	1597.755127	3.560092	0.008804
714.061279	3.999938	0.04464	1601.22998	3.55973	0.008785
715.641357	3.996494	0.044324	1604.705322	3.55937	0.008766
717.221313	3.993099	0.044012	1608.181274	3.559012	0.008747
718.801208	3.989753	0.043704	1611.657837	3.558657	0.008728
720.380981	3.986452	0.043399	1615.13501	3.558305	0.00871
721.960632	3.983196	0.043097	1618.612549	3.557955	0.008691
723.540161	3.979983	0.042799	1622.09082	3.557607	0.008673
725.119629	3.976812	0.042504	1625.56958	3.557261	0.008655
726.698975	3.973682	0.042213	1629.049072	3.556918	0.008637
728.278198	3.970592	0.041924	1632.529053	3.556577	0.008619
729.8573	3.96754	0.041639	1636.009521	3.556238	0.008601
731.43634	3.964525	0.041357	1639.490601	3.555902	0.008584
733.015259	3.961548	0.041078	1642.97229	3.555568	0.008566
734.593994	3.958606	0.040802	1646.454468	3.555236	0.008549
736.172729	3.955698	0.040529	1649.937256	3.554906	0.008532
737.751282	3.952825	0.040259	1653.420654	3.554578	0.008515
739.329712	3.949985	0.039992	1656.904663	3.554253	0.008498
740.908081	3.947177	0.039728	1660.389282	3.553929	0.008481
742.486267	3.944402	0.039467	1663.874268	3.553608	0.008465
744.064392	3.941657	0.039208	1667.359985	3.553289	0.008448
745.642395	3.938943	0.038953	1670.846069	3.552972	0.008432
747.220276	3.936258	0.0387	1674.333008	3.552657	0.008416
748.798035	3.933603	0.03845	1677.820313	3.552344	0.0084
750.375671	3.930976	0.038203	1681.308228	3.552033	0.008384
751.953247	3.928378	0.037958	1684.796875	3.551724	0.008368
753.53064	3.925807	0.037716	1688.285889	3.551417	0.008352